CLARKSON UNIVERSITY

**FABRICATION AND CHARACTERIZATION OF GOLD NANOPARTICLE
REINFORCED CHITOSAN NANOCOMPOSITES FOR BIOMEDICAL APPLICATIONS**

A Dissertation

by,

Nimitt G. Patel

Materials Science and Engineering, Ph.D. Program

Submitted in Partial Fulfillment of the requirements
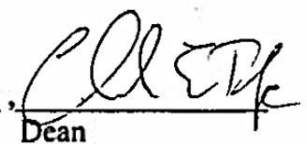
for the degree of

Doctor of Philosophy, Materials Science and Engineering

Friday, June 27, 2014

Accepted by the Graduate School

11 July 14

Date   Dean

UMI Number: 3636199

UMI

Dissertation Publishing

UMI 3636199

ProQuest®

The undersigned have examined the thesis entitled,
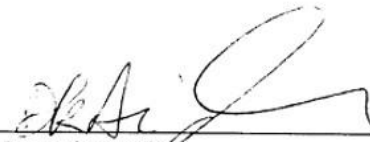
FABRICATION AND CHARACTERIZATION OF GOLD NANOPARTICLE REINFORCED CHITOSAN NANOCOMPOSITES FOR BIOMEDICAL APPLICATIONS

presented by **Nimitt Gunvantbhai Patel**, a candidate for the degree of **Doctor of Philosophy** in **Materials Science and Engineering,** and hereby certify that it is worthy of acceptance.

06/27/2014
Date

Dr. Philip A. Yuya

06/27/2014
Date

Dr. Daryush K. Aidun

06/27/2014
Date

Dr. Marilyn Freeman

06/27/2014
Date

Dr. Daniel T. Valentine

06/27/2014
Date

Dr. Don H. Rasmussen

ABSTRACT

Chitosan is a naturally derived polymer, which represents one of the most technologically important classes of active materials with applications in a variety of industrial and biomedical fields. Polymeric materials can be regarded as promising candidates for next generation devices due to their low energy payback time. These devices can be fabricated by high-throughput processing methodologies, such as spin coating, inkjet printing, gravure and flexographic printing onto flexible substrates. However, the extensive applications of polymeric films are still limited because of disadvantages such as poor electromechanical properties, high brittleness with a low strain at break, and sensitivity to water. For certain critical applications the need for modification of physical, mechanical and electrical properties of the polymer is essential. When blends of polymer films with other materials are used, as is commonly the case, device performance directly depends on the nanoscale morphology and phase separation of the blend components. To prepare nanocomposite thin films with the desired functional properties, both the film composition and microstructure have to be thoroughly characterized and controlled.

Chitosan reinforced bio-nanocomposite films with varying concentrations of gold nanoparticles were prepared through a solution casting method. Gold nanoparticles (~ 32 nm diameter) were synthesized *via* a citrate reduction method from chloroauric acid and incorporated in the prepared Chitosan solution. Uniform distribution of gold nanoparticles was achieved throughout the chitosan matrix and was confirmed by SEM images. Synthesis outcomes and prepared nanocomposites were characterized using TEM, SAED, SEM, EDX, XRD, UV-Vis, particle size analysis, zeta potential and FT-IR

for their physical, morphological and structural properties. Nanoscale mechanical properties of the nanocomposite films were characterized at room temperature, human body temperatures and higher temperatures using instrumented indentation techniques. The obtained films were confirmed to be biocompatible by their ability to support the growth and proliferation of human tissue cells *in vitro*. Statistical analysis on mechanical properties and biocompatibility results, were conducted. Results revealed significant enhancement on both the mechanical properties and cell adherence and proliferation. The results will enhance our understanding of the effect of nanostructures reinforcement on these important functional polymeric thin films for potential biomedical applications.

ACKNOWLEDGEMENTS

grateful to Ted Champagne and Chris Plunkett for their help with electron microscopy. I

thank my parents, family, friends and lab-mates for their support during the course of this

work.

Table of Contents

List of Figures

List of Tables

Chapter 1. Introduction

1.1 Problem Description

Ever increasing world population creates a real need for technological development in the medical field to improve human welfare and quality of life. Research in medical science, instrumentation technologies, physical therapies and biomedical engineering is of high importance when it comes to wellbeing of the human population. In the past few decades, biomedical science and engineering using bio-inspired materials and biomaterials is one of the rapidly growing branches in the medical field.

A biomaterial is a synthetic or natural material that is used to replace or restore function to a body tissue and is continuously or intermittently in contact with body fluids. Biomaterials are derived from natural organisms and plants and are biocompatible, biodegradable and renewable. While there is a need for a prominent approach towards development of biocompatible, biodegradable and renewable materials, chitosan opens numerous opportunities in biomedical and commercial applications. Chitosan is commercially obtained by deacetylation of chitin; which is a structural component of shell-fish crust [1]. Other sources of chitin include mollusks, squid back-bones, insect cuticles, algae (marine diatoms), protozoa and cell walls of various fungal spices [1, 2]. After cellulose chitosan, which is a polysaccharide, stands at the prime position for its abundance in nature. Being biocompatible, chitosan could be used in many applications areas such as implants, biomedicines, dental materials, bone substitute materials, wound healing, tissue engineering, absorbable sutures, drug delivery [3-5] as well as food packaging [6], water treatment, reverse osmosis [7], cosmetics [8] and many more. Chitin

and chitosan derivatives demonstrate excellent performance while being used in artificial organs in the areas of skin [9, 10], bones, nerves, cartilage and blood vessels [9]. Chitosan also has potential to be used as a primary material for implantable biosensors. Implantable biosensors are widely used in various applications such as blood glucose and uric acid monitoring. Some functions of these biosensors such as pressure and force measurement, when used in load bearing applications, require certain mechanical stability over a prolonged period of time. For example, compressive stress sensor probes have been implanted in the annulus of intervertebral discs [11]. Components of such biosensors are often subjected to various stresses under different environmental conditions.

Chitosan films and membranes are often subjected to different mechanical, thermal and frictional stresses while in service. For instance, Chitosan film applied for a skin grafting or a wound healing gets exposed to mechanical stresses such as stretching, compression and twists. Chitosan, when used in bioactive coatings in orthopedic and dental implants [12] experiences different physical and mechanical stresses. For such films, both electrical and mechanical characteristics should be well understood to achieve optimum performance.

For certain critical applications, the need for modification of physical and mechanical properties of biomedical material is essential. Incorporation of nano-scaled materials in chitosan improves both their electromechanical and physical properties [5, 6, 13-18]. Gold is a widely known biocompatible material that can be used in implants, nerve repairs, bio-sensors and other bio-medical applications. Chitosan reinforced with gold nanoparticles has proven to be a biocompatible and mechanically stronger

2

(compared to pure chitosan) material when used for sciatic nerve repair [19]. Not only mechanical stability, but also the biocompatibility could be improved by reinforcing implant polymers with gold nanoparticles. Chitosan embedded with gold nanoparticles is an excellent material as a signal transmitting device in a physio-chemical condition monitoring sensors [20]. Gold-chitosan nanocomposites yield promising results in sensors for determining polyphenol index in wine [21], glucose [22, 23] , as a bio-adhesive for advanced tissue repair and wound dressing applications [24] and also as an implant for a peripheral nerve repair for physical injury [19].

To achieve optimum performance of materials used in biomedical engineering, understanding their physical, morphological, and electromechanical properties is very important. To use chitosan as a material for wound healing, its mechanical properties should be comparable to that of the wound and surrounding tissues to avoid any physical mismatch, and to prevent failures in treatment. Limited emphasis has been given to mechanical properties characterization of chitosan based nanocomposites for bio-medical applications compared to their reliability and biocompatibility characterization partly due to lack of appropriate characterization techniques.

1.2   Objectives

Cell-tissue interactions occur at nano and micro scales. As a result, in tissue engineering and wound healing applications, it is important to understand physical and mechanical properties of the engineered biomaterials and target tissues at nano-scales. In most cases of tissue engineering, mechanical properties of grafted scaffolds are often compared with that of the target tissues. With such conditions, in-depth understanding of

the nanomechanical properties of the bio-engineering materials is essential. It is also desired to develop the method to fine-tune the nanomechanical properties of the bio-engineering materials for targeted application areas. To the best of my knowledge, not enough attention has been given to the development of nanocomposites with controllable nanomechanical properties with the use of crystalline gold nanoparticles within the chitosan matrix for biomedical applications.

The objectives of the dissertation are:

1. Synthesize crystalline gold nanoparticles and process chitosan polymer matrix

2. Fabricate thin films of the bio-nanocomposites from as-prepared gold nanoparticles and chitosan polymer with different concentration of the nanoparticles

3. Characterize morphological, chemical and microstructural properties of the nanocomposites solutions and the solid films through transmission electron microscopy, scanning electron microscopy, X-ray diffraction analysis, UV-Vis spectroscopy, energy dispersive X-ray spectroscopy, selected area electron diffraction analysis, zeta potential measurements and dynamic light scattering techniques

4. Quantitatively determine mechanical properties such as elastic, visco-elastic and elasto-plastic characteristics at nanoscale as a function of temperatures comprising room temperature and human body temperature

5. Determine biocompatibility by observing the cell proliferation capabilities of the bio-nanocomposite films through *in-vitro* cell culture studies

It is hypothesized that the mechanical properties of the chitosan films will be enhanced by incorporation of more crystalline metallic phase of the gold element. Because of the dimensional stability of the nanoparticles, efficient metal-polymer adhesion and accurate control over the concentration of the gold nanoparticles, mechanical properties of the nanocomposites are expected to be fine-tunable, which is essential for the certain biomedical applications. It is also expected that the biocompatibility of the chitosan will not be affected by the addition of gold because of its non-corrosive, non-toxic and biocompatible nature.

1.3 Dissertation Organization

From this point in this work, first background and literature review on chitosan based materials used in biomedical engineering is given in Chapter 2. After which, processing and fabrication of the nanomaterials, polymers, and polymer reinforced nanocomposites, and methods to characterize their physical, microstructural, morphological, nanoscale mechanical properties, and their biological nature are discussed in Chapter 3. Along with experimental procedures, operating principles and theories behind the characterization methods are also discussed in detail in Chapter 3. In Chapter 4, the results are shown and discussion based on critical analysis of the outcomes is presented. In Chapter 5, summery of the work and concluding remarks are discussed based on the results obtained and presented in Chapter 4. Finally, Chapter 6 (the last chapter) shows future opportunities regarding development of the material, and methods to explore various other properties with advanced characterization techniques. Challenges associated with the future opportunities and possibilities of potential solutions are also discussed in the last chapter.

Chapter 2. Background and Literature Review

2.1 Biomedical Engineering

Biomedical engineering or bioengineering is the application of engineering principles in making improvements in the biological and medical fields for development of the well-being of human beings. The field seeks to close the gap between medicine and engineering fields. Biomedical engineering has had a great impact on life expectancy and better health in the past century. As indicated in **Table 2.1**, in the USA alone, millions of patients suffer and die as a result of tissue and organ deficiencies. Biomedical engineering field has proven great success in improving lives of people with medical impairment. In-effective and inefficient human organs have been effectively replaced with artificial replacements with high-tech engineering approaches in recent years [25-27]. Functions of certain devices, instruments and materials used in the fields of biomechanics, bio-molecular engineering, bioinstrumentation, bio-imaging and biomaterials can be fine-tuned with advanced engineering approaches to improve their efficiency for targeted applications. There was a time when lives of human beings were threatened even with minor injuries or impairments. With the advancement in the area of biomedical engineering, it is now possible to heal wounds, cuts, burns, bumps and scars, repair bone fractures, deliver drugs to heal affected tissues, fill dental cavities, repair internal and external tissue injuries, improve vision and do much more. More critical surgeries such as replacing damaged heart values with the artificial valves and synthetic blood vessels have also become possible.

Biomedical engineering is relatively new field compared to other classical engineering disciplines. Because of that, bioengineering field requires expertise from

other disciplines such as electrical, mechanical, materials and chemical engineering as well as physical and biological sciences to solve potential healthcare problems.

Table 2.1 Data for organ and tissue deficiencies [28] (b) approximately 150,000 from these are hospitalize and 10,000 of them die annually

Indicator	Procedures or Patients per Year
Skin	
Burns (b)	2,150,000
Pressure sores	150,000
Venous stasis ulcers	500,000
Diabetic ulcers	600,000
Neuromuscular disorders	200,000
Spinal cord and nerves	40,000
Bone	
Joint replacement	558,200
Bone graft	275,000
Internal fixation	480,000
Facial reconstruction	30,000
Cartilage	
Patella resurfacing	216,000
Chondromalacia patellae	103,400
Meniscal repair	250,000
Arthritis (knee)	149,900
Arthritis (hip)	219,300
Fingers and small joints	179,000
Osteochondritis dissecans	14,500
Tendon repair	33,000
Ligament repair	90,000
Blood vessels	
Heart	754,000
Large and small vessels	606,000
Liver	
Metabolic disorders	5,000
Liver cirrhosis	175,000
Liver cancer	25,000
Pancreas (diabetes)	728,000
Intestine	100,000
Kidney	600,000
Bladder	57,200
Ureter	30,000
Urethra	51,900
Hernia	290,000
Breast	261,000
Blood Transfusions	18,000,000
Dental	10,000,000

2.2 Materials for Bioengineering

Biomaterials are the materials used in the medical field. In other words, these are materials that are chemically, physically and structurally considered compatible with natural biological tissues and organs. To be a successful biomaterial, it has to meet certain factors such as physical properties, cytotoxicity, biocompatibility and design. Major application areas of biomaterials in biomedical engineering include, but not limited to, drug delivery, tissue engineering, prosthetics, biosensors and wound healing (**Figure 2.1**).
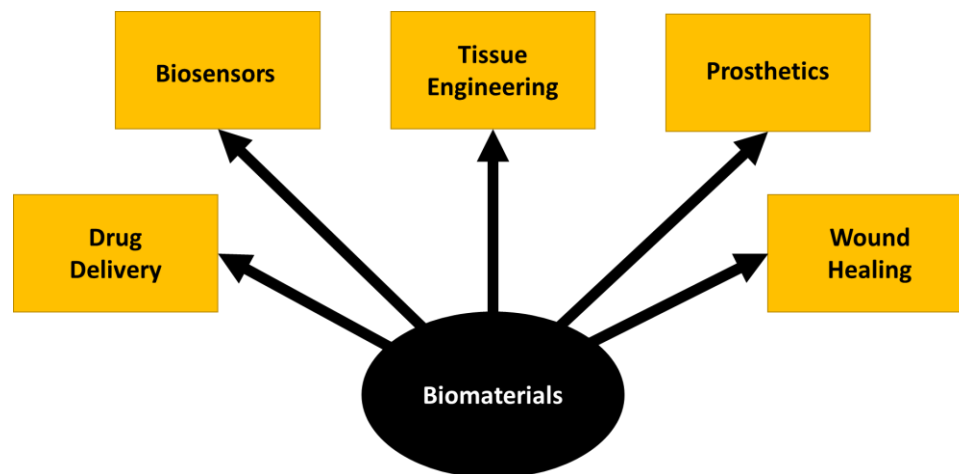
Figure 2.1 Application areas of biomaterials in biomedical engineering

Biomaterials are generally classified in four broad categories: 1.) polymers, 2.) metals, 3.) ceramics, and 4.) composites. Each of these materials has its own application potentials, advantages and drawbacks. For example, devices made of polymers can be fabricated by high-throughput processing methodologies such as spin coating, inkjet printing, gravure and flexographic printing onto flexible substrates. They also demonstrate excellent resilience and flexibility. Certain polymers can be used in

replacing soft tissues such as skin, nose, ear, blood vessels, hip sockets and sutures. However, the potential problem with polymers is their disadvantages such as poor electromechanical properties, high brittleness with a low strain at break, and sensitivity to water. They also demonstrate time dependent performance strength, i.e. their shape and strength change with time. Also, most polymers easily degrade physically and chemically with aging.

Metals such as stainless steel, titanium, gold, silver and platinum have excellent strength. Their toughness and ductility can also be fine-tuned with various compositions of different elements (by making alloys). High strength metals are used to replace damaged bones and joints, making screws for the implant attachment with connecting bones, dental root implants and wires for various implantable instrumentations. However, the density and specific weight become major issues when considering such materials for certain biomedical applications. For example, plates, rods or balls made of steel may cause physical imbalance when used as a substitute for replaced bone material. With metals, chances of corrosion and erosion in the long run are also possible. They also involve costly manufacturing processes.

Bio-inert ceramics such as calcium phosphates (bone cements), aluminum oxide and carbon are non-reactive with high level of biocompatibility. Additionally they exhibit high load bearing capacity with compressive stresses. They are widely used in orthopedic and dental implants where the organs are continuously subjected to repeat compressive loading. The disadvantage of using ceramics in implants is their low resilience and hence extremely brittle nature which make them prone to sudden cracking and rupture. To make use of positive characteristics of certain materials while avoiding their drawbacks,

development in composite materials can be potentially rewarding. Carbon fiber reinforced epoxy, wire or fiber reinforced bone cement, nano-filler reinforced polymer sheeting and thin films are a few examples of composite materials which can be very useful in serving various functions in biomedical field. Composite materials can be used in applications such as joint implants, heart valves and tissue repair, to name a few. The challenges associated with composite materials are their complex design, difficult processing and costly production. It is also important to model the materials response to understand and predict its lifetime and service performance.

2.3 Chitosan source, processing, structure and properties

Environmental concerns have driven the attention towards developing bio-based polymers to overcome environmental sustainability drawbacks of synthetic polymers. Considering increasing need of special purpose materials and rising environmental concerns, more emphasis on modifying biopolymers with advanced technology is needed. The perspective of sustainable development has directed materials research towards modification of new materials for targeted end applications. Natural polymers need such attention to tailor their inherent properties which qualify them for certain end use.

Nature has evolved a wide range of materials for specific functions in animals, plants, and marine-life organisms from which, cellulose and chitin are with the most abundance in nature. Chitin and chitosan are polysaccharides commonly available from exoskeletons of various crustaceans such as shrimps and crabs, insects and mushrooms (**Figure 2.2**). Other sources of chitin include mollusks, squid back-bones, insect cuticles, algae (marine diatoms), protozoa and cell walls of various fungal spices [1, 2]. In the past

decade, processing, chemistry, microstructure and properties of chitosan have been thoroughly studied. The primary functions of chitin and chitosan in shrimp and crabs is to provide sufficient strength and protection to survive in various environmental conditions. Being natural polymers, chitin and chitosan are biodegradable and nontoxic materials. Because of such fundamental natural properties, they open wide range of applications in the biomedical field which will be discussed later in this chapter.
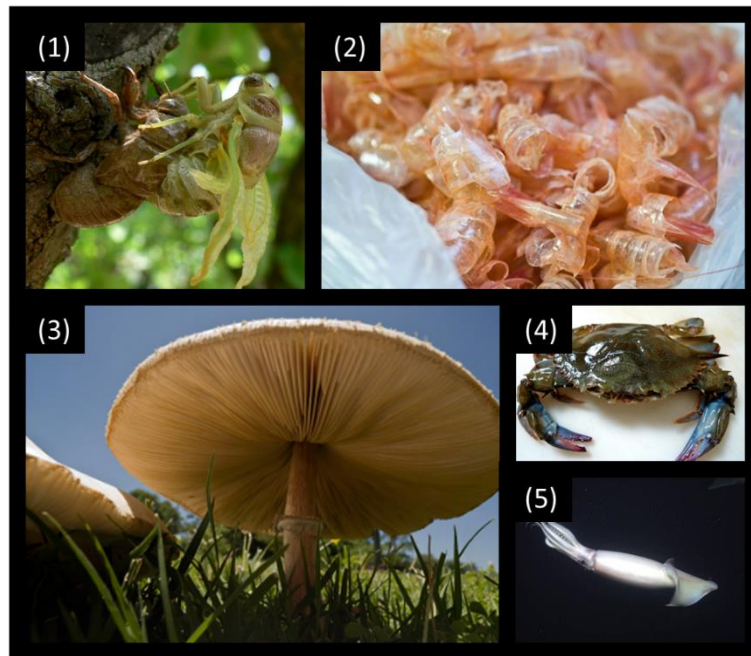
Figure 2.2 Various sources of Chitin - a primary source of chitosan (1) Cicada with exoskeleton (2) shrimp shells (3) mushroom (4) crab, and (5) squid

Chitosan is derived from chitin by deacetylation. Deacetylation is the process of removing acetyl group from the molecules of chitin under harsh environment of concentrated sodium hydroxide (NaOH). The process leaves behind the amine ($-NH_2$) groups of the chain with the final chitosan. Care is taken to avoid any undesirable effects such as de-polymerization and/or formation of reactive groups. To shield the process

11

from such undesirable effects, deacetylation of chitin is normally conducted in nitrogen purged environment or by adding sodium borohydride in NaOH solution. [29] Step-by-step procedure to extract chitosan from their natural sources is shown in **Figure 2.3**. A schematic illustration of molecular chemical structure of chitin and chitosan is shown in **Figure 2.4**. As shown in **Figure 2.4**, chitin chain consists of repeat units of N-acetylglucosamine. In natural form of the polymer, — NH_2 (primary amine) group is protected with acetyl group which makes chitin least soluble in water, and least reactive which limits its applications. Because of that, it is important to free amine groups from acetyl group. The degree of deacetylation is the extent at which these acetyl groups are removed from the polymer in its natural form. The higher the degree of deacetylation, the more soluble and reactive the chains will be. Upon deacetylation, chitin takes the form of chitosan (**Figure 2.4**). In this work, chitosan with degree of deacytylation of 75-85% was used. In nanocomposite technology, gold-amine [30] and gold-thiol [31, 32] interaction chemistry is well established. As seen in **Figure 2.4**, deacetylation frees the amine groups from the acetyl groups. These free — NH_2 groups present on chitosan chains have great potential to bind easily (without any binding reagent) with gold nanoparticles.
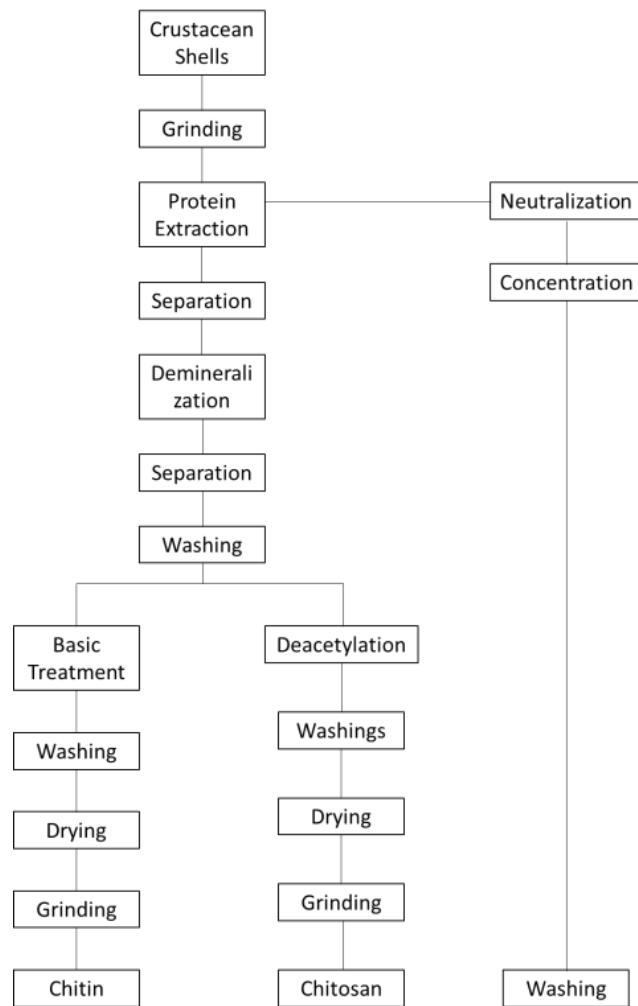
Figure 2.3 Schematic illustration showing procedure to extract chitin and chitosan from crustaceans [33]
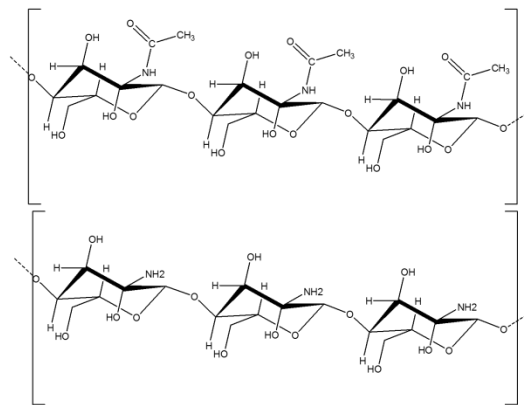
Figure 2.4 Molecular structure of chitin [top] and chitosan [bottom]

2.4 Applications of chitosan

Chitosan is a bio-based natural polymer that exhibits properties such as film-forming abilities, antimicrobial nature, binding capacity and strength comparable with various synthetic polymers. Chitosan has potential for applications in wide range of fields such as agriculture [34], cosmetics [35], biotechnology [36], food [37], water treatment [38], pulp & paper [39], medical [40] and membranes [41]. In agriculture, chitosan is used in seed and leaf coating [42] and in controlled agro-chemical release technology. In food processing industries, chitosan is used as a color stabilizer, preservatives, dye and acid removal and as an additive for animal foods. In membrane technology for solvent separation and permeability control, chitosan can be used with certain chemical and physical modifications [43]. In paper industries, chitosan is used for surface treatments, for making carbon-less copy papers and photographic papers. In water treatment, to remove proteins, metal ions, dyes, amino acids and filtering certain impurities, chitosan has been proven to be a material of interest. Chitosan has potential applications in the field of biotechnology in the areas such as chromatography [44], protein separation [45-47], enzyme [48] and cell [49] immobilization and glucose sensor electrodes [50]. Compared to other areas, chitosan can be most rewarding if used in biomedical engineering because of its biocompatible nature, mechanical stability and excellent biodegradability. In medical field, chitosan can be used in bandages, artificial blood vessels and valves, blood cholesterol control, wound healing, skin grafting, tissue engineering, contact lenses, drug-delivery, implants and implant coatings, bio-sensors, tumor inhibition and artificial body fluids, to name a few. In this chapter, applications of chitosan in the field of biomedical engineering are emphasized. In following sections,

few of the major applications of chitosan in biomedical field such as tissue engineering and wound healing are discussed.

2.4.1 Tissue Engineering

Tissue engineering is a technique used to develop, modify and optimize methods to repair and/or replace damaged or anomalous body tissues. Repair or replacement of tissues is done by growing cells onto scaffolds, *in vivo* or *in vitro*. With increasing world population and hence, increasing need to develop advanced technology to survive from deficiencies in structural components of organs, much attention is being given towards advancement in tissue engineering. [51] The combination of artificial organs, scaffolds, biomaterials and differentiation cells need improvement in standards and quality to avoid major tissue and organ damage. Porous biodegradable polymer matrix is an excellent material to seed and grow living cells on its surface and within its structure. More recently, there has been much interest in modifying chitosan to improve its solubility and change its physio-chemical properties by introducing various type of side chains to make it fit for a wide range of applications [52-57]. Ding et al. [58] discussed potential applications graft polymerized chitosan on to Poly-L-Lactic Acid (PLLA) surface in tissue engineering field. Tissues of skin, bones, nerves and ligaments can be successfully repaired by using appropriate technique with tissue engineering. When used in such applications where living human cells need to attach and grow onto the surface and interfaces, it is of high importance to bear properties such as biocompatibility, mechanical strength and durability for the material. In a recent study [59], composites made of chitosan, PVA and inorganic bioactive glass were developed for their use in bone tissue engineering as a mechanically stable scaffold. In order to enhance cell

growth, tissue scaffolds must exhibit proper attachment with the host tissues, be capable to transport enough nutrients throughout the cross-section and accelerate cell growth to achieve specific mechanical strength, stability and desired biological performance. For such inevitable functions, it is highly desirable for the replacement tissues to have some level of porosity to facilitate transportation of cells and other body fluids. In this regard, chitosan is an excellent material to perform certain functions with desired efficiency. **Figure 2.5** shows microstructure of chitosan film with porous structure and in **Figure 2.6**, regeneration of skin tissues using chitosan is shown.
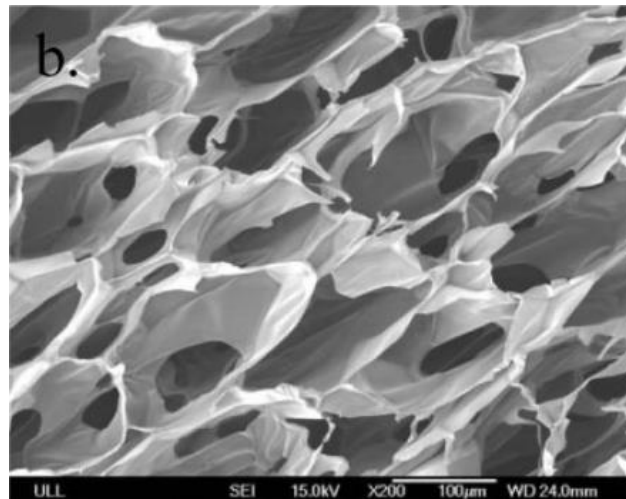
Figure 2.5 Porous microstructure of pure chitosan [60]

2.4.2 Wound healing

Similar to tissue regeneration, chitosan delivers great benefits in healing wounds, cuts and burns. In a study by Harkins et al. [61] it has been shown that because of its antimicrobial activity, blood absorption ability and excellent biocompatibility, chitosan combined with cellulose can be primarily used in would healing materials. Khan et al. [62] found that chitosan processed with certain chemical treatments makes flexible, soft, non-toxic and non-allergic material for would dressing that is comparable with existing

16

Figure 2.6 Chitosan acetate films for skin tissue regeneration (a) The film set up, (b) The film after the application, (c) The third day evolution, (d) The sixth day evolution, (e) and (f) Fourteenth day of evolution [10]

commercial product Omiderm® used for would healing. Chitosan acetate is an antimicrobial material and main constituent used in the making of HemCon® bandages. **Figure 2.7** illustrates functions such as bleeding control, adhesion, and would healing performed by HemCon® bandages made of chitosan. Burkatovskayaa et al. [63] demonstrated the benefits of using chitosan in would healing applications by performing experiments on mice skins. **Figure 2.8** shows improvement in relieving wounds of mice using chitosan and alginate made bandages.
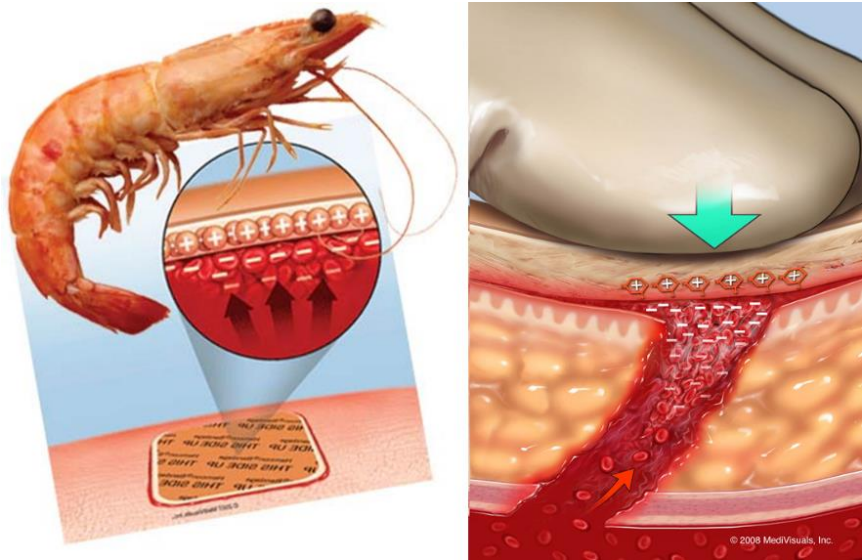
Figure 2.7 illustration of functions performed by a HemCon® bandage made of chitosan ©MediVisuals, Inc. 2008 [64]

Figure 2. 8 Chitosan and alginate used in healing wound in mice [63]

Polymers used in biomedical applications are often subjected to various kinds of physical and mechanical stresses. For certain critical applications, it is desired that the materials is reliable throughout its life span. Failure of such materials could result in devastating situations. For example, chitosan used in heart valves [65] is continuously subjected to cyclic forces as a results of expansion-contraction cycles of the blood vessels near the heart regions. In such applications of chitosan films, the importance of mechanical stability is second to none. To predict how long the material will last under certain cyclic loading, it is desired to perform time dependent viscoelastic properties characterization.

Chapter 3. Materials and Experimental Methods

3.1 GNP-Chitosan nanocomposites preparation

3.1.1 Materials

Low molecular weight Chitosan (M_w = 50-190 KDa; ~85% of deacetylation), acetic acid (≥99.0%), chloroauric acid ($HAuCl_4:3H_2O$) and sodium citrate tribasic dehydrate (≥ 99.0%) were purchased from Sigma Aldrich (St. Louis, MO). Ultra high purity water (resistivity 18.3 − 18.5 MΩ.cm at 25 °C) was obtained using a Milli-Q Element® water purification system (EMD Millipore, Billerica, MA). All experiments were performed using Milli-Q water. All glassware and stir bars were first cleaned with a soap solution and rinsed with deionized water followed by bath washing in a freshly prepared aquaregia ($HCl:HNO_3$ 3:1). After which, they were thoroughly rinsed with deionized water, drained and dried in an oven at 50 °C.

3.1.2 Preparation of gold nanoparticles and gold-chitosan bionanocomposite films

Gold nanoparticle suspension in aqueous solution was obtained *via* a citrate reduction method. **Figure 3.1** shows the color of the suspension changing from pale yellow to dark greyish and finally wine red. It shows that citrate ions have reduced gold chloride to pure gold nanoparticles with citrate ligands on the nanoparticles surface. With the use of high speed ultra-centrifuge, the obtained suspension was washed three times with ultra-pure Milli-Q water to remove any possible side products and finally stored in an amber bottle at room temperature for later use.
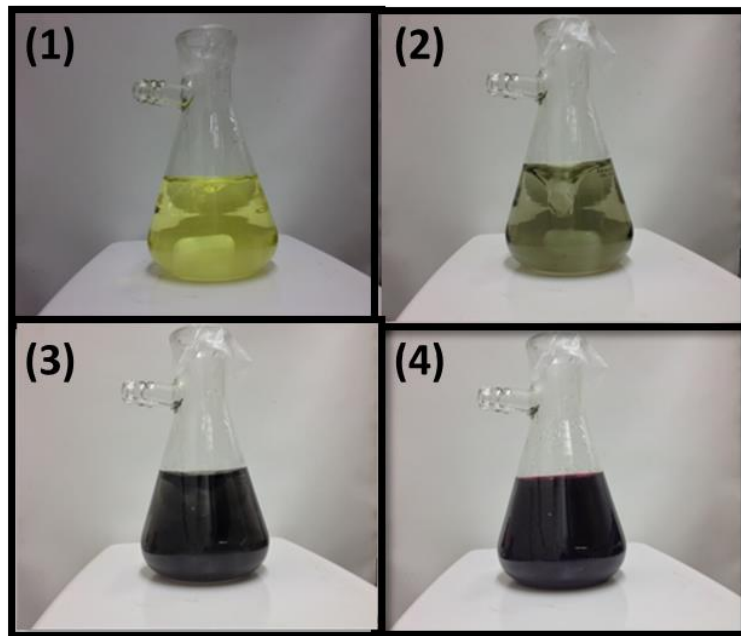
Figure 3.1 Gold nanoparticle formation from gold chloride solution

Gold nanoparticles were obtained *via* the classical Terkovich et al. [66] method with slight modifications. 100 ml of $HAuCl_4$ (2.54 mM) solution was vigorously stirred at 50 °C on a hot plate stirrer for 10 minutes. 2 ml of freshly prepared sodium citrate (10% w/w) was quickly added to the aqueous solution of $HAuCl_4$. The solution was brought to room temperature after 3 hours and continually stirred for next 12 hours. Obtained gold nanoparticles were washed with DI water and subsequently centrifuged at 7000 rpm (~3500 x g) for 10 min to remove unreacted salts. Finally washed Au nano-dispersion in DI water was kept in sealed glass vials for embedding them into the chitosan matrix. Synthesized gold nanoparticles were characterized using SEM, TEM, UV-Vis, particle size analyzer and zeta potential to evaluate their stability and size distributions before being dispersed in chitosan/acetic acid solution for preparing bionanocomposite films.

Low molecular weight Chitosan (2 % w/w) was mixed with 150 ml solution of diluted acetic acid (1 % w/w). The mixture was stirred at room temperature for 24 hours until it turned transparent showing that chitosan had been dissolved completely. After that, the solution was filtered with a small pore sized (5 μm) filter paper and stored at 4 °C in amber vials for the later procedures. Gold nanoparticle reinforced chitosan nanocomposites were prepared by adding gold nanoparticle suspensions of different concentrations drop wise into the vigorously stirring chitosan solutions. The mixtures were stirred for 12 hours to ensure uniform dispersion of gold nanoparticles in the chitosan matrix. The composite solutions were again characterized using SEM, UV-Vis and zeta potential for the gold particle dispersion, entrapment efficiency and to study the aggregation of gold-nanoparticles in the chitosan matrix. Nanocomposite films were prepared via a solution evaporation method. [18] Gold-chitosan nanocomposite solutions were kept in petri dishes and degassed in vacuum to remove entrapped air. The degassed composite solutions were kept at room temperature for drying. After which, the dried films were carefully removed from the petri dishes and put in a vacuum desiccator to remove moisture. Finally, the as obtained films were carefully stored in a desiccator for subsequent studies. **Figure 3.2** shows the procedure used to fabricate gold-chitosan nanocomposites in this work. Au-chitosan nanocomposite films with gold nanoparticles concentration (w/v) of 0 mg/ml (pure chitosan), 0.10 mg/ml, 0.15 mg/ml, 0.20 mg/ml and 0.25 mg/ml in chitosan solution are referred to here as Film 1, Film 2, Film 3, Film 4 and Film 5, respectively.

Temperature is
maintained at 100 °C

Double distilled water

Temperature is
maintained at 100 °C

Aq. Gold solution

Temperature is
maintained at 100 °C

Aq.Trisodium citrate

Citrate capped Gold nanoparticle

Au

1% acetic acid;
pH=4

Sonication and
filtration

Chitosan Powder
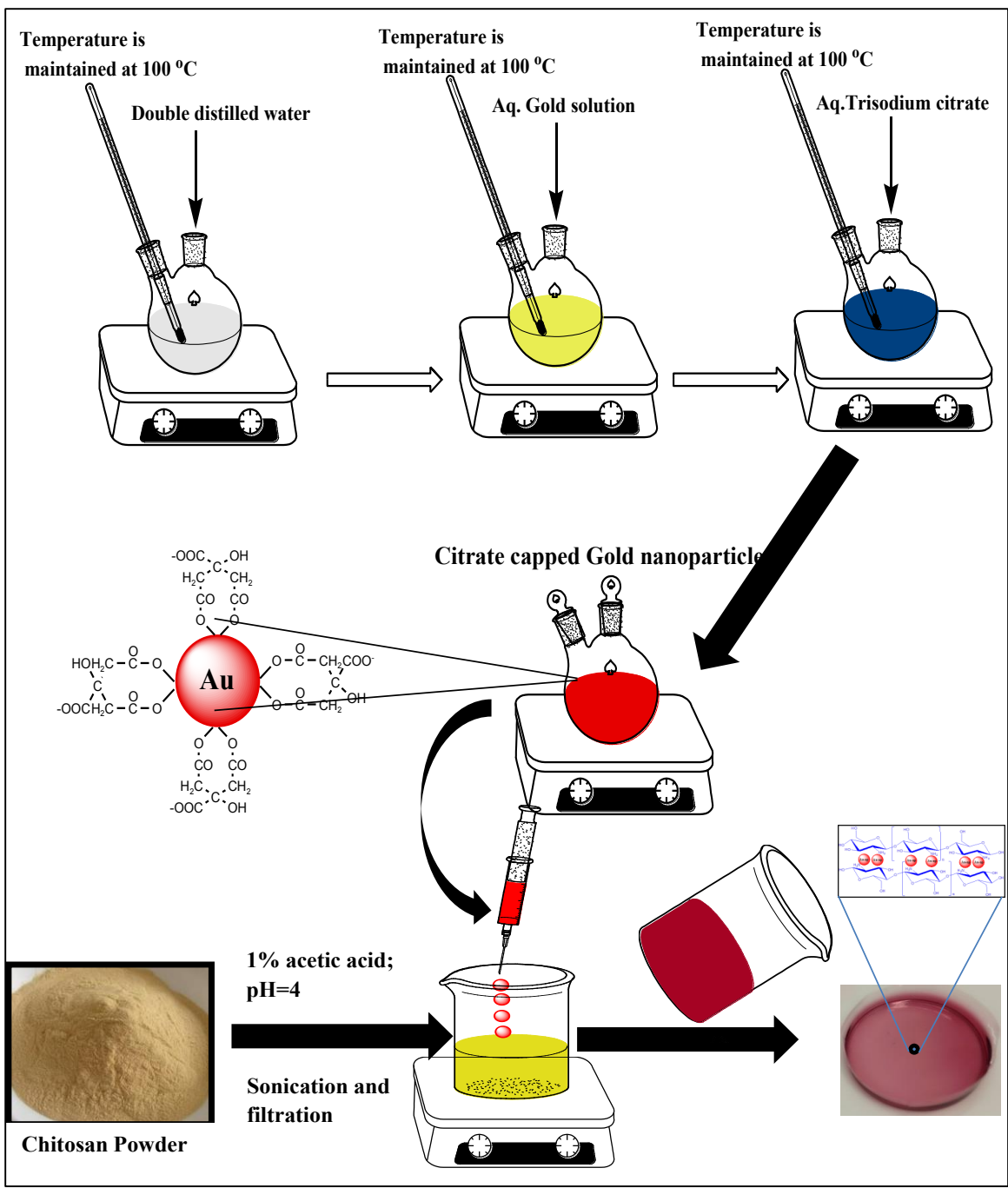
**Figure 3.2 Schematic representation of the procedure used to make gold
nanoparticle reinforced chitosan nanocomposites**

23

3.2 Materials Characterization

After several chemical processes and fabrication of the material, its physical, chemical, morphological, microstructural, mechanical and biological properties were characterized. In this section, operating principles and methodologies of the characterization techniques such as UV-Vis, transmission electron microscopy, selected area diffraction spectroscopy, particle size analysis, scanning electron microscopy, electron diffraction spectroscopy, dynamic and quasi static nanoindentation and *in-vitro* cytocompatibility testing are discussed.

3.2.1 Microstructural and Morphological Characterization

Nanocomposites are prone to develop microstructural defects and discontinuities as a result of forces developed at molecular level, unwanted contamination, inclusion of foreign material and various processing conditions such as temperature and pressure. Such irregularities in the materials structure could significantly affect its performance adversely. Also, it is important to understand materials chemistry and its physiochemical mechanism. For example, studying the interfacial condition of the nano-fillers with the surrounding bonded matrix helps in predicting its mechanical performance enhancement. Characterizing the materials toxicity and biocompatibility helps in predicting its reliability for the targeted application.

3.2.1.1 UV-Vis (ultraviolet-visible) spectroscopy

UV-Vis spectroscopy is an important tool for qualitative and quantitative determination of gold nanoparticles and gold nanoparticle-reinforced chitosan

nanocomposites solutions. The working principle of the technique is described briefly below.

When a certain electronic transition matches the energy of a certain band of UV, it is absorbed and the remaining radiations pass through the sample. Using this residual radiation, a spectrum is obtained with "*gaps*" at these discrete energies which is called an *Absorption Spectrum.* A simple schematic diagram that can describe most modern UV spectrometers is shown in **Figure 3.3**. Two sources are required to scan the entire UV-Vis band: 1) Deuterium lamp – covers the UV- 200-330 nm wavelengths. 2) Tungsten lamp – covers 330-700 nm wavelengths. The lamps illuminate the entire band of UV or visible light and the monochromator (grating or prism) gradually changes the small bands of radiation, and sends it to the beam splitter. After that, the beam splitter sends a separate band to a cell containing the sample solution and a reference solution. The detector measures the difference between the transmitted light through the sample (I) versus the incident light (I_o) and sends this information to the recorder.

In this work, UV-Visible spectrophotometer (Lambda 50 by Perkin Elmer, Waltham, MA) was used for characterizing the nanoparticles and nanocomposites suspensions. Chitosan solution containing gold nanoparticles with concentration of 0.10 mg/ml, 0.15 mg/ml, 0.20 mg/ml and 0.25 mg/ml were analyzed by reducing their concentration to 50 % of the original solution. Serial dilution was performed with the synthesized gold solution with known concentration to calculate the actual concentration of the gold in the chitosan matrix. The procedure to determine actual gold concentration in the chitosan matrix using UV-Vis spectroscopy is discussed in Chapter 4.
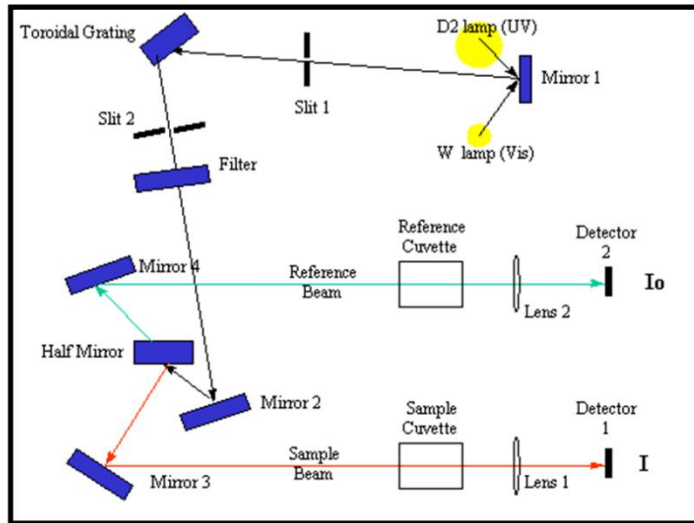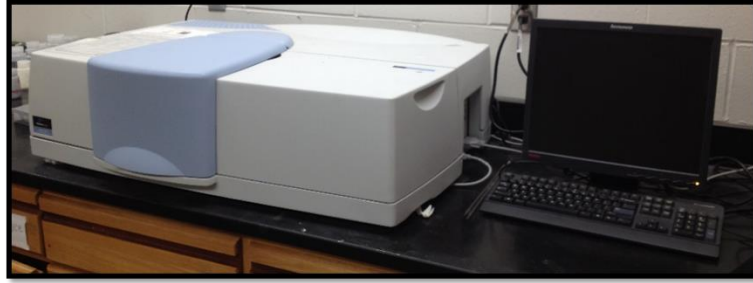
Figure 3.3 Picture of the UV-Vis equipment used in this study (Top), and schematic of the operation explained in the text (Bottom)

3.2.1.2 Transmission Electron Microscopy

Transmission Electron Microscopy (TEM) is a vital characterization tool for directly imaging nanomaterials and nanocomposites to obtain a qualitative measure of particles size, distribution, and morphology. Since performance of materials such as mechanical and chemical stability for certain applications strongly depend on their microstructural conditions, it is very important to explore the material's microstructure with such techniques. Following is a brief discussion on the operating principles and analytical procedure of TEM.

In TEM, the sample is irradiated with a beam of high energy electrons. When the beam passes through the sample, one can get a transmitted as well as diffracted beam. The image is formed by the interference between the transmitted and diffracted beam and the resultant image can be seen on a fluorescent screen. This permits a very high resolution of the order of 2Å. To reach the main fluorescent screen, the electron beam has to pass through the sample. Therefore, preparation of high quality samples is a prerequisite. With recent advances in the TEM technologies, it is possible to obtain high resolution electronic images directly with the use of computers and software and because of that, fluorescent screen technique is obsoleting. **Figure 3.4** shows the TEM instrument used in this work and schematic representation of the operating principle of TEM.
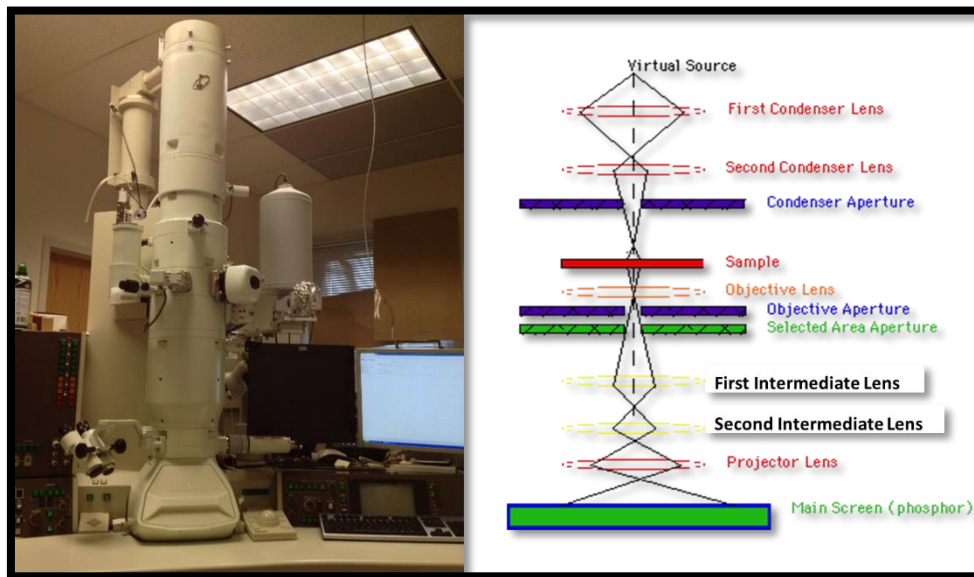
Figure 3.4 Picture of the TEM equipment used in this study (left), and schematic of the operation (right) (source: www.jeol.com)

In the present work, carbon pre-coated copper grids (200 mesh) purchased from Ted Pella, Inc. were used. One drop of the sample solution (containing dispersed

nanoparticles in water and ethanol) was put on the surface of grid and was allowed to dry in air at room temperature. Since gold nanoparticles were entrapped in the chitosan matrix, negative staining (without the use of any dye) was used. The dried grids were examined under the electron microscope (JEM 2010 with EDAX by JEOL, Peabody, MA) at a required magnification.

3.2.1.3 Selected Area Electron Diffraction

Selected Area Electron Diffraction (SAED) was performed to study the crystallinity of the nanoparticles embedded in the chitosan. SAED is a crystallographic experimental technique that can be performed inside most transmission electron microscopes (TEM). In a TEM, a thin crystalline specimen is subjected to a parallel beam of high-energy electrons. In most TEM measurements, thickness of the sample is kept below 100 nm to facilitate the flow of electron through. Because of the small sample thickness, and energy of the electrons in the range of 100–400 kilo-electron volts (keV), the electrons pass through the sample with minimal resistance. In this case, electrons are treated as wave-like, rather than particle-like. Because the wavelength of high-energy electrons is a few thousandths of a nanometer (for 20kV, 0.008 nm), and the spacing between atoms in a solid is about a hundred times larger, the atoms act as a diffraction grating to the diffracted electrons. That is, some fraction of electrons will be scattered at particular angles, determined by the crystal structure of the sample, while others continue to pass through the sample without deflection. As a result, the image on the screen of the TEM will be a series of spots which is known as the selected area diffraction pattern (SADP). Each spot corresponds to a satisfied diffraction condition of the sample's crystal structure. If the sample is tilted, the same crystal will stay under

illumination, but different diffraction conditions will be activated, and different diffraction spots will appear or disappear.

'S' in SAED is referred to as "*selected*" because the user can easily choose from which part of the specimen to obtain the diffraction pattern. Located below the sample holder on the TEM column is a selected area aperture, which can be inserted into the beam path. This is a thin strip of metal that will block the beam. It contains several different sized holes, and can be moved by the user. The effect is to block the entire electron beam except for the small fraction passing through one of the holes; by moving the aperture hole to the section of the sample the user wishes to examine, this particular area is *selected* by the aperture, and only this section will contribute to the SADP on the screen. **Figure 3.5** shows the schematic of the SAED technique.

As a diffraction technique, SAD can be used to identify crystal structures and examine crystal defects. It is similar to X-ray diffraction, but unique in a way that areas as small as several hundred nanometers in size can be examined, whereas X-ray diffraction typically samples areas several centimeters in size.
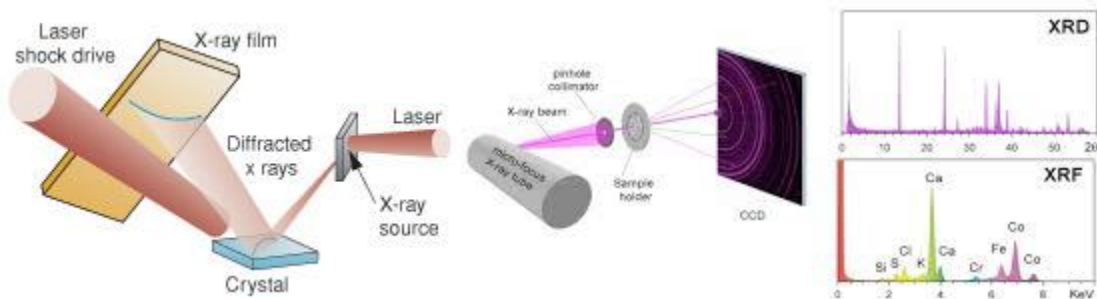
Figure 3.5 Schematic representation of SAED operating principle

A diffraction pattern is made under broad, parallel electron illumination. An aperture in the image plane is used to select the diffracted region of the specimen, giving

site-selective diffraction analysis. SAD patterns are a projection of the reciprocal lattice, with lattice reflections showing as sharp diffraction spots. In this work, SAED was performed in the same TEM instrument in which nanoparticles were characterized for their size.

3.2.1.4 Scanning Electron Microscopy

Scanning electron microscopy (SEM) is another tool used to characterize nano-sized domains of complex materials microstructures. To characterize nano- and micro-structure of cross-sections of the nanocomposite films, SEM was performed. SEM is a type of electron microscope that images the sample surface by scanning it with a high-energy beam of electrons in a raster scan pattern. The electrons interact with the atoms that make up the sample producing signals that contain information about the sample surface topography, composition and other properties such as electrical conductivity, etc. The electron beam hits the sample and produces secondary electrons from the sample surface (**Figure 3.6**). These electrons are collected by a secondary detector or a backscatter detector, converted to a voltage, and then amplified. The amplified voltage is applied to the grid of a monitor which causes the intensity of the spot of light on the display to change. The image consists of thousands of spots of varying intensity on the screen of a monitor that correspond to the topography of the sample. The types of signals produced by an SEM include secondary electrons, back-scattered electrons (BSE), characteristic X-rays, light (cathode-luminescence), specimen current and transmitted electrons. Though secondary electron detectors are common in all SEMs, it is rare that a single machine would have detectors for all possible signals. The signals result from interactions of the electron beam with atoms at or near the surface of the sample. In the

most common or standard detection mode, secondary electron imaging or SEI, SEM can produce very high-resolution images of a sample surface revealing details with spatial resolution less than 1 nm to 5 nm.

In the present work, SEM analysis of the samples was done on JSM-7200-F (JEOL, Peabody, MA) Field Emission Scanning Electron Microscope (FE-SEM) **(Figure 3.6)**. Gold-chitosan nanocomposite films were cut and placed vertically underneath the electron beam column to observe the gold nanoparticles distribution and size throughout the cross-section.

3.2.1.5 Electron Diffraction Spectroscopy

Energy-dispersive X-ray spectroscopy (EDS, EDX, or XEDS), sometimes called energy dispersive X-ray analysis (EDXA) or energy dispersive X-ray microanalysis (EDXMA), is an analytical technique used for elemental analysis or chemical characterization of a sample. It relies on an interaction of some source of X-ray excitation and a sample. Its characterization capabilities are due in large part to the fundamental principle that each element has a unique atomic structure allowing unique set of peaks on its X-ray spectrum. To stimulate the emission of characteristic X-rays from a specimen, a high-energy beam of charged particles such as electrons or protons, or a beam of X-rays, is focused into the sample being studied. At rest, an atom within the sample contains ground state (or unexcited) electrons in discrete energy levels or electron shells bound to the nucleus. The incident beam may excite an electron in an inner shell, ejecting it from the shell while creating an electron hole at the place of electron.
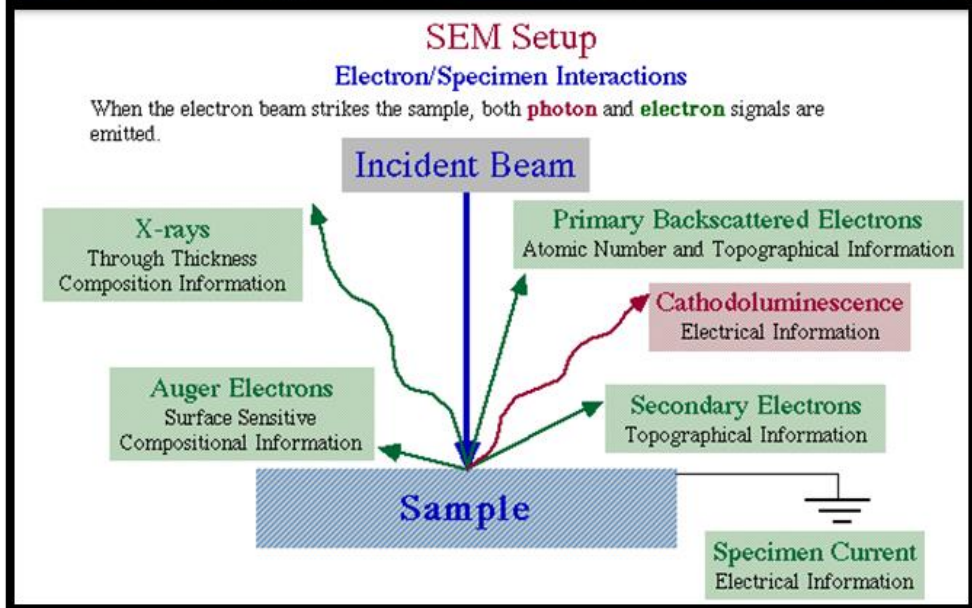
Figure 3.6 SEM instrument JEOL JSM-7200-F (top) and a simplified illustration of the working mechanism (bottom) [67]

An electron from an outer, higher-energy shell then fills the hole, and the difference in energy between the higher-energy shell and the lower energy shell may be released in the form of an X-ray. The number and energy of the X-rays emitted from a specimen can be measured by an energy-dispersive spectrometer. As the energy of the X-rays is characteristic of the difference in energy between the two shells, and of the atomic structure of the element from which they were emitted, this allows the elemental composition of the specimen to be measured. Four primary components of the EDS setup are:

1. Excitation source (electron beam or x-ray beam)

2. X-ray detector

3. Pulse processor

4. Analyzer

Electron beam excitation is used in electron microscopes, scanning electron microscopes (SEM), and scanning transmission electron microscopes (STEM). A detector is used to convert X-ray energy into voltage signals; this information is sent to a pulse processor, which measures the signals and passes them onto an analyzer for data display and analysis. The most common detector now is Si (Li) detector cooled to cryogenic temperatures with liquid nitrogen; however newer systems are often equipped with silicon drift detectors (SDD) with Peltier cooling systems.

3.2.1.6 FT-IR

To identify the functional groups present in a molecule, infrared spectroscopy is a very efficient tool for their qualitative analysis. The technique requires a source that generates light across the spectrum of interest and a mono-chromator salt prism (grating) which separates the source radiation into its different wavelengths (**Figure 3.7**). A slit

selects the collection of wavelengths that shine through the sample at any given time which is collected by detector.

FT-IR spectra of the samples were recorded using a model Perkin Elmer (Waltham, MA) FT-IR system. Spectra were recorded with a Perkin Elmer Spectrum 10 software in the range 4000-400 cm^{-1}. The KBr pellet technique has been most commonly adopted for recording the spectra. However, in this work, the nanocomposite films were characterized directly in their free standing state.
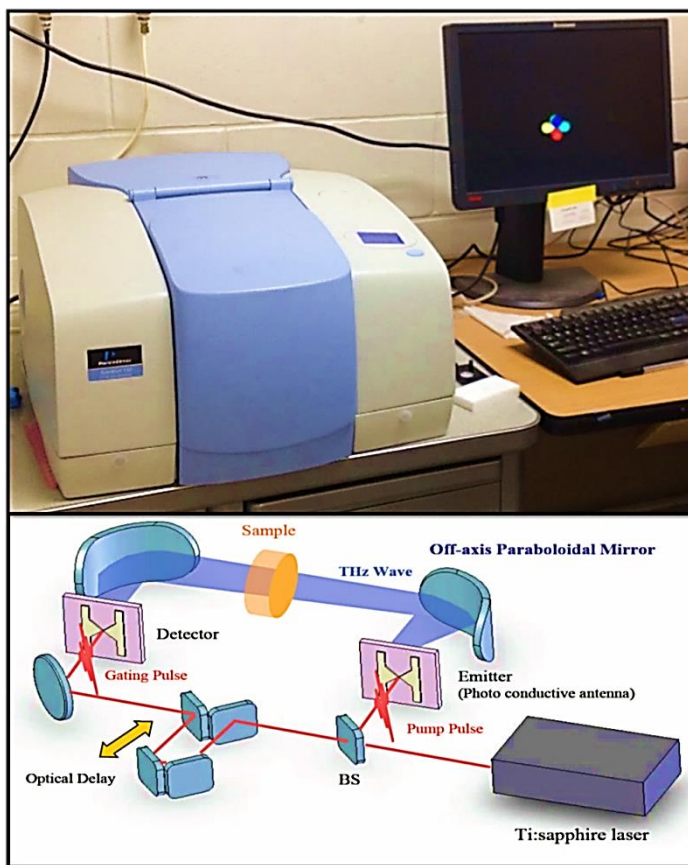
Figure 3. 7 FT-IR instrument used in this study (Top), and Schematic of the operation (Bottom) (Source: www.riken.jp/.../THz-img/English/annual_gas.htm)

3.2.1.7 X-ray Diffraction

X-ray diffraction is a versatile, non-destructive analytical technique for identification and quantitative determination of the various crystalline forms, known as '*phases*' of the compounds present in powdered and solid samples. Identification is achieved by comparing the X-ray diffraction pattern, or 'diffractogram', obtained from an unknown sample with an internationally recognized database containing reference patterns. Modern computer-controlled diffractometer systems use automatic routines to measure, record, and interpret the unique diffractograms produced by individual constituent even in highly complex mixtures. When a monochromatic X-Ray beam (**Figure 3.8**) with wavelength λ is applied on lattice planes in a crystal at an angle θ, diffraction peaks occurs when the distance travelled by the ray reflected from successive planes differ by a complete number (n) of wavelengths. This is described by Bragg's **Equation 3.1**:

$$n\,\lambda = 2\mathrm{d}\sin\theta \;\ldots\ldots\ldots\ldots\ldots\ldots\ldots\ldots\ldots\ldots.. \; 3.1$$

here, d is the spacing between the lattice planes. By varying the angle "θ", Bragg's equation is satisfied by different "d" spacing in polycrystalline materials. A diffractometer collects intensities over an angular range by measuring 2θ, the angle between the incident and the reflected beam. The resulting plot of the intensity as a function of the 2θ value is known as a diffractogram and can be used to identify the phases (qualitative information), their atomic arrangement (structural information), their relative concentration (quantitative information), as well as the possible presence of a known crystalline amorphous phase. The widths of the peaks of a particular phase pattern

provide an indication of the average crystallite size. Crystalline materials produce sharp characteristic peaks, while amorphous materials results in broad humps. Peak broadening also occurs by variations in 'd' spacing caused by micro-strain. The XRD can be used to determine the size of the nanoparticles by using Sherrer's equation as given below (**Equation 3.2**):

$$d = \frac{0.9\lambda}{B \cos\theta_B} \quad \ldots\ldots\ldots\ldots\ldots\ldots\ldots\ldots\ldots\ldots\ldots\ldots\ldots..3.2$$

where, d = Particles diameter

λ = Wavelength of X-ray (Cu-Kα radiation)

B = Full width at half maximum (FWHM)

θ_B = Diffraction angle (θ_2 -θ_1)

In the present work, X-ray diffraction analysis of the samples were carried out using Bruker D8 (Madison, WI) equipped with a 2θ compensating slit, Cu-Kα radiation (1.54Å) at 40 kV, 40 mA passing through Nickel filter with a wavelength of 0.154 nm at 20 mA and 35 kV. Nanocomposite films were prepared on 1" x 1" glass slides with thickness of ~100 nm. Data collection was performed in a continuous scan mode with a step size of 0.01° and step time of 1 sec over a 2θ range of 0° to 70°. Data analysis was performed with Bruker's DIFFRAC.SUITE™ Software.
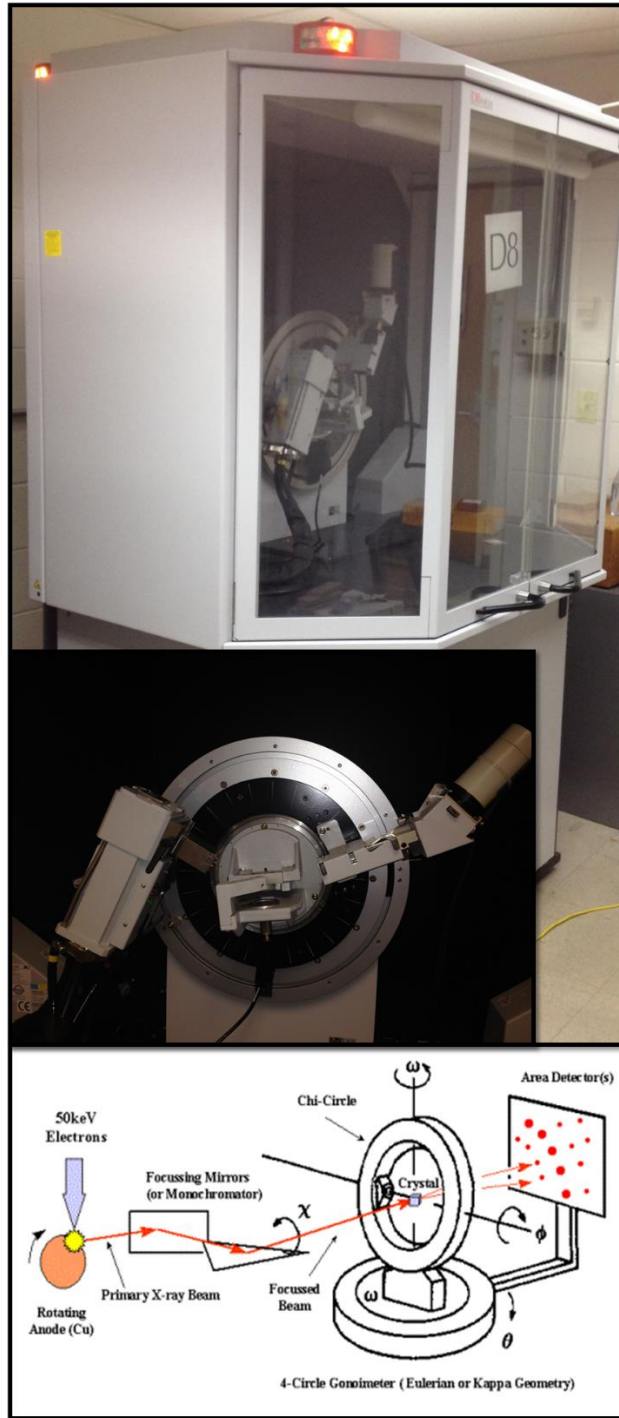
FIgure 3.8 Bruker D8 XRD instrument used in this study (Top), and Schematic representation of the operation (http://ruppweb.dyndns.org/)

3.2.1.8 Zeta-Potential

Zeta potential is a measure of electrical charge associated with the surface of particle/molecules in a medium. It has a practical significance in the research of suspensions of particles in aqueous or non-aqueous media. The relative instability of a suspension, i.e. the tendency of the solid particles to flocculate (aggregate) - or not - is a function of zeta potential (ZP). It gives a good measure to estimate the stability of the nanoparticles in the suspending media. Depending on the application, the particle's zeta potential needs to be within or out of certain limits. For example, the behavior of particles coming together (when ZP is in a range, typically -30mV to +30mV) is considered to be required in the area of water purification. Conversely, an oral pharmaceutical formulation should maintain its dispersed colloidal state, that is, it should exhibit a high zeta potential value, to ensure proper dosing of the active ingredient (a.i.) [68]. Zeta potential is an important material property in many other areas of science and technology including, but not limited to, fine ceramics, geology and mining, food and beverages, biosciences, chemicals and polymers, cosmetics, inks and paper pulp.

In this work on chitosan reinforced nanocomposites, the stability and good dispersion of the gold nanoparticle are desired to get uniform distribution of the nanoparticles throughout the chitosan matrix. The Zeta Potential measurements were carried out on ZetaPALs (Brookhaven Instruments, Holtsville, NY) employing a nominal 5 mW He-Ne laser operating at 633 nm wavelength (**Figure 3.9**). The scattered light was detected at 135° angle. The refractive index (1.33) and the viscosity (0.89) of ultrapure water were taken at 25 ℃ for measurements. All the data analyses were performed in automatic mode. Measured size range was presented as the average value of 4 runs.
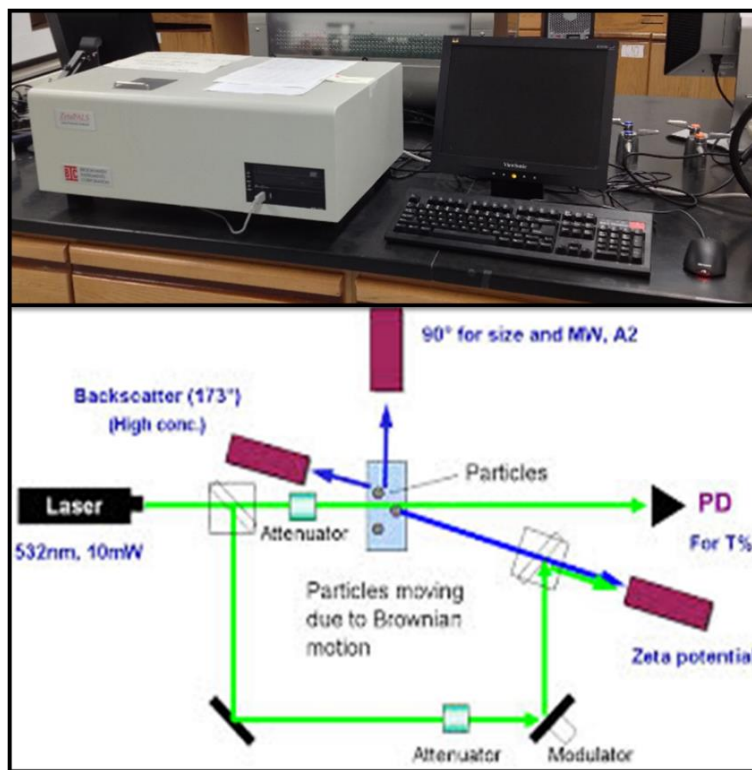
Figure 3.9 Zeta potential and particle size analyzer instrument (Top) and schematic of the operation (Bottom)

3.2.1.9 Particle size analysis

The photon-correlation spectrometer is based on the Photon Correlation Spectroscopy (PCS) technique and is designed for the measurements of sub-micron particle sizes, diffusion coefficients, viscosities and molecular weights of polymers in basic and applied studies.

The PCS method consists of determining the velocity distribution of the movement of particles by measuring dynamic fluctuations of the intensity of the scattered light. The dispersed particles (or macromolecules suspended in a liquid medium) undergo Brownian

motion and this causes the fluctuations in the local concentration of the particles, resulting in local inhomogeneity of the refractive index. This in turn results in fluctuations in the intensity of the scattered light. The line-width of the light scattered spectrum Γ (defined as the half-width at half-maximum) is proportional to the diffusion coefficient of the particles D (**Equation 3.3**):

$$\Gamma = D\,q^2 \dots\dots\dots\dots\dots\dots\dots\dots\dots\dots\dots 3.3$$

where,

$$q = \frac{4\pi n}{\lambda}\sin\left(\frac{\theta}{2}\right)\dots\dots\dots\dots\dots\dots\dots\dots\dots\dots\dots 3.4$$

n is the refractive index of the medium, λ laser wavelength of the laser, and θ the scattering angle. With the assumption that the particles are spherical and non-interacting in nature, the mean radius can be obtained from the Stokes-Einstein **Equation 3.5**

$$R_h = \frac{k_b T}{6\pi\eta D}\dots\dots\dots\dots\dots\dots\dots\dots\dots\dots\dots 3.5$$

where, k_B is the Boltzmann constant, T the temperature in °K and η the shear viscosity of the solvent.

In this work, particle size measurements for determining the size distribution of the gold nanoparticles were performed using a Brookhaven particle size analyzer (**Figure 3.9**) instrument. The gold suspension was diluted to make a translucent medium and then, placed in the instruments specimen cuvette holder for the characterization. Five readings were taken for the particle size analysis studies.

3.2.2 Mechanical Characterization

Mechanical stability is one of the most important aspects of materials used in structural applications. Critical functions of the materials in the fields such as biomedical,

electronics, water treatment and food packaging rely considerably on the mechanical strength and stability of the material. For example, chitosan scaffold for skin grafting needs certain mechanical stability and flexibility to be physically compatible with the native tissues in wound healing application [69]. Protective layers made of chitosan thin films on perishable food need certain strength to withstand forces applied during packaging, transportation, handling and storage.

Cell-tissue interactions are initiated at nanoscale when chitosan is used as a biomaterial. Macro-scale mechanical properties do not give enough information about the structural performance of the material at nanoscale. Nanoindentation is a useful tool to qualitatively characterize materials nanomechanical properties with a very high accuracy. Moreover, nanoindentation is a quasi-nondestructive test with a very high spatial resolution. In this work, mechanical properties of GNP-Chitosan nanocomposites films were characterized using nanoindentation.

3.2.2.1 Nanoindentation

For thin-films and small volume systems, nanoindentation is a popular technique to pullout important information about the mechanical properties. Nanoindentation sometime is also called as depth sensing indentation or instrumented indentation. The principle goal is to extract the reduced modulus and hardness by indenting materials with known geometry indenters, and recording indentation depth and applied load through instrumentation. Normal size of the indents ranges from nano to sub-micron level. Because it is almost impossible to visualize the indents with naked eye, nanoindentation

is considered as quasi-nondestructive technique. A schematic of nanoindenter is shown in **Figure 3.10**.

Nanoindenter instrument primarily consists of a heavy load frame to minimize the effects of external vibrations by acting as a seismic mass. The loading frame supports majority of essential elements of the instrument including specimen holder, transducer and indenter shaft. Indenter shaft is typically made of a stiff and lightweight material so that the compliance can be reduced, and the resonant frequency of the system is maximized [70]. The shaft holding the indenter tip is attached with an electromagnetic force motor to apply controlled load to the specimen, and is mounted on the supporting springs. For sensing displacement, a two parallel plate capacitive displacement transducer is commonly used. The noise errors could be reduced considerably by using large plates separated by a small distance. With advanced development in the nanoindentation test instrumentation, various experimental techniques such as quasi-static (simple loading and unloading), dynamic (cyclic oscillatory force and displacements), creep (prolonged loading) and relaxation (prolonged deformation) can be used to evaluate materials performance characteristics for various applications.
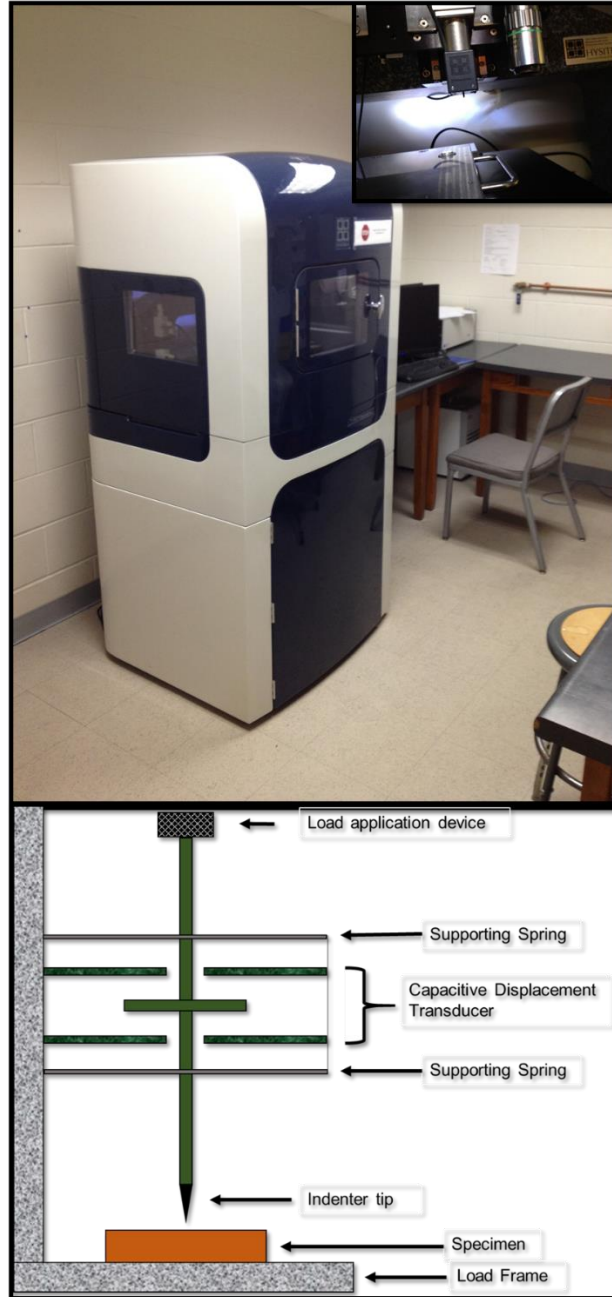
Figure 3.10 Nanoindenter instrument (Top) and Instrument schematic (Bottom)

3.2.2.1.1 Quasi-static nanoindentation

In quasi-static nanoindentation, materials surface is indented with known load or displacement and the resultant displacement or load required is evaluated to deduce

material's mechanical properties. Elastic modulus and hardness are the properties widely extracted from the standard quasi-static nanoindentation test. Classical methods of indentation tests such as Rockwell, Brinnel, Vickers and Mayer hardness tests involves analysis of the indent impression dimensions to calculate hardness of the material. In general, nanoindentation tests are carried out by controlled deformation of the specimen surface with a known geometry indenter. The indentation impression size is often in the scales of several micrometers which makes it very difficult to be evaluated by optical techniques, however, that makes the technique quasi non-destructive. In nanoindentation experiments, the indentation displacement is recorded as a result of the load applied or *vice-versa*. Since the geometry of the indenter is known, it is easy to calculate area of contact of the indenter tip with the sample during the complete indentation period. The rate of change of load with respect to displacement is used to calculate the contact stiffness. The contact area is determined from a very well calibrated tip-area function. From the calculated contact stiffness and known contact area, the elastic modulus of the specimen can be determined. The commonly used indenter geometries are flat punch, pyramidal and spherical. Pyramidal probes with geometries such as conical, berkovich and cube corner are considered sharp probes. The surface region probed with the sharp indenters is prone to plastic deformation because of concentrated localized stresses. To avoid plastic deformation of the specimen surface during indentation, and to capture the response of greater number of GNPs, in this work, a cono-spherical tip with radius of curvature 99.56 μm was used.

Figure 3.11 shows the load function used to perform indent on chitosan nanocomposite films. It consists of loading, hold and unloading segments. The loading

and unloading rates are 7500 µN/s and hold period is 32 seconds. **Figure 3.12** shows the resulting load-displacement plot obtained from the indentation test. In **Figure 3.12,** P_{max} is maximum load applied which, in this case, is 7500 µN, h_{max} is the resulting maximum penetration depth as a result of maximum load and holding time, h_c is contact depth of the indent and h_f is the final depth after all the forces are removed from the specimen surface.
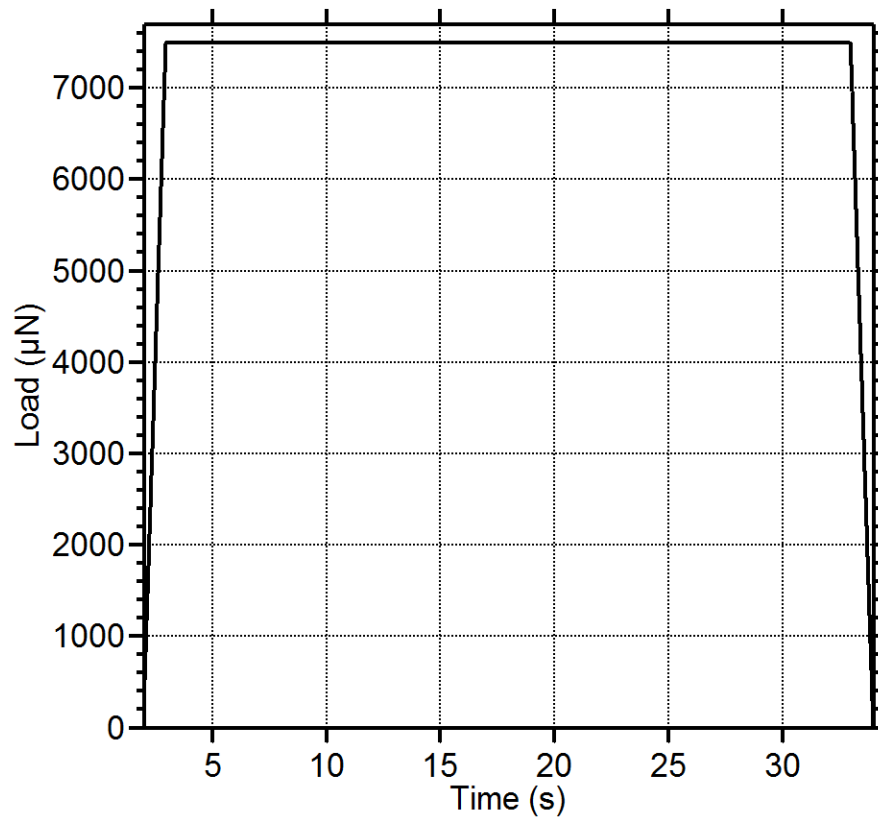
Figure 3.11 Quasi-static load function (Indentation Load vs. Time)

Holding time has a great influence on indentation depth especially in case of polymers due to creep effect. The creep effect and analysis are discussed in-depth in the later sections of this chapter. The slope of the unloading curve from the maximum load is

the contact stiffness of the material. Contact depth h_c can be determined from **Equation 3.6.**

$$h_c = h_{max} - 0.75 \times \frac{P_{max}}{S} \dots\dots\dots\dots\dots\dots\dots\dots\dots\dots\dots\dots\dots 3.6$$
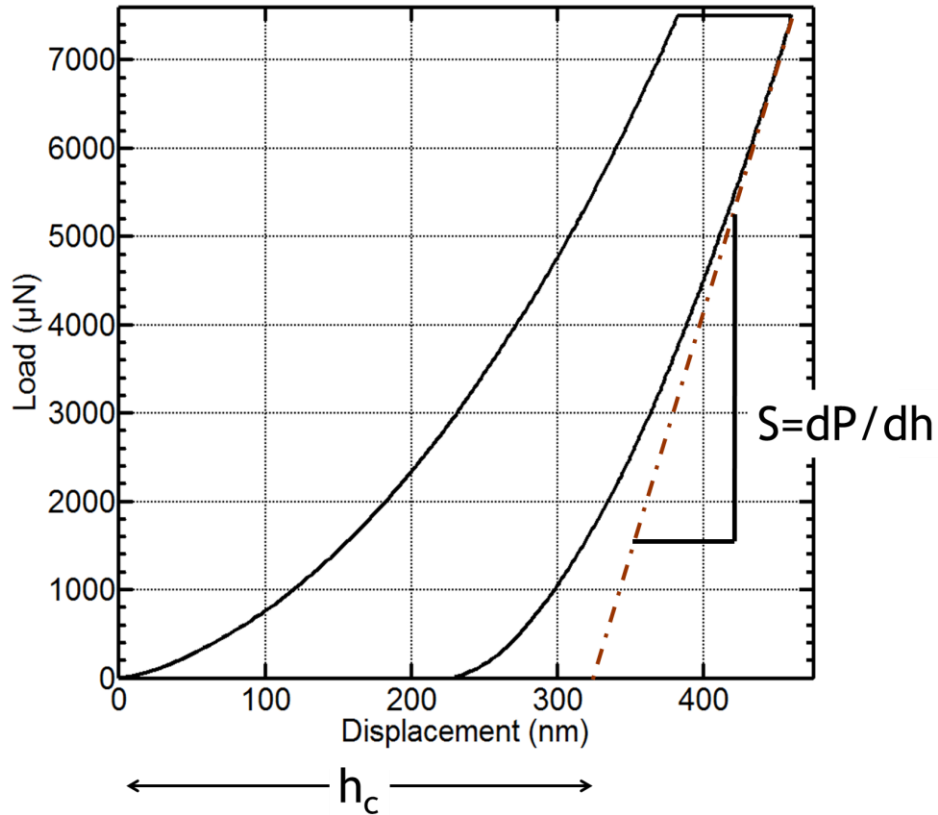
Figure 3.12 Indentation load vs. displacement plot

As previously discussed, the known geometry indenters are used in the instrumented indentation (nanoindentation) testing, the area of contact at contact depth h_c is known. For spherical indenters the depth vs. contact area can be expressed as in **Equation 3.7**.

$$A_c = C_0 h_c{}^2 + C_1 h_c \dots\dots\dots\dots\dots\dots\dots\dots\dots\dots\dots\dots\dots 3.7$$

where, A_c is the area of contact at contact depth h_c. C_0 is a geometric conctant. For sperical indenters, C_0 is $-\pi$ i.e. -3.14 and C_1 is $2\pi R$ (R is a radius of the tip). With the use of contact area A_c and stiffness S, the reduced modulus (E_r) of the materials can be calculated from **Equation 3.8** [71].

$$E_r = \frac{\sqrt{\pi}}{2 \times \sqrt{A}} \times S \dots\dots\dots\dots\dots\dots\dots\dots\dots\dots\dots\dots\dots\dots 3.8$$

The reduced modulus is related to the youngs modulus of the material by:

$$\frac{1}{E_r} = \frac{(1-v_i{}^2)}{E_i} + \frac{(1-v_s{}^2)}{E_s} \dots\dots\dots\dots\dots\dots\dots\dots\dots\dots\dots 3.9$$

here, E_i and E_s represent young's modulus of the indenter and the sample, respectively. Similarly v_i and v_s are Poisson's ratios of the indenter-tip material, and the sample, respectively.

3.2.2.1.2 Dynamic Nanoindentation

The manner in which solid materials resist physical deformation classifies the material in three major categories; a) elastic, b) viscous and c) visco-elastic. Elastic material deforms under the effects of applied load, stores energy, and upon releasing the load, regains its original shape. The stresses developed in the material are proportional to the loads applied. Viscous materials on the other hand deform under the influence of applied load, dissipate energy in the form of heat, and do not recover their original shapes upon removal of the applied load. The stresses developed because of the deformation are proportional to the rate of change of deformation. A viscoelastic material behaves like the one with combination of viscous and elastic material. Polymers fall under the category of viscoelastic materials.

More generally, in order to determine viscoelastic material properties, the material of interest is often subjected to oscillatory forces and viscoelastic properties derived from the material response. Recent development in nanoindentation instrumentation has made it possible to characterize viscoelastic properties of the materials at nano and micron scales. Dynamic nanoindentation method involves applying oscillatory force (using AC current) superimposed onto a quasi-static load (using DC current) on the specimen surface, and recording resulting displacement to determine viscoelastic properties [72-74]. Holding constant load for a period of time and recording resulting displacement (creep) and holding constant displacement in to the materials surface and recording change in the reaction force (stress relaxation) are other methods of characterizing mechanical properties. Indentation creep and stress relaxation will be discussed in the later parts of this chapter.

In dynamic nanoindentation, a simple harmonic oscillation is applied to the system by applying load "P_t" and resulting displacement h_t and phase φ are measured (**Figure 3.13**).
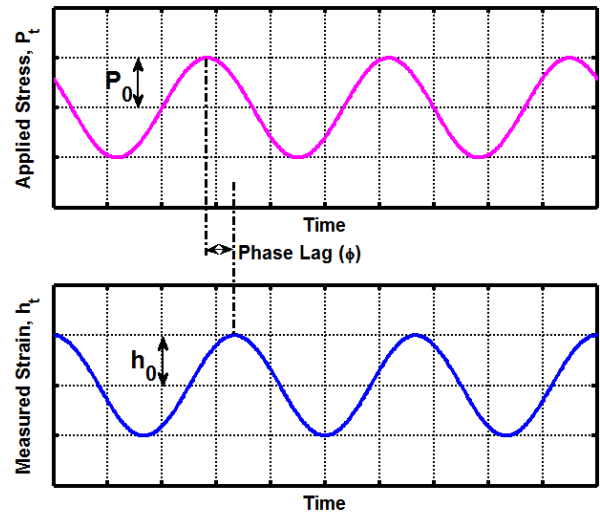
Figure 3.13 Dynamic load, dynamic displacement and phase lag

The test can be performed by applying a small sinusoidal force superimposed on a relatively large static force. The response in terms of amplitude and phase is captured by a lock-in amplifier. The dynamic compliance of the system can be determined by the **Equation 3.10** [74].

$$\left|\frac{X_0}{F_0}\right| = \left\{ \left(k_i + k_{\text{storage}} - m\omega^2\right)^2 + (\omega c_i + k_{\text{loss}})^2 \right\}^{-\frac{1}{2}}, \ldots\ldots\ldots\ldots 3.10$$

Similarly, the phase shift between the applied force amplitude and the resulting displacement amplitude can be expressed by,

$$\tan(\phi) = -\frac{(\omega c_i + k_{\text{loss}})}{(k_i + k_{\text{storage}} - m\omega^2)} \cdots\cdots\cdots\cdots\cdots\cdots\cdots\cdots\cdots 3.11$$

here, F_0 is the applied force amplitude, X_0 is the resultant displacement amplitude, k_i is the stiffness of the indenter supporting spring (See **Figure 3.14**), c_i is the damping

coefficient of the indenter instrumentation, and m is the mass of the indenter. $k_{storage}$ and k_{loss} are the storage and loss stiffness of the specimen respectively.

Within the limits of linear viscoelasticity, the elastic-viscoelastic correspondence principle is used to relate the stiffness of the material to the modulus. From Hertzian [75] contact mechanics theory, the storage indentation modulus (M') is expressed as

$$M' = \frac{E'}{1-\nu^2} = \frac{k_{storage}}{2}\sqrt{\frac{\pi}{A_c}} \dots\dots\dots\dots\dots\dots\dots\dots\dots\dots\dots 3.12$$

and, the loss indentation modulus (M'') is given by

$$M'' = \frac{E''}{1-\nu^2} = \frac{k_{loss}}{2}\sqrt{\frac{\pi}{A_c}} \dots\dots\dots\dots\dots\dots\dots\dots\dots\dots\dots 3.13$$

where, ν is the Poisson's ratio, A_c is the area of contact between tip and sample, and E' and E'' are the storage and loss moduli, respectively.

The loss factor is a useful measure of the relative contributions of the storage and loss moduli to the mechanical response which is defined as

$$\tan(\delta) = \frac{k_{loss}}{k_{storage}} \cdot \dots\dots\dots\dots\dots\dots\dots\dots\dots\dots\dots 3.14$$

Loss factor is a measure of damping in a linear viscoelastic material. Loss factor value higher than the unity (tan (δ) > 1) indicates a predominantly viscous or fluid like behavior whereas a value lower than the unity (tan (δ) < 1) indicates a predominantly solid-like response. Since the errors associated with the tip-sample contact area cancels out while calculating the loss factor, it becomes very advantageous in the analysis of dynamic nanoindentation.

Before analyzing dynamic nanoindentation results, the instrument parameters such as the mass of the indenter (m), supporting spring stiffness (k_i), and system damping coefficient (c_i) must be known. Instrument parameters can be determined by performing systematic calibrations before beginning tests. The standard procedure involves oscillating the indenter tip with a wide spectrum on frequencies without any contact with the sample, and measuring dynamic compliance (ratio of displacement amplitude by force amplitude) (**Equation 3.10)** and/or phase shift (**Equation 3.11**) between the load amplitude and the displacement amplitude. The system parameter constants can be obtained by zeroing sample storage stiffness ($k_{storage}$) and loss stiffness (k_{loss}) in **Equation 3.10** and fitting dynamic compliance throughout the frequency sweep. **Equation 3.11** for phase could also be used with the similar approach to determine the instrument constants.

The moduli values obtained through the dynamic nanoindentation greatly depend on the way contact stiffness expressions are derived from various viscoelastic models. The most commonly used viscoelastic model to analyze dynamic nanoindentation results is two parameter Kelvin-Voigt model.

3.2.2.1.2.1 Kelvin-Voigt model

The common way to model the tip-sample viscoelastic contact forces is by Kelvin-Voigt model (or Voigt model). With Kalvin-Voigt model, the tip-sample contact is represented by a Hookean spring with stiffness "k_s" connected in parallel with a Newtonian damper with damping coefficient "c_s" as shown in the highlighted region in

Figure 3.14. k_i and c_i represent nanoindenter instrument stiffness and damping respectively. "*m*" is the mass of the indenter.
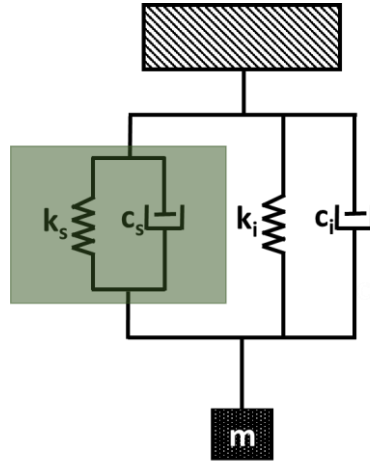
Figure 3.14 Model showing Kelvin-Voigt solid used to model tip sample contact forces

The energy stored in spring is proportional to the load exerted as a result of mass "*m*", and resistance offered by damper is proportional to the rate of deformation of the damper. When load is released, the system is restored to its original shape as a result of forces exerted by the spring. Time required to relax all the stresses in the system depends on the resistance of the damper "c_s". The storage stiffness evaluated from the two parameter Kelvin-Voigt model is simply k_s, while the loss stiffness is $c_s\omega$, here ω is the frequency of oscillation of the indenter.

3.2.2.1.3 Nanoindentation creep and stress relaxation

Stress relaxation and creep effect are essential to be analyzed in order to investigate the time-dependent viscoelastic properties of polymers. To investigate the influence of nanostructure incorporation and nanostructure content on time-dependent

performance of the gold-chitosan bionanocomposites, viscoelastic creep and stress relaxation experiments are performed using instrumented nanoindentation. The long term mechanical stability is a major concern for viscoelastic materials such as chitosan bionanocomposites used in biomedical applications.

3.2.2.1.3.1 Nanoindentation creep tests

Creep testing is another useful technique to predict time-dependent response of the materials under continuous deformation. When a polymeric material is strained under the influence of constant load, it deforms continuously and the rate of deformation tends to zero as the loading time in increased. This phenomenon is known as creep. Indentation depth is not linearly dependent on the load in a viscoelastic material. Time-dependent properties of viscoelastic materials for applications involving prolonged loadings cannot be determined by classical mechanical or nanomechanical testing and hence, nanoindentataion creep analysis is desired [76-82]. In nanomechanical testing, the magnitude and rate of applied load have significant influence on the manner in which material deforms.

For performing creep tests in this study, the indenter was abruptly loaded to 11000 μN in 1 second, which was then maintained constant for 30 seconds before unloading at the same rate as that of loading. The indenter thereupon moves continually, which is called creep. After a sufficient amount of time was experienced, the indentation depth and strains in the material were finally stabilized and did change with the hold time. This is how creep behavior in viscoelastic materials were observed by holding certain magnitude load for a period of time and recording resulting deformation.

Systematic approaches based on simple representative spring and dashpot models are used to deduce meaningful results through viscoelastic creep experiments on wide range of polymers. The most widely used model for analyzing the viscoelastic creep data is generalized Kelvin-Voigt model. **Figure 3.15** shows load function used to perform creep tests on the gold-chitosan nanocomposite specimens and the resulting displacement. **Figure 3.16** shows an elastic-viscoelastic type of model with multiple Kelvin-Voigt solids arranged in series; also known as generalized Kelvin model. Creep behavior is a very important property of a viscoelastic composite that controls its dimensional stability, especially in applications where the material has to support loads for long periods of time. [32]
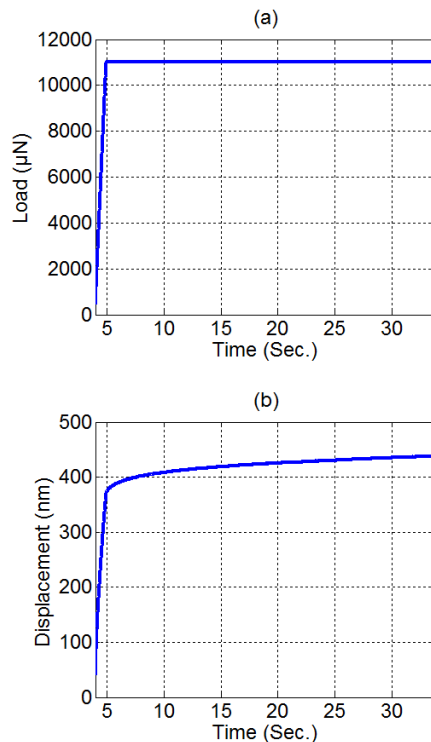
Figure 3.15 (a) Indentation creep load function, and (b) a typical indentation creep curve

54
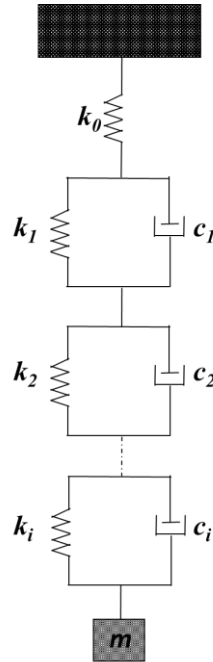
Figure 3.16 Model of Voigt solids arranged in series for viscoelastic creep analysis

Such model is used to derive equations used for viscoelastic creep analysis. Ideally, the creep curve should be obtained by a step loading of the sample followed by holding of the load for extended period of time. However, ideal step loading needs increasing the force to its desired maximum value and is not possible to achieve the infinite loading rate with any testing instrument. Oyen et al. [80] derived **Equations 3.17** and **3.18** by taking loading ramp rate in to consideration for viscoelastic creep analysis as:

$$h^{3/2}(t) = \frac{3k}{8\sqrt{R}}\{C_0 t - \sum C_i \tau_i [1 - \exp(-t/\tau_i)]\}, \ when \ 0 \leq t \leq t_R \ ....3.17$$

$$h^{3/2}(t) = \frac{3k}{8\sqrt{R}}\{C_0 t_R - \sum C_i \tau_i \exp(-t/\tau_i)[\exp(t_R/\tau_i) - 1]\}, \ when \ t \geq t_R \ ...3.18$$

In **Equations 3.17** and **3.18**, *h(t)* is the depth of the indentation at time *t*, *k* is the loading rate, C_0 is compliance of the spring with stiffness K_0, C_i is the compliance of the spring, and τ_i is retardation time as a result of dashpot resistance in the ith Kelvin model in the

system, (see **Figure 3.17**). t_R is the time required to increase the load to its maximum value. The maximum load is given by

$$P_{max} = kt_R \ldots\ldots\ldots\ldots\ldots\ldots\ldots\ldots\ldots\ldots\ldots\ldots\ldots.3.19$$

Equations 3.17 and **3.18** will be used to fit experimental data to deduce creep parameters.

3.2.2.1.3.2 Nanoindentation stress relaxation tests

Stress relaxation occurs when reorganization of the structure to reach the thermodynamic equilibrium after a perturbation happens. It involves structural changes at different length scales, and the required time, called relaxation time, is on a wide range of time scales. Upon deformation of viscoelastic materials at constant strain, the instantaneous stress decays over a period of time. This effect is called viscoelastic relaxation. In polymers, viscoelastic relaxation is the result of relaxation and rearrangement of molecular chains and segments. Viscoelastic stress relaxation is a very useful measure in designing materials for various applications. It represents the stability of the materials with respect to deformation over extended period of time under continuously applied strain. Traditionally, the load is applied to the material of interest in tension, compression or in flexural mode. The load function in **Figure 3.17** shows that the Chitosan films are subjected to a strain-versus-time profile with the spherical tip and the resulting stress- versus-time profile is recorded. The films were indented with a displacement of 300 nm ramped in 1 second and the tip was held at the same depth for 30 seconds before unloading. **Equation 3.21** derived by Yuya et al. [83] with the use of

generalized Maxwell model (**Figure 3.18**) were used to evaluate relaxation parameters of the chitosan films.

In **Equations 3.20** and **3.21**, *P(t)* and *E(t)* are the resultant load and relaxation modulus, respectively, h_0 is the applied constant strain, *R* is the radius of spherical indenter, E_∞ is the long term modulus of the material.

$$P(t) = \frac{4h_0^{3/2}\sqrt{R}}{3} \times E(t) \quad\text{..3.20}$$

$$\text{where, } E(t) = \left[E_\infty + \sum_{j=1}^{m} E_j\, e^{-t/\tau_j}\right]\text{..3.21}$$
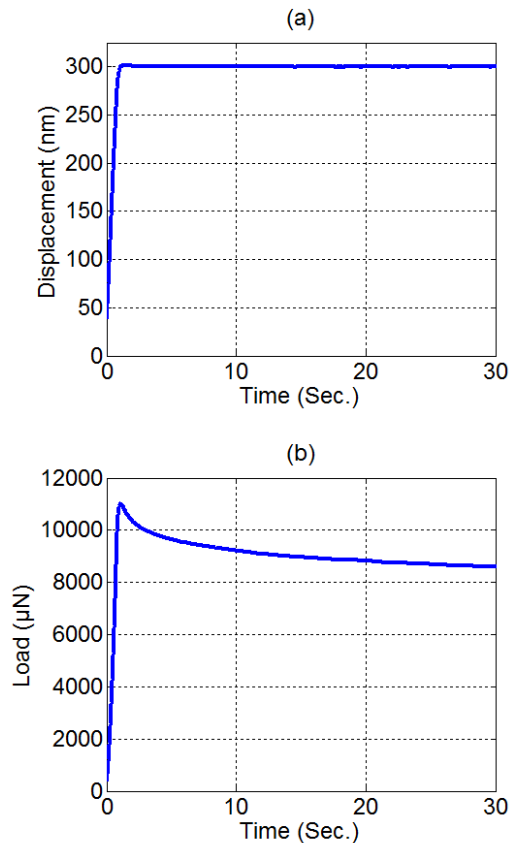
Figure 3.17 (a) Indentation relaxation load function, and (b) a typical indentation relaxation curve
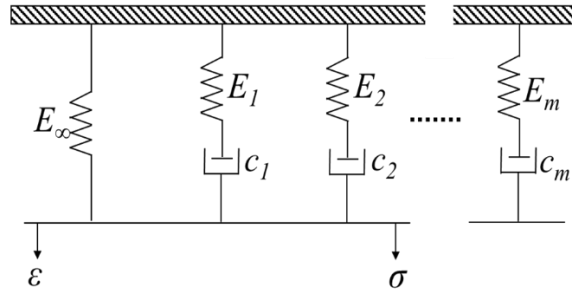
Figure 3.18 Generalized Maxwell Model

3.2.2.1.4 Plasticity index determination *via* nanoindentation

When a polymeric material is deformed, it stores and dissipates fractions of energy during the phenomena of the total work done. Elastic deformation is a function of energy stored and plastic strains are the function of energy lost in the form of heat. The plasticity index is the measure of a relative elastic/plastic nature of a solid material when it undergoes elastic-viscous-plastic deformations under the influence of external load. Nanoindentation can be used to quantitatively determine plasticity index of the viscoelastic materials at nano and micro scales. The loading curve represents the load required to overcome elastic and plastic resistances of the specimen surface. The unloading curve mostly represents the elastic recovery of the materials. Both, loading and unloading curves can be analyzed to evaluate materials elastic and plastic response due to the applied load or strain.

Figure 3.19 shows effect of materials nature on quasi-static nanoindentation curves. For completely elastic materials, loading and unloading curves fall on the same path (**Figure 3.19a**). In other words, upon unloading the material, it gains its original shape. For a perfectly plastic material, loading curve goes to the maximum load value and

upon unloading, does not recover its original shape (**Figure 3.19b**). Materials exhibiting

both elastic and plastic nature show partial recovery of shape upon unloading (**Figure**

3.19c). Most (almost all viscoelastic) materials fall under this category. Energy stored or

lost can be evaluated by analyzing areas under the loading and unloading curves. For

example, in **Figure 3.19c**, area A_1 represents the energy lost because of the plasticity of

the material during the indentation cycle, and area A_2 is the function of energy recovered

because of elastic nature of the material.
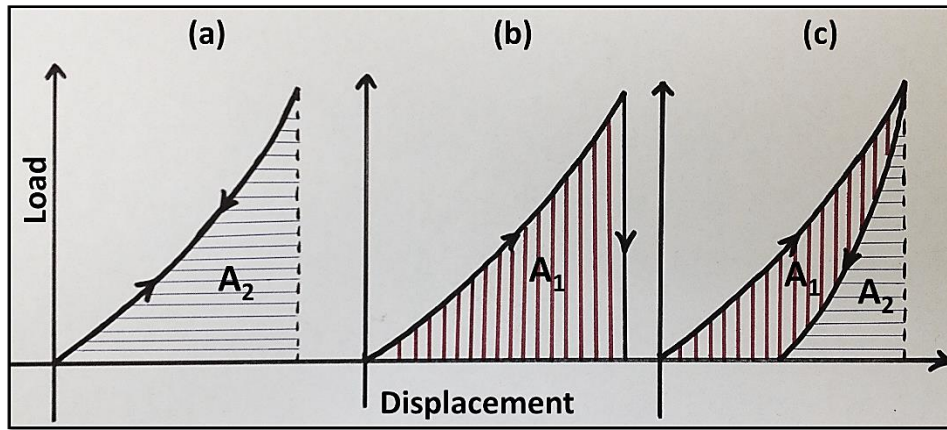
**Figure 3.19 Representation of (a) elastic, (b) plastic, and (c) elastic-plastic response
of materials by nanoindentation curves**

In **Figure 3.19a** and **3.19b,** for elastic materials, the complete recovery of the

energy is shown by the absence of area A_1, and similarly, for plastic materials, the

complete loss of energy is observed by looking at the area A_1. Plasticity index (Ψ) can be

expressed by following **Equation 3.22** [84].

$$\psi = \frac{A_1}{A_1 + A_2} \quad \dots\dots\dots\dots\dots\dots\dots\dots\dots\dots 3.22$$

The plasticity index (ψ) can vary between 0 and 1, where $\psi = 0$ indicates the fully-elastic

behavior and $\psi = 1$ represents fully-plastic behavior of the material.

3.3 Biocompatibility testing

Even though the main focus of this work on chitosan is to improve its properties and widen the application areas in the biomedical filed, it is of prime importance to see whether the nanocomposites are able to proliferate human body tissue cells. If the films prepared are not biocompatible, there is no use of improving its mechanical stability using gold nanoparticle for targeting their potential applications in the biomedical field. After preparing chitosan films with different gold concentrations, and with various chemical processing, it is desired to confirm their biocompatibility.

For that, cell culture experiments were performed in a controlled environment. Cell culture is the technique to remove cells from complex environment of the body and perform desired experiments in a controlled environment to see the nature of the materials on living cells. Unlike *in vivo* and *in situ* biocompatibility tests, cell culture is performed as *in vitro* studies, that is, examination of cells is not performed in the complete organism. The biocompatibility tests of the gold-chitosan nanocomposite films were performed using human epithelial cells derived from cervix tissues because of their good adhesion efficiency with polymers and ability to form uniform mono-layer. Such qualities of the cells derived from human cervix tissues could help in getting higher accuracy of the cell count measurements and better reliability of the results in biocompatibility testing. For cell culture tests, living tissues are digested using enzymes to isolate individual cells from the tissues. Specimen for biocompatibity testing was prepared by drying the drops of the bionanocomposite solutions to form thin films on a glass substrate (**Figure 3.20**). To decontaminate the specimen prepared from unwanted effects of bacteria, the microscopic slide with the specimen was autoclaved before the

tests. After that, the specimen was covered with a solution medium containing the cells. It was observed that cells were proliferating on all the chitosan films. For the complete duration of the study, cells were fed at regular interval (2-3 days). *pH* of the solution was maintained at 7. When not under observation, the specimen was stored in an incubator. The incubator was set at 37 °C and the humidity was controlled to prevent the cell medium from evaporating. 5% CO_2 was also supplied to the incubator as it reacts with the bicarbonate present in the cell solution to keep the *pH* at 7.
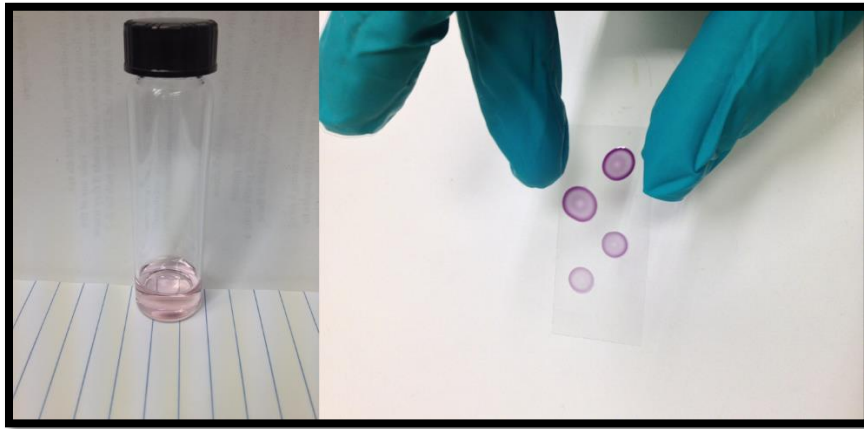
Figure 3.20 Medium containing human cervix tissue cells (left), and gold-chitosan nanocomposites specimen prepared on a glass slide for biocompatibility testing (right)

To see the cells response for their ability to adhere and proliferate on the nanocomposites materials, phase contrast optical microscopy was used. The counting was done at period of 1, 3 and 5 days interval. Readings from 5 different regions on each film were recorded at the specified time intervals.

Chapter 4. Results and Data Analysis

4.1 Gold-chitosan nanocomposites preparation

Figure 4.1 shows the gold nanoparticle – chitosan solution with varying gold concentrations and the nanocomposite films formed *via* a solution evaporation technique. The obtained films were carefully peeled off from petri dishes and stored in desiccator for later use. The thickness of the films were measured through SEM and found to be approximately 100 micrometers. Chemical, morphological, mechanical and biological characterization of nanocomposite solutions and films were performed.
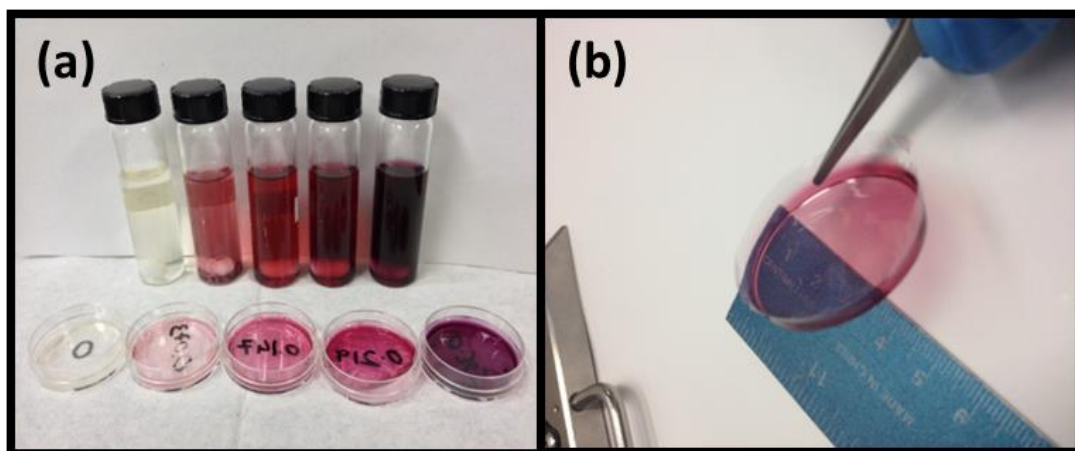
Figure 4.1 (a) Gold-chitosan nanocomposite solutions and casted films (b) free standing film of gold-chitosan nanocomposite

4.2 Materials Characterization

4.2.1 Microstructural and Morphological Characterization

4.2.1.1 UV-Vis spectroscopy analysis

Light absorbance of the samples in the UV and visible ranges were characterized using UV-Vis spectroscopy. **Figure 4.2a** shows UV-Vis spectra obtained for the bare gold nanoparticle and gold-chitosan nanocomposite in aqueous medium. In **Figure 4.2a,** the blue curve represents the UV-Vis absorption spectrum of bare gold nanoparticles aqueous solution. The absorption maxima (λ_{max}) for the bare gold nanoparticles are observed at 528 nm. The λ_{max} at 528 nm represents the characteristic of gold nanoparticles with the average diameter of about 30 ± 3 nm. In **Figure 4.2a**, the green curve shows the UV-Vis spectrum of gold-chitosan nanocomposite. In the inset on **Figure 4.2a**, it is observed that the peak from gold-chitosan nanocomposite solution has shifted from 528 nm to 532 nm. In the chitosan matrix, the gold nanoparticles tend to come closer to each other because of the ionic interaction between the functional groups present in the chitosan. Thus, there will be a shift in absorbance maxima in the curve for gold nanoparticle with chitosan.
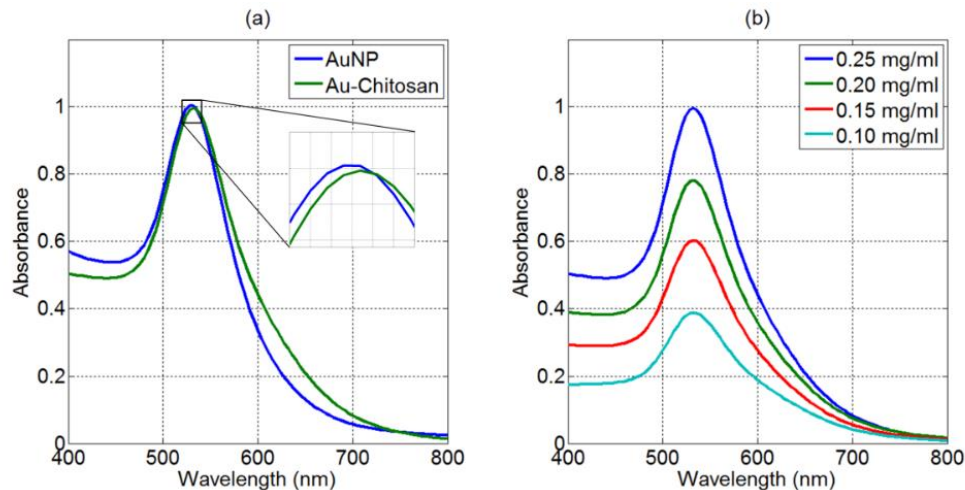
Figure 4.2 (a) UV-Vis spectra of bare gold nanoparticles and gold-chitosan nanocomposites, and (b) UV-Vis spectra (normalized) of gold-chitosan nanocomposites with varying concentration of gold

Figure 4.2b shows normalized UV-Vis spectra of the gold-chitosan nanocomposites having different gold concentrations. For studying polymer nanocomposites, it is essential to determine exact amount of nanoparticles within the polymer matrix. For that, first a standard curve showing the relationship between the absorption and gold concentration was obtained. Using the standard curve (**Figure 4.3**), quantitative determination of gold nanoparticles dispersed in the chitosan matrix was performed. This study was also useful in exploring possibilities of any agglomeration and leaching effects in the chitosan matrix.

In order to quantitatively determine the concentration of gold nanoparticles in chitosan matrix, a standard curve was obtained using the prepared gold nanoparticles suspension with known concentration. In the equation obtained with a linear fit in the standard curve (**Figure 4.3**), "y" represents the gold nanoparticle concentration in "mg/ml" while "x" is the maximum absorption recorded on the UV-Vis spectrum. Once

the standard curve with equation is obtained, it is very straight forward to determine the concentration of gold nanoparticles successfully incorporated in the chitosan matrix. Absorbance spectra obtained from 50% diluted solutions of gold chitosan nanocomposites are shown in **Figure 4.4**. **Table 4.1** shows the efficient incorporation of the gold nanoparticles in the polymer matrix. Films containing 0 mg/ml (pure chitosan), 10 mg/ml, 15 mg/ml, 20 mg/ml, and 25 mg/ml gold nanoparticles concentration are referred as Film 1, Film 2, Film 3, Film 4 and Film 5, respectively.
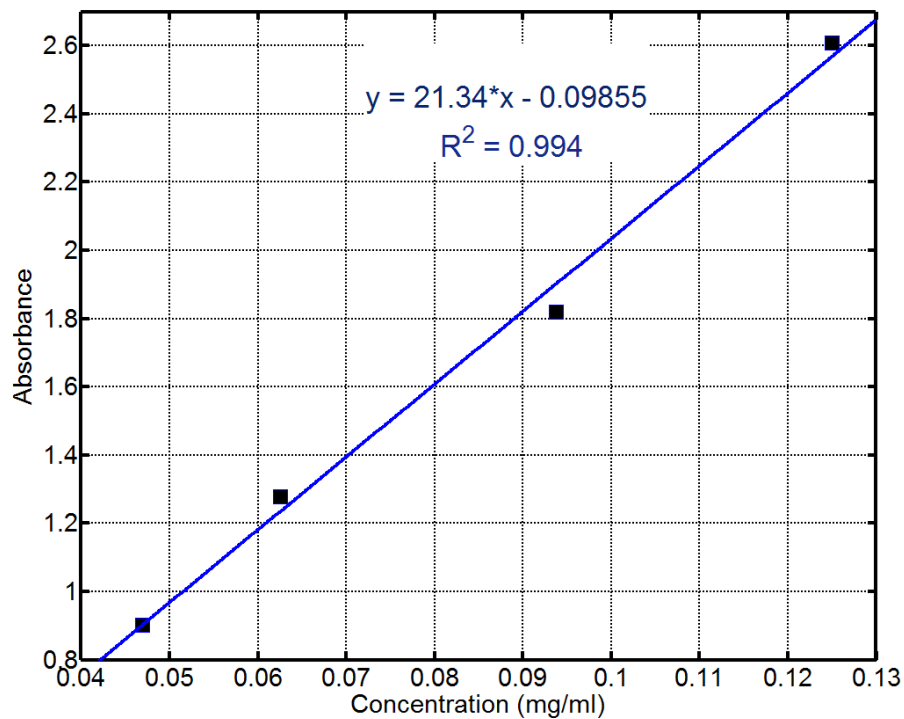
Figure 4.3. UV-Vis standard curve (Absorbance vs. Gold Concentration)
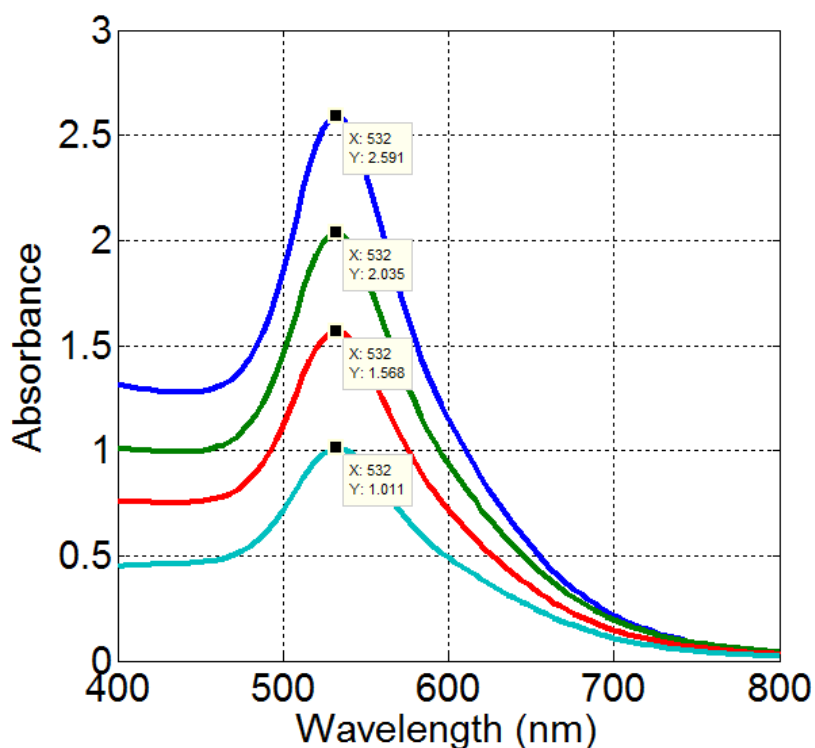
Figure 4.4. UV-Vis spectra of gold-chitosan nanocomposites with varying concentration of gold

Table 4.1 Gold concentration (w/v) calculated through standard curve technique

Absorbance Max x 2 (as the solutions were 50% diluted)	Concentration (mg/ml)
5.22	0.10
3.68	0.15
2.55	0.20
1.80	0.25

4.2.1.2 TEM, SAED and Particle size analysis

Figure 4.5a shows the TEM image of the gold nanoparticles in the polymeric mesh. Gold nanoparticles dispersed in the chitosan matrix exhibit spherical geometry. In the high resolution TEM image (**Figure 4.5b**), the interface of gold nanoparticle with chitosan matrix appears to be efficiently bonded. In other words, there is no trace of polymer aggregation visible on to the surface of the nanoparticles. This is a very

important aspect for nanocomposites in order to get maximum advantage of incorporating nano-fillers in polymer matrices. More evidence on quality of wetting and adhesion of chitosan on gold nanoparticles surfaces are shown in later sections. In TEM image (**Figure 4.5a**), particles are fairly mono-dispersed with respect to their size which is approximately 30 nm. The size distribution histogram (**Figure 4.5c**) obtained through particle size analysis tests for gold nanoparticles also revealed mean diameter of 32.4 ± 2 nm. The narrow size distribution and absence of agglomerates prove that chitosan matrix prevents agglomeration of the gold nanoparticles. Stability of gold nanoparticles in the chitosan matrix can be explained as the formation of a three dimensional net involving chitosan and gold nanoparticles since CH_2 group of chitosan also participates in the stabilization of nanoparticles (**Figure 4.6**).
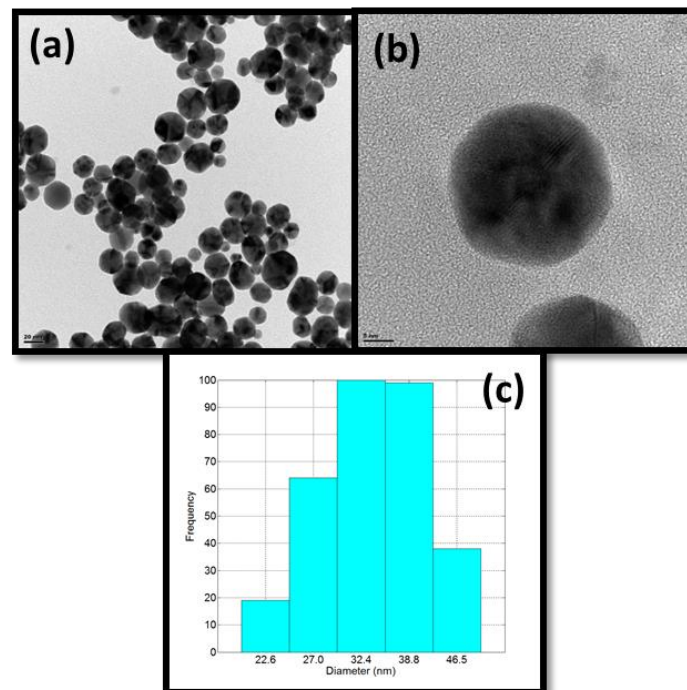
Figure 4.5 (a) TEM image of gold nanoparticles (b) close up (high magnification) image of a gold nanoparticle (c) size distribution histogram of gold nanoparticles
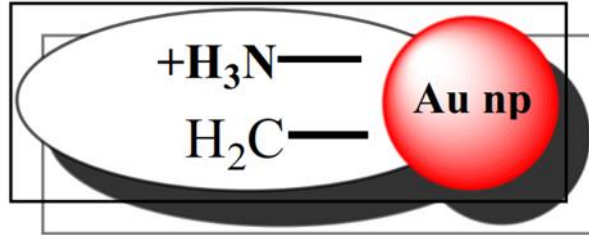
Figure 4.6 Cartoon representation of the interface bonding between gold nanoparticle and chitosan matrix

Figure 4.7 shows the SAED patters. Visible diffraction patterns as bright spots proves crystallinity of the gold nanoparticles, however, since the nanoparticles are embedded in the amorphous polymer matrix, the distinct diffraction line pattern is not clearly visible.
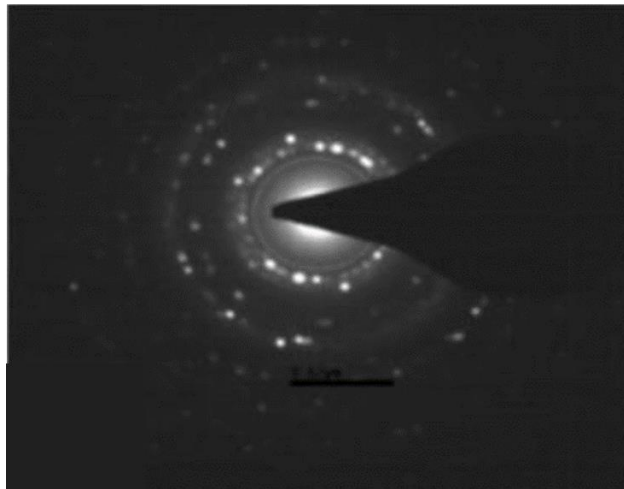
Figure 4.7 SAED image of gold nanoparticle in chitosan matrix

4.2.1.3 Scanning Electron Microscopy

Figure 4.8 shows the FE-SEM images of pure chitosan and gold-chitosan nanocomposites with different Au-NP concentration. The images clearly show increasing

concentration of Au-NPs within the chitosan-Au composites. Moreover, there are no obvious discontinuities observed at the nanoparticle-matrix interface or throughout the film cross-sections. With the use of same SEM equipment, EDX tests were performed on the specimens for the elemental analysis. Results in **Figure 4.9** show that Au in the gold-chitosan nanocomposites is in pure elemental form. No other metal impurities are present in the composites.

Film 1	Film 2	Film 3	Film 4	Film 5
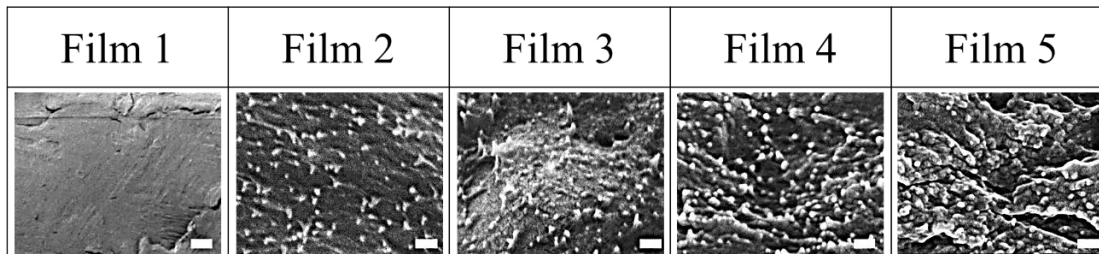
Figure 4.8 SEM micrographs of the cross sectioned pure chitosan and gold-chitosan nanocomposite films with varying gold concentrations
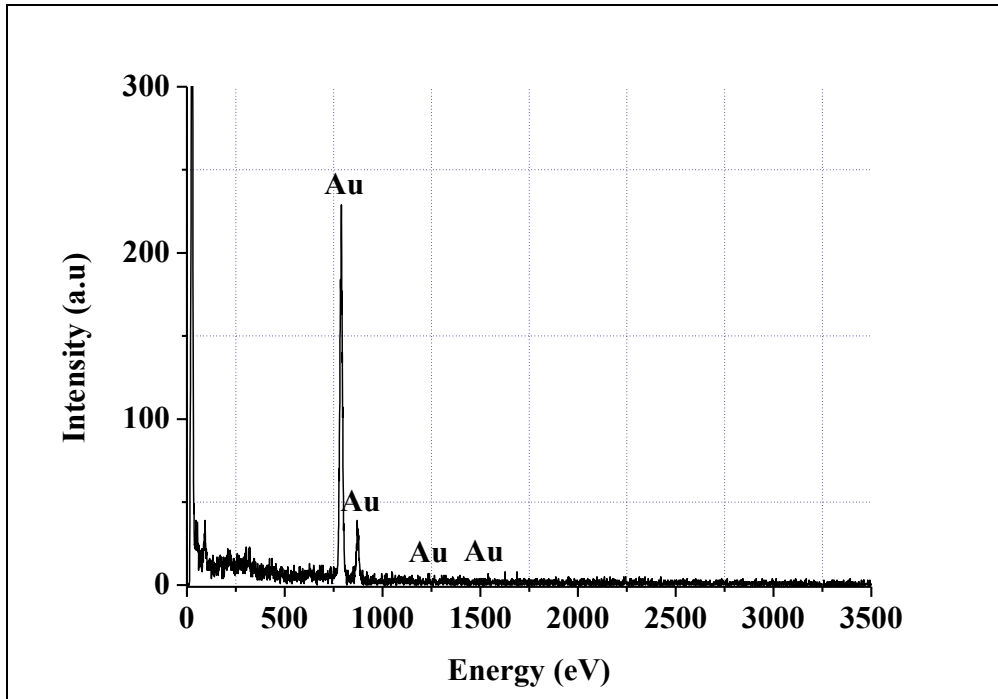
Figure 4.9 EDX spectra of gold nanoparticles in chitosan matrix

4.2.1.4 FT-IR

To analyze the nanocomposites structure and identify the molecular groups in interaction with gold nanoparticles, Fourier transform infrared (FT-IR) measurements were carried out. FT-IR spectroscopy was used to identify molecular structures that are present in the films based on their respective absorption bands in the infrared spectrum. **Figure 4.10** represents the overlaid FT-IR spectra of the nanocomposite films with varying gold nanoparticles concentration. Most of chitosan characteristic bands at 1650 cm^{-1} (amide I band characteristic to C=O stretching of N-acetyl group), 1410 cm^{-1} (bending vibration of OH group), 1376 cm^{-1} (symmetric deformation vibration mode of CH$_3$), 1323 cm^{-1} (CH$_2$ wagging vibration mode in primary alcohol) and 1259 cm^{-1} (the amide III vibration mode due to combination of N-H deformation and C-N stretching) are insensitive to the presence of metal surface (**Table 4.2**). However the most prominent band at 1553 cm^{-1} assigned to amino group in pure chitosan film shifts to a higher wavenumber (1557 cm^{-1}) in the presence of gold nanoparticles. It is quite evident that the primary amino groups are in interaction with the metal surface. The amino groups act as capping sites for the gold nanoparticles stabilization.
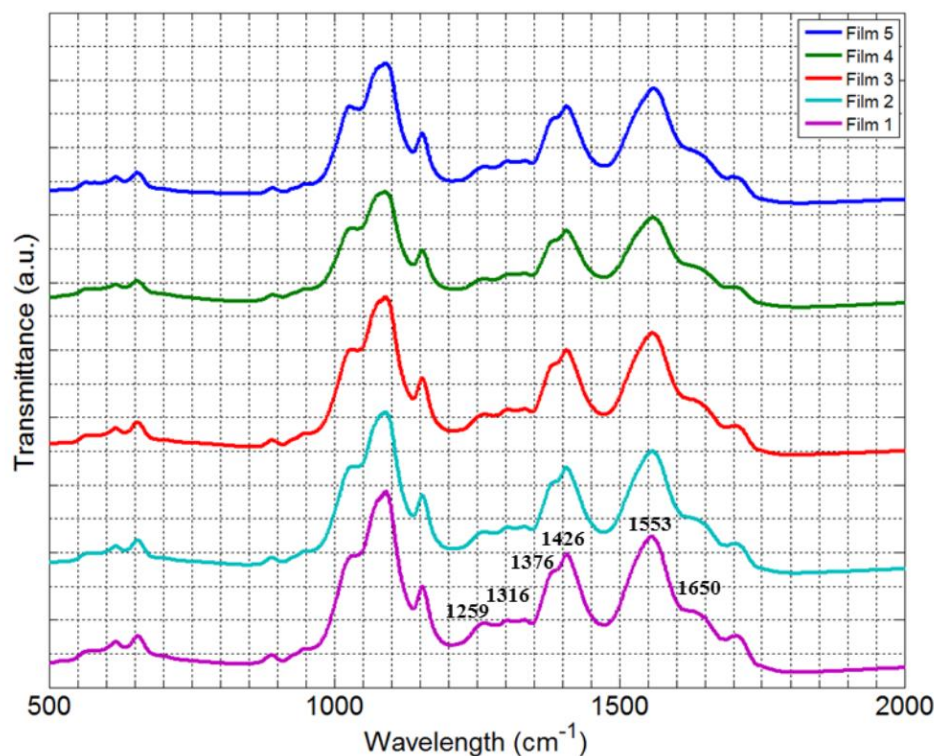
Figure 4.10 FT-IR spectra of gold-chitosan nanocomposite films at varying concentration of gold

Table 4.2 Characteristic absorption values of different functional groups present in the nanocomposites interaction with Gold nanoparticles

Functional Group	Type of Vibration	Characteristic Absorptions (cm^{-1})
Amide C=O	stretching	1650
-NH$_2$	stretching	1553
-OH	bending	1410
-CH$_3$	symmetric vibration	1376
-CH$_2$	wagging	1316
-CN and -NH	Stretching and deformation	1259

4.2.1.5 XRD

X-Ray diffraction was used to determine information regarding the crystalline structure of the nanocomposite films. The gold chitosan nanocomposites obtained with

various Au-concentrations had noticeably different XRD patterns (see **Figure 4.11**). The ratio between the intensities of the {111} and {200} reflections increased from Film 1 to Film 5 (**Table 4.3**). An increasing {1,1,1}/{2,0,0} intensity ratio indicates a more pronounced long range lattice order along preferential crystal orientations due to increasing gold nanoparticles concentration.
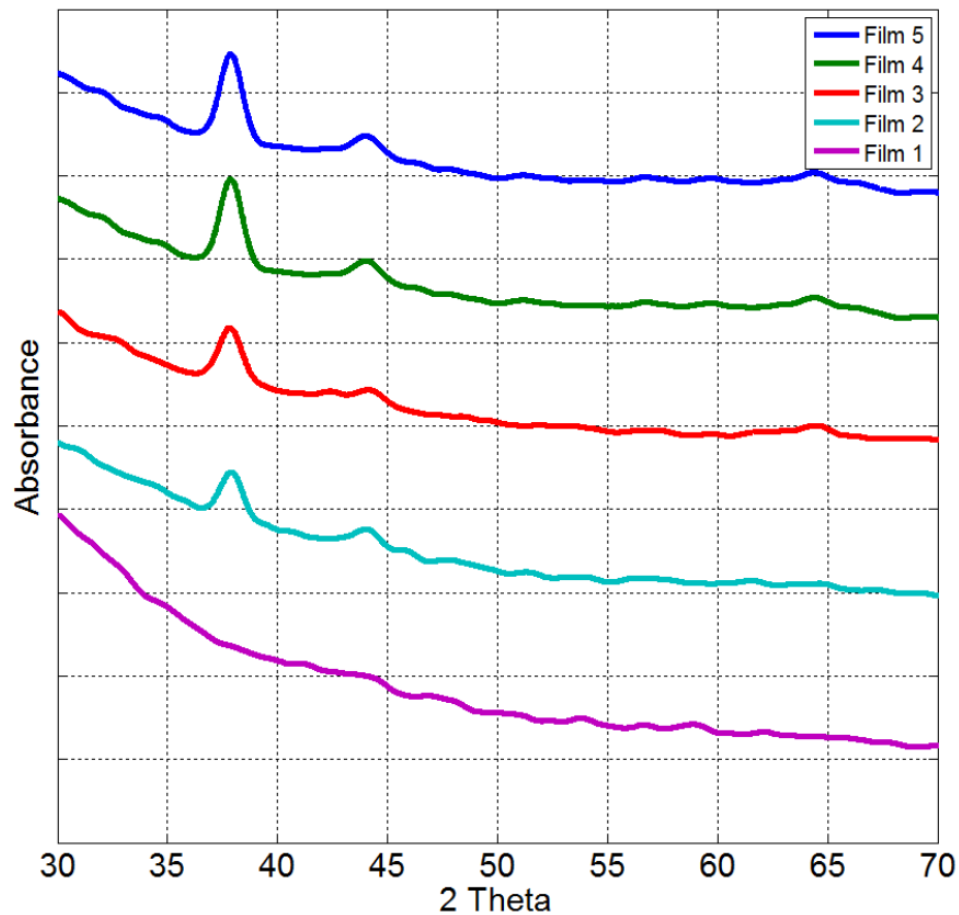
Figure 4.11 X-ray diffraction of gold-chitosan nanocomposites

Table 4.3 The ratio between the intensities of the {111} and {200} reflections of different chitosan-Au composites

Gold-chitosan nanocomposites	Film 1	Film 2	Film 3	Film 4	Film 5
Intensity ratio {111}/{200}	0.00	1.32	1.39	2.17	2.80

4.2.1.6 Zeta-Potential analysis

Stability of nanoparticles in composite solution is essential in the process of making nanocomposites. Stability of colloidal dispersions of aqueous solutions can be studied by checking its zeta potential. For charged particles with optimum zeta potential (" > 30 mV), particle aggregation is usually less likely to occur as a result of electrostatic repulsions. **Figure 4.12** and **4.13** show the zeta potential of bare gold nanoparticles and chitosan matrix respectively. Because of the opposite nature of charges of both constituents of the composite, it is very likely that they will be attracted as a result of electrostatic interactions. In **Table 4.4,** the zeta potential values of nanocomposite films synthesized using varying concentrations of gold nanoparticles with chitosan are shown. The zeta potential measurements revealed that increasing the concentration of gold nanoparticles in the composite do not contribute much effect. The sufficient positive charge (> +60 mV) due to coating/ wrapping of the gold nanoparticles with the cationic chitosan is rendered making them electrostatically stable.
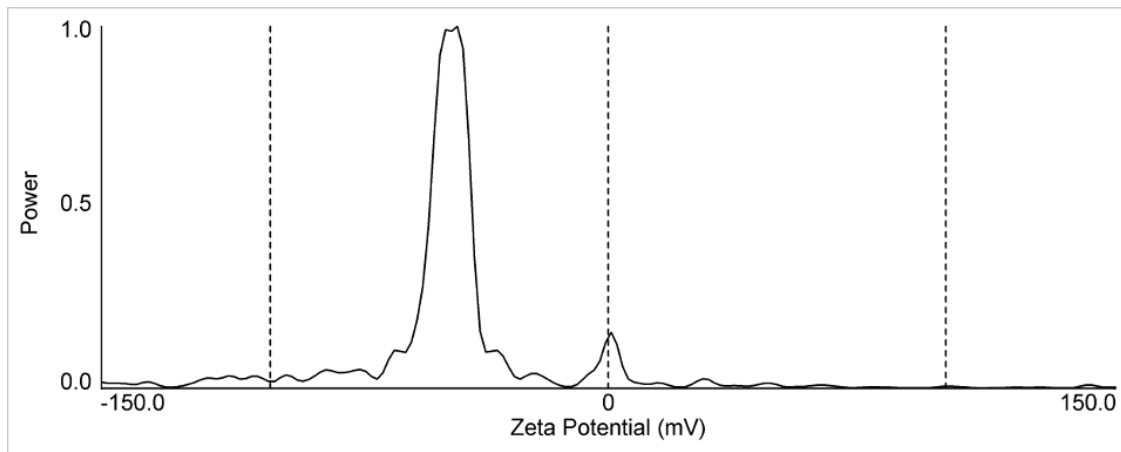
Figure 4.12 Zeta potential curve of bare gold nanoparticles
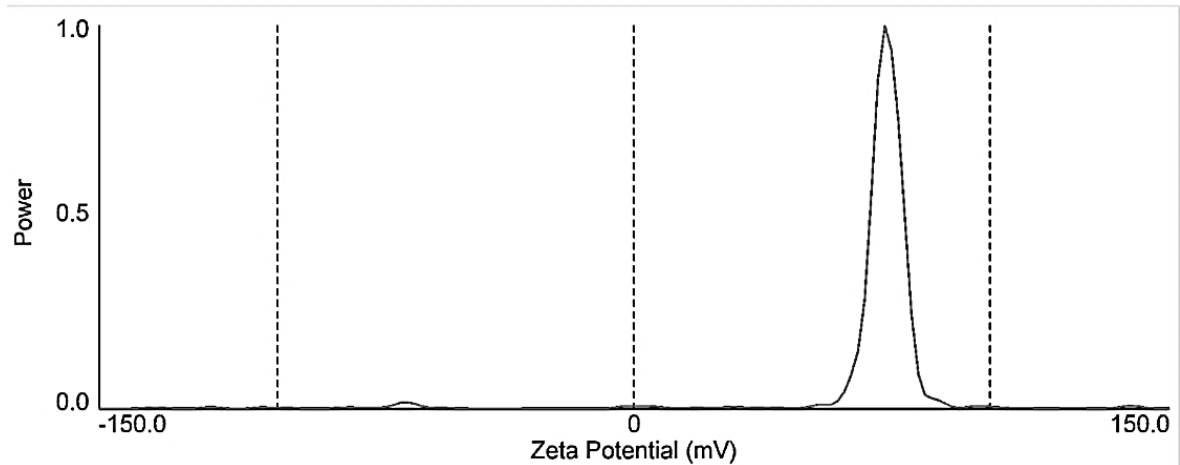
Figure 4.13 Zeta potential curve of chitosan solution

Table 4.4 Zeta potential values of the gold-chitosan nanocomposites

Au Concentration in Chitosan	0.10 mg/ml	0.15 mg/ml	0.20 mg/ml	0.25 mg/ml
Mean Zeta Potential (mV)	66.87	70.09	62.74	62.99
S.D.	1.3	0.32	0.38	1.01

4.2.2 Mechanical characterization

Following is the summary about the previous studies on mechanical properties of chitosan based composites for biomedical applications. Jayasuriya et al. [85] observed positive effects on nano- and micro-hardness as the ratio of ZnO nanoparticles is increased in Chitosan matrix. Garcia et al. [86] obtained more elastic and less hard zein-chitosan composite films as zein concentration was increased in the material. In a study of structural and mechanical properties of halloysite-chitosan bionanocomposites for tissue engineering, Liu et al. [87] achieved improvements in tensile and viscoelastic properties as halloysite concentration is increased. From a study on chitosan-

nanohydroxyapatite (nHA) nanocomposites for bone tissue engineering, Maganti et al. [60] reported positive effect of nHA concentration on mechanical properties without affecting other essential properties exhibited by the pure chitosan films. Graphene oxide-chitosan nanocomposites developed for bio- and electro-chemical applications showed significant increase in tensile strength and young's modulus upon introducing minute amount of graphane oxide reinforcement [13]. In a study on graphane reinforced chitosan nanocomposites for tissue engineering, reduced modulus and hardness increased considerably with a small amount of graphene addition [18]. Positive effects of gold nanoparticle reinforcement on both mechanical stability and cellular response was observed when gold nanoparticle reinforced chitosan nanocomposites was studies as a material used for peripheral nerve regeneration [19]. Wang et al. achieved significant improvement in indentation hardness, tensile modulus and tensile strength of chitosan film upon reinforcement with carbon nanotubes [17]. However, approach towards in-depth understanding of the nano-scale mechanical properties lacks attention of the researchers. Following sections describe quantitative analysis performed for nanomechanical properties of the gold-chitosan nanocomposites films in this work.

4.2.2.1 Quasi-static nanoindentation

Quasi-static nanoindentation tests were performed to determine reduced modulus of the gold-chitosan bionanocomposite films. **Figure 4.14** shows representative load vs. displacement curves obtained from Film 1, Film 2, and Film 3. It is clearly observed that for the same constant load of 7500 µN, indentation depth reached at the end of the loading segment is considerably lower as the gold concentration is increased in the

chitosan matrix. In other words, hardness increases as more gold nanoparticles are added

in the chitosan matrix.
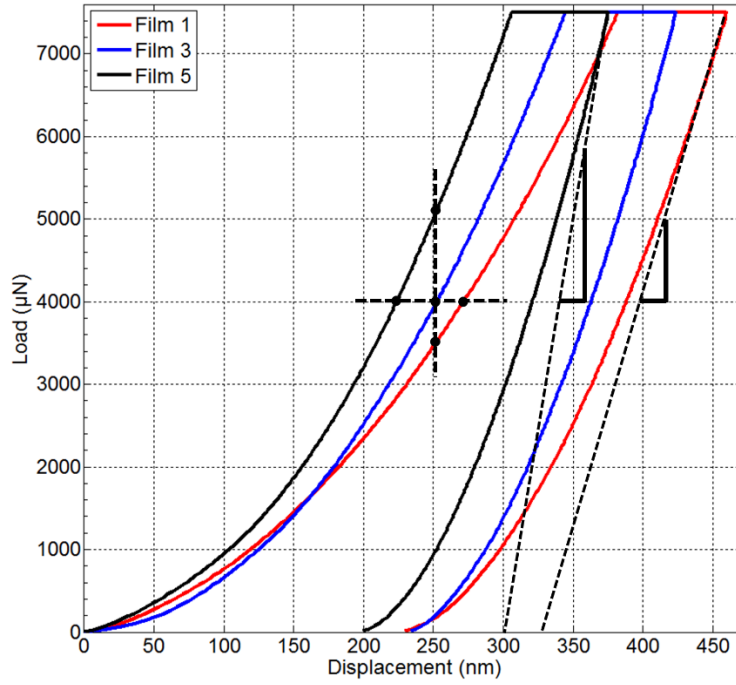
Figure 4.14 Representative load-displacement curves of gold-chitosan nanocomposite films (Film 1, Film 3 and Film 5)

When material is loaded under constant force, it exhibits continuous deformation

as a result of creep effects. Creep effect is observed in the load-displacement curves as a

flat region on top and in between loading and unloading curves. In the Figure, it is hard to

evaluate the intensity of creep effects, however, the difference between the maximum

depths of penetration in the creep segment is lower in case of Film 5 than it is in Film 1.

The results indicate material creeping is lower with higher concentration of gold

nanoparticles in the chitosan matrix. In-depth creep analysis will be discussed in later

sections of this chapter. Reduced modulus is calculated from the slope of the unloading

curve. In **Figure 4.14**, slope at the beginning of unloading curves is stiffness of the

material. It is evident that the stiffness increases as more gold nanoparticles are added to the chitosan matrix. Reduced modulus is calculated from stiffness and indenter contact area using **Equation 3.8** in Chapter 3, and is directly proportional to stiffness of the material. In this work, for the same nanocomposite film, since there was no significant difference observed in the stiffness values from the unloading curves of quasi-static and dynamic nanoindentation experiments, results obtained from unloading curves of the dynamic experiments are presented in this chapter. **Figure 4.15** shows the bar plots of reduced modulus of the gold-chitosan nanocompsite films. In **Figure 4.15a** the effect of the reinforcement of chitosan with gold nanoparticles is very clear. As the gold nanoparticle content is increased, significant improvement in reduced modulus is achieved. For Film 1 (pure chitosan), the average reduced modulus for at least 8 indents is ~ 3 GPa. The same for Film 5 is ~ 5.5 GPa. In other words, ~ 83% improvement in reduced modulus of chitosan film is achieved by incorporating gold nanoparticles with 0.25 mg/ml concentration. All other concentrations in between Film 1 and Film 5 show the expected trend i.e. with increasing gold nanoparticle concentration, the reduced modulus is higher.
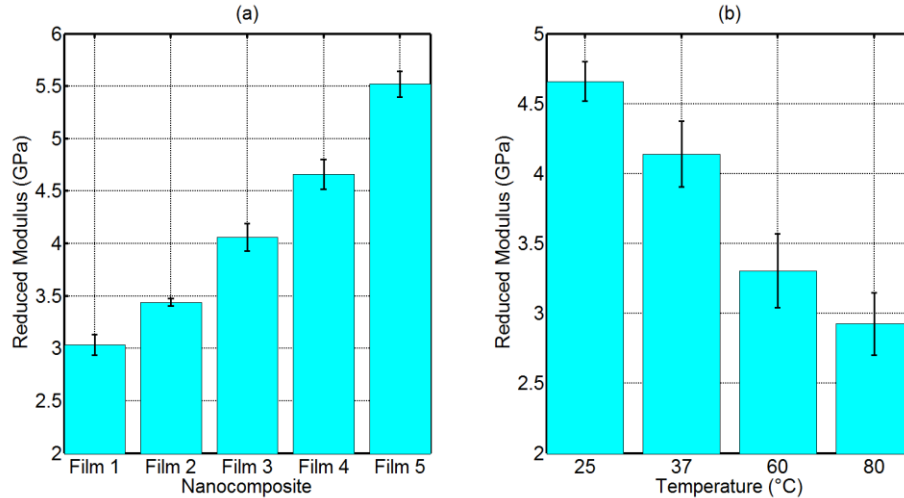
Figure 4.15 Bar plots of reduced moduli (a) effect of concentration, and (b) effect of temperature

Temperature also has great influence on mechanical properties of polymers. Generally, bonding strength of the polymeric chain becomes weaker and the material becomes more flexible under the influence of higher temperatures. As a representation, **Figure 4.15b** shows the reduced modulus values of Film 4 at temperatures of 25 °C, 37 °C, 60 °C and 80 °C. It is clear from the bar plot that the chitosan film loses its stiffness (and hence reduced modulus) with increase in temperature. It is interesting to know that even when we go from room temperature (25 °C) to the human body temperature (37 °C), there is a significant drop in reduced modulus of the gold-chitosan nanocomposites. In designing the material in tissue engineering and other application where it is in direct contact with the human body, such studies are really useful. Reduced modulus values get even lower at higher temperatures.

Figure 4.16 is a three dimensional representation of reduced modulus of the gold chitosan as a function of gold concentration and as a function of temperature. It is clear

78

that for the material having higher stiffness, more gold concentration is required. All films show similar trend of reduced modulus with increase in temperature i.e. as the temperature is higher, reduced modulus gets lower. In the 3D plot, for Film 3 and Film 5, at 37 °C there is a sudden drop in reduced modulus. This could be the result of significant relaxation of residual stresses in the film with increase in temperature above its processing (film curing) temperature. However, in the films other than Film 3 and Film 5, this effect is not observed.
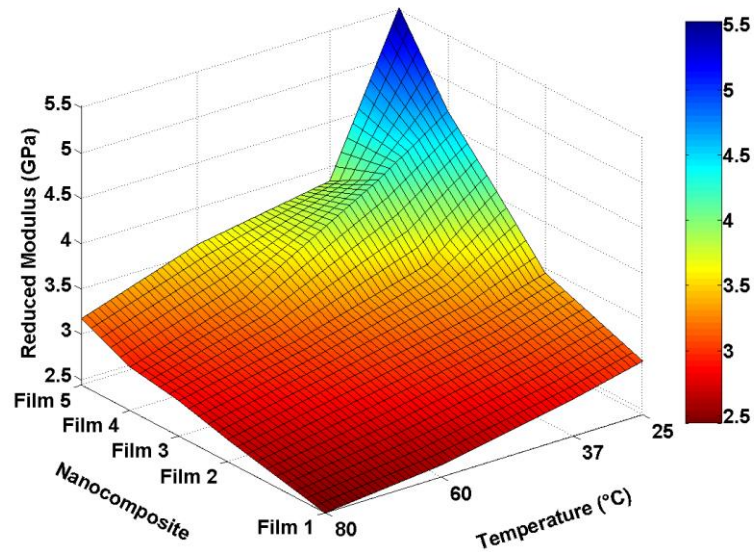
Figure 4.16 Three dimensional surface representation of reduced modulus vs. gold concentration vs. temperature

4.2.2.2 Dynamic nanoindentation

Dynamic nanoindentation was performed by indenting the gold chitosan nanocomposite films up-to a certain depth and oscillating the indenter tip with a range of frequencies (10 Hz to 200 Hz). The response of the nanocomposite films was used to characterize viscoelastic properties of the materials. Viscoelastic properties such as

storage modulus, loss modulus, and loss tangent (tan delta) were determined and analyzed for the entire frequency sweep. This section describes the viscoelastic properties results of the films.

Figures 4.17 to 4.21 show 3D surface plots of storage moduli of the gold chitosan nanocomposite films. They show the storage modulus as a function of temperature and as a function of frequency. In all cases, it is observed that the storage modulus is lower at higher temperatures, and as the temperature is increased, the materials lose their energy storing capacities. For instance, the storage modulus of film 3 at 10 Hz drops from 9 GPa to below 6.5 GPa as the temperature is increased from 25 °C to 80 °C. Also, as the gold nanoparticle concentration is increased, the storage modulus is also increased. For example, at 25 °C and a frequency of 10 Hz, the storage moduli for Films 1, 2, 3, 4, and 5 are approximately 6.5 GPa, 7.5 GPa, 9 GPa, 10.3 GPa and 12.1 GPa, respectively. In viscoelastic materials, the force required to deform the material is proportional to the rate of deformation. In other words, viscoelastic materials behave like the ones with higher stiffness (more solid like) if they are deformed at higher loading rates. Because of that, it is evident from Figures 4.17 to 4.21 that at higher frequencies, the storage modulus is increased as the deformation rate is increased. For example, in case of Film 3, at 25 °C, the storage modulus is 9 GPa at 10 Hz frequency. At the same temperature, when the loading frequency is increased to 200 Hz, the reduced modulus is recorded to be ~ 10 GPa.
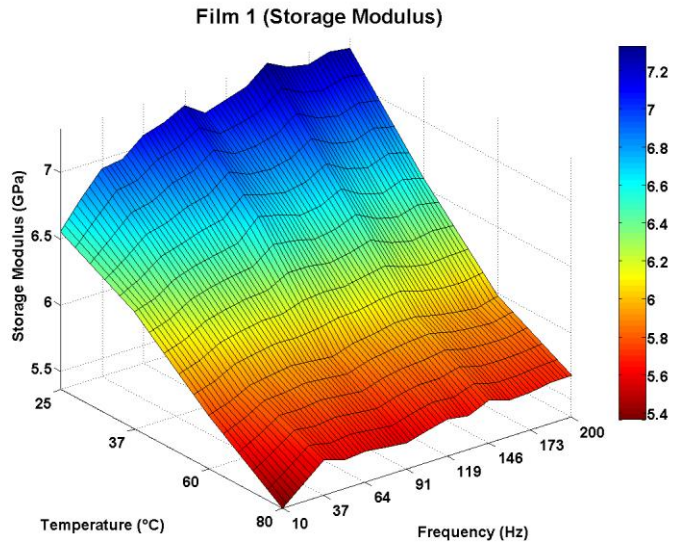
Figure 4.17 Storage modulus vs. temperature vs. frequency of Film 1
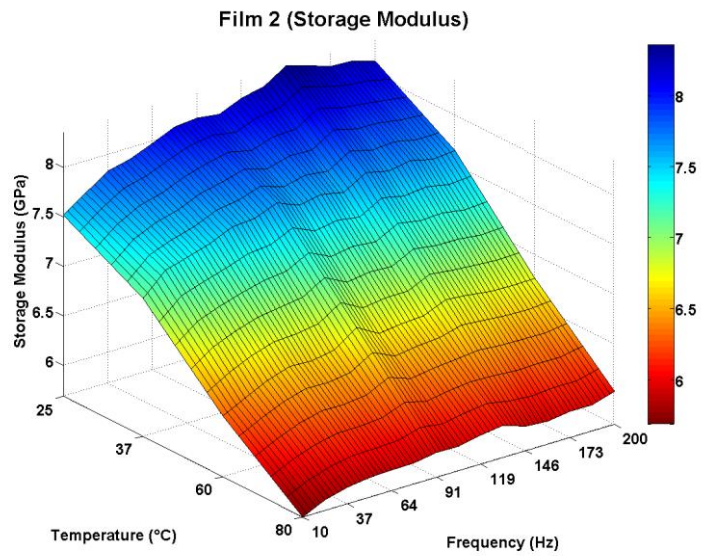
Figure 4.18 Storage modulus vs. temperature vs. frequency of Film 2
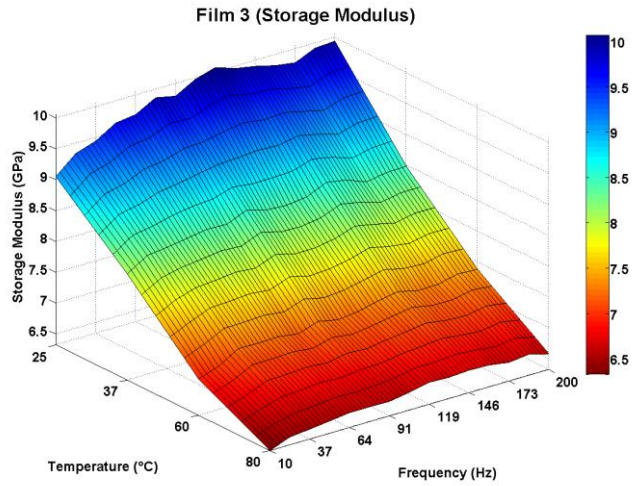
Figure 4.19 Storage modulus vs. temperature vs. frequency of Film 3
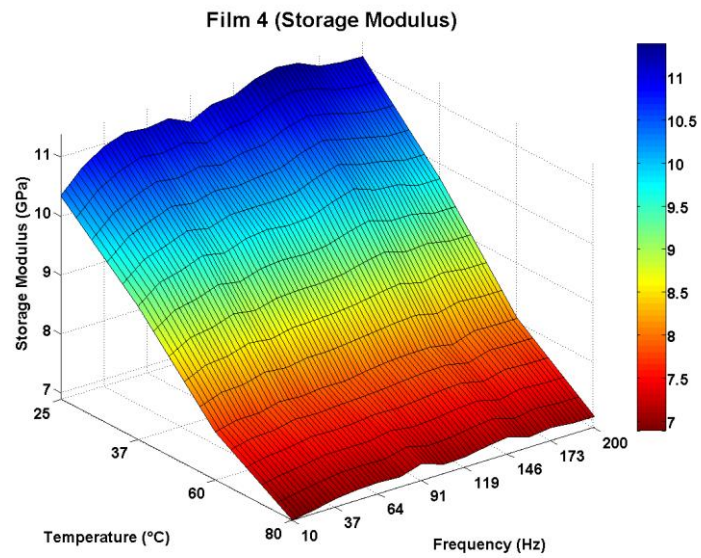
Figure 4.20 Storage modulus vs. temperature vs. frequency of Film 4
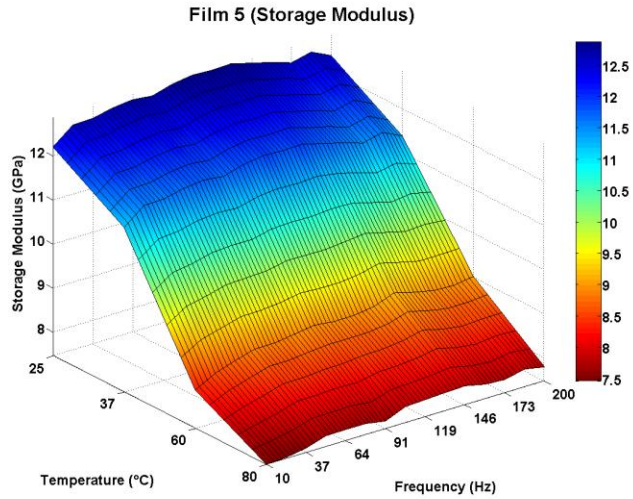
Figure 4.21 Storage modulus vs. temperature vs. frequency of Film 5
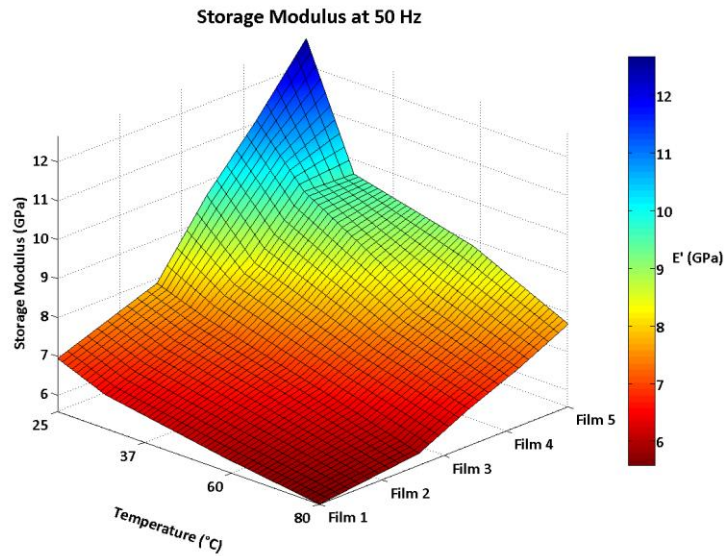
Figure 4.22 Three dimensional surface representation of storage modulus (at 50 Hz) vs. gold concentration vs. temperature

To summarize the effect of gold concentration and temperature on storage modulus of the nanocomposite films, a frequency of 50 Hz was chosen and the storage modulus was plotted vs. temperature and vs. nanocomposite type (**Figure 4.22**). The

surface plot is similar to the surface plot of reduced modulus vs. temperature vs. gold concentration (**Figure 4.16**). The highest storage modulus is observed with the highest gold concentration film (Film 5) at the lowest temperature (bluish region). The lowest reduced modulus is seen at the red region which is the least gold concentration film (pure chitosan, Film 1) at highest temperature. Like reduced modulus, the sudden drop in storage modulus at 37 °C is observed in the case of Film 5.

The trend of loss modulus vs. temperature is also similar to storage modulus i.e. the loss modulus of the films drops down as the temperature is increased and rises as the gold concentration is increased (**Figures 4.23** to **4.27**). Similar trend is observed for the loss tangent (tan delta) values (**Figures 4.28** to **4.32**).
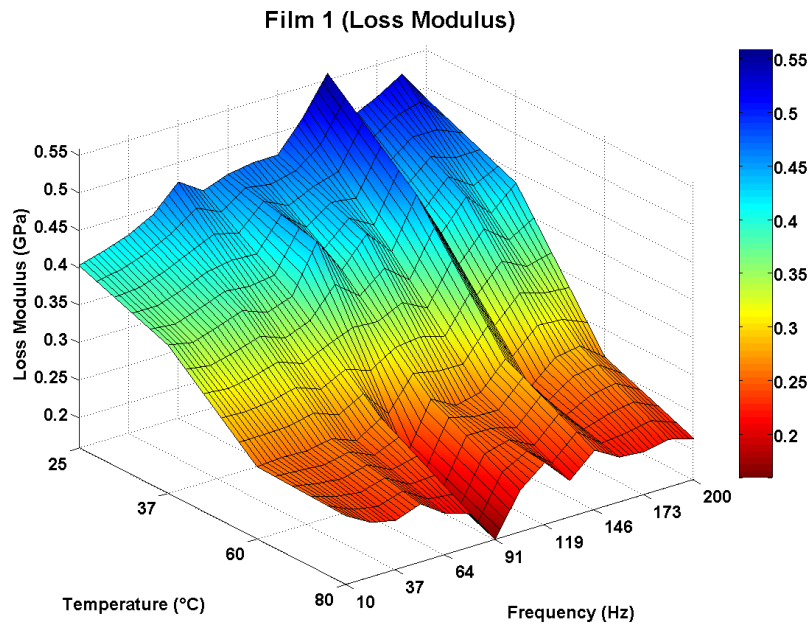
Figure 4.23 Loss modulus vs. temperature vs. frequency of Film 1
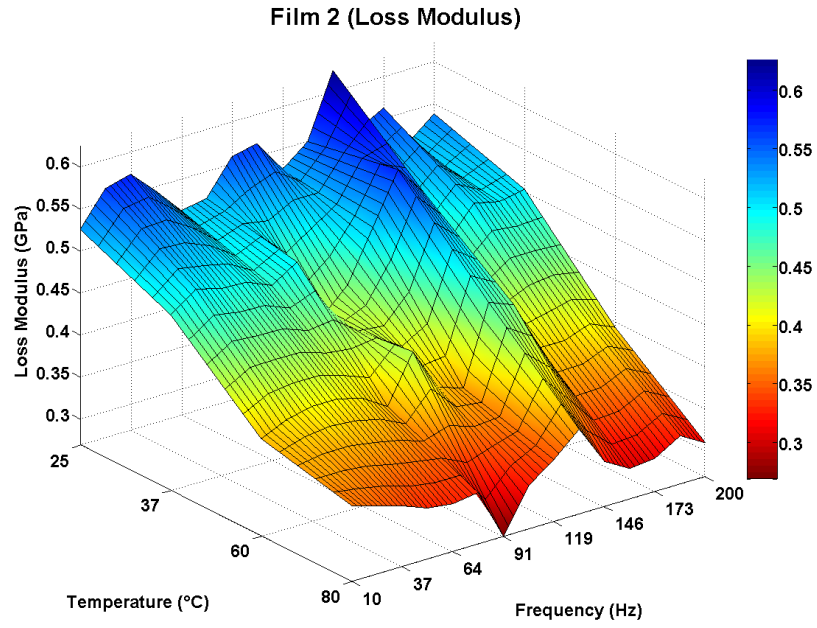
Figure 4.24 Loss modulus vs. temperature vs. frequency of Film 2
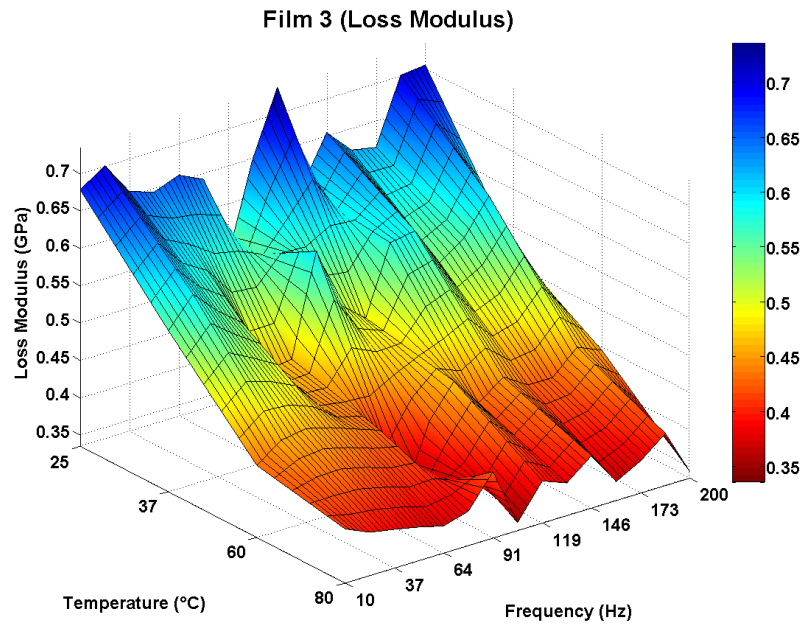
Figure 4.25 Loss modulus vs. temperature vs. frequency of Film 3
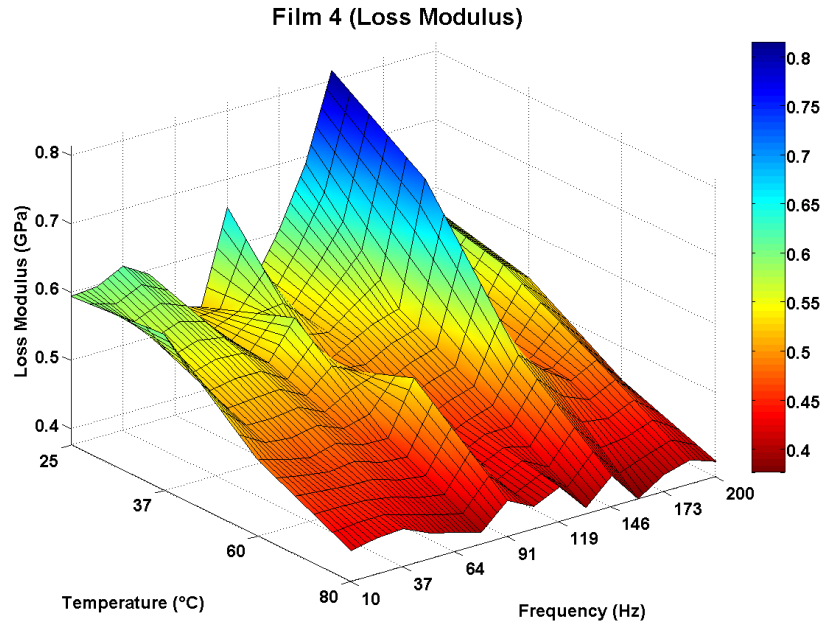
Figure 4.26 Loss modulus vs. temperature vs. frequency of Film 4
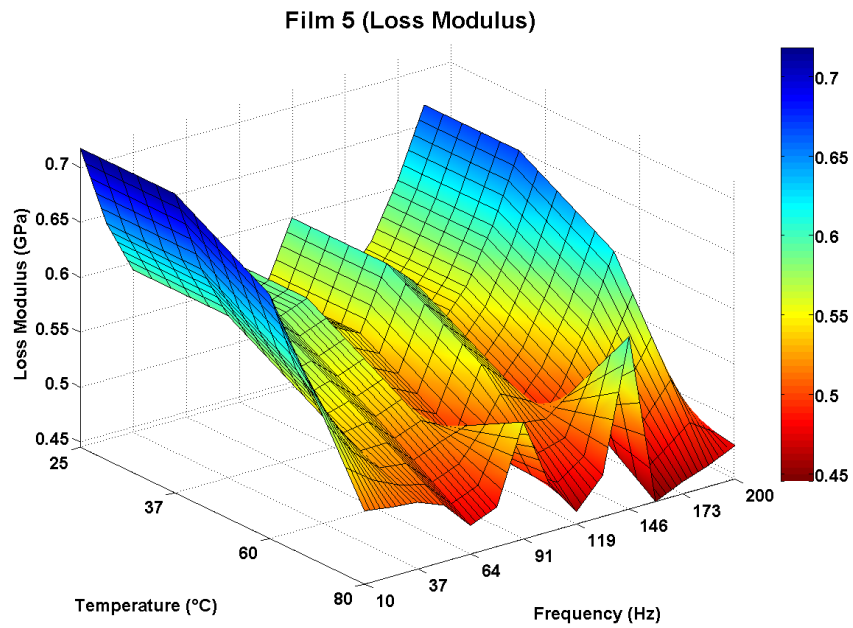
Figure 4.27 Loss modulus vs. temperature vs. frequency of Film 5
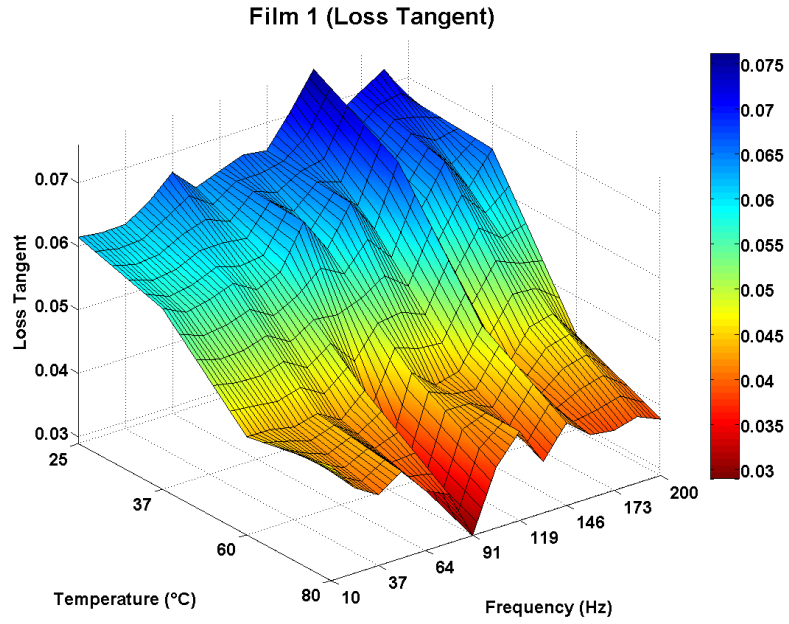
Figure 4.28 Loss tangent vs. temperature vs. frequency of Film 1
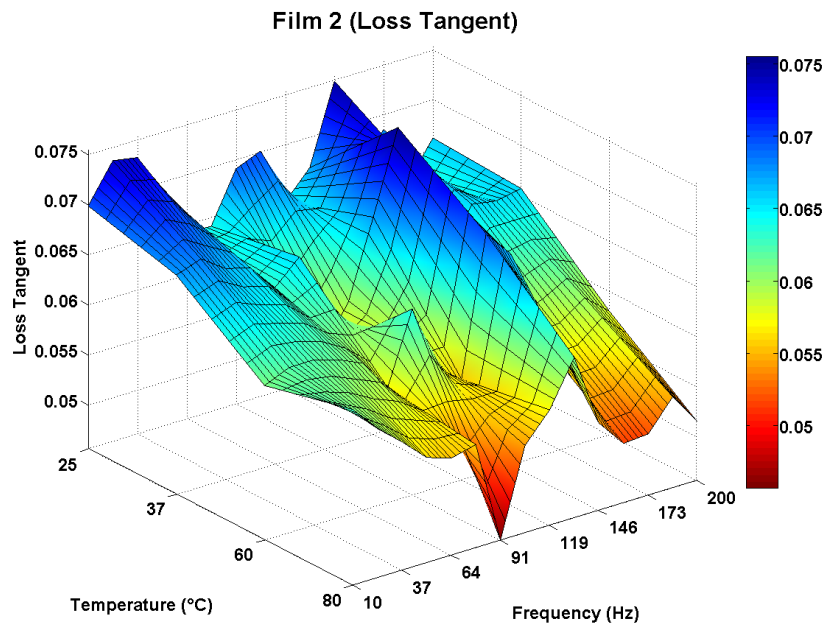
Figure 4.29 Loss tengent vs. temperature vs. frequency of Film 2
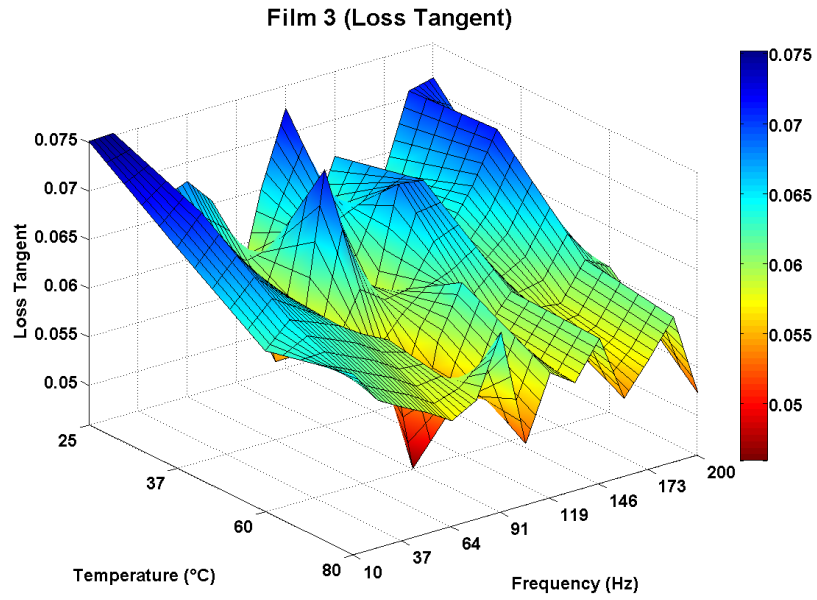
Figure 4.30 Loss tangent vs. temperature vs. frequency of Film 3
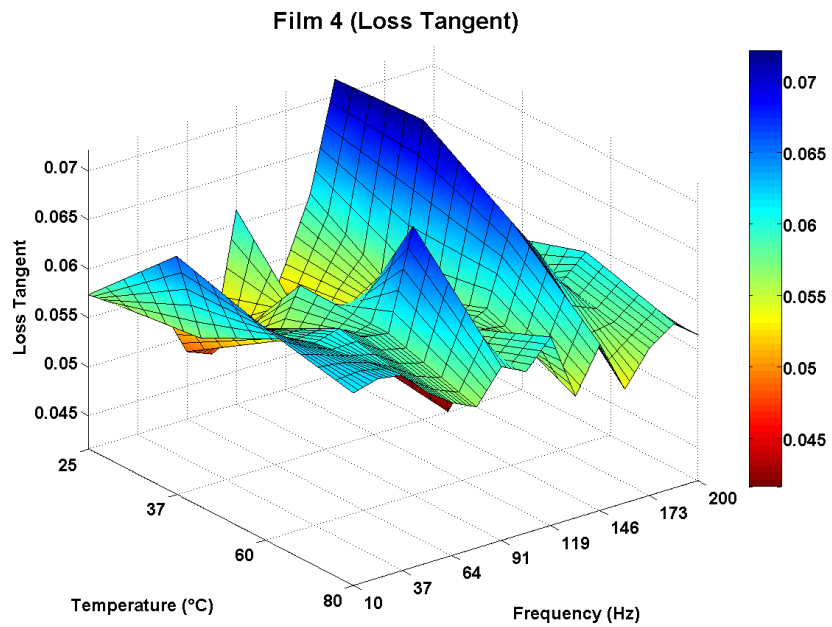
Figure 4.31 Loss tangent vs. temperature vs. frequency of Film 4
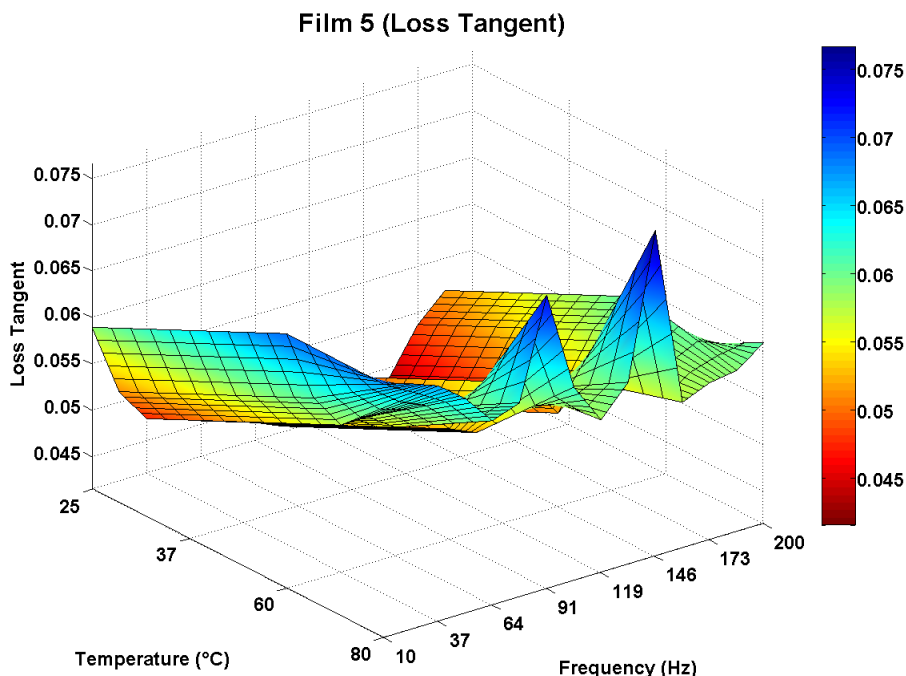
Figure 4.32 Loss tangent vs. temperature vs. frequency of Film 5

Figure 4.33 summarizes the results of frequency sweep experiments to show the effect of gold concentration in the chitosan matrix on viscoelastic properties. It shows that the storage modulus increases with increase in gold concentration and loss modulus shows similar trend with increase in gold concentration. However, the loss factor tan delta (loss tangent) is higher as the chitosan is used in more pure form. That means, the materials is exhibits less solid-like nature when it is used with least gold concentration. Yi-Lo et al. [19] reported storage modulus values for gold-chitosan nanocomposites with increasing gold concentration in the range of 2.8 GPa to 3.5 GPa by performing dynamic mechanical analysis at 37 °C. Marino et al. [14] also performed dynamic mechanical analysis on chitosan and chitosan based nanocomposites, and determined storage moduli in the range of 4 to 9 GPa. Shear modulus of chitosan with different concentration of -
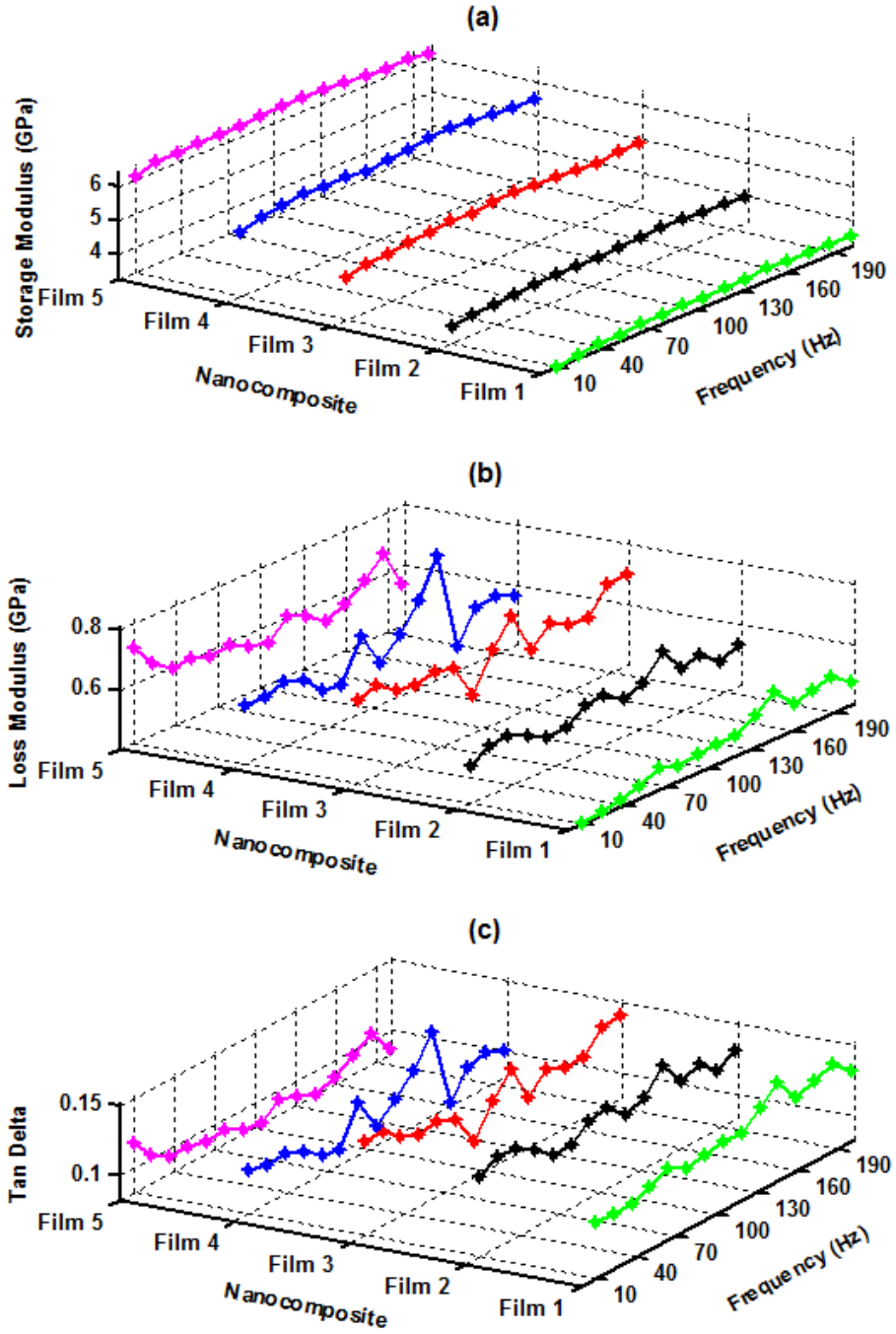
Figure 4.33 Three dimensional plots of (a) storage modulus, (b) loss modulus, and (c) loss tangent vs. gold concentration vs. frequency

tripolyphosphate complexes was determined to be around 1 GPa in a study by Ji et al. [88]. In a study of mechanical properties of Chitosan/halloysite nanotubes bionanocomposites [87], the storage modulus of chitosan film was determined around 1.8 GPa at 60 °C.

4.2.2.3 Nanoindentation creep analysis

Figure 4.34 shows nanoindentation creep curves for Film 1, Film 3 and Film 5. In the figure, indentation depth is plotted vs. holding time, when the material is deformed under the influence of constant load (here 11 mN) over a period of time. As is seen in the figure, as soon as the ramp loading is applied to the material, it initially deforms at faster rate and as time increases, the deformation rate slows down. Such creep effect can be quantitatively evaluated to characterize important time dependent viscoelastic properties.
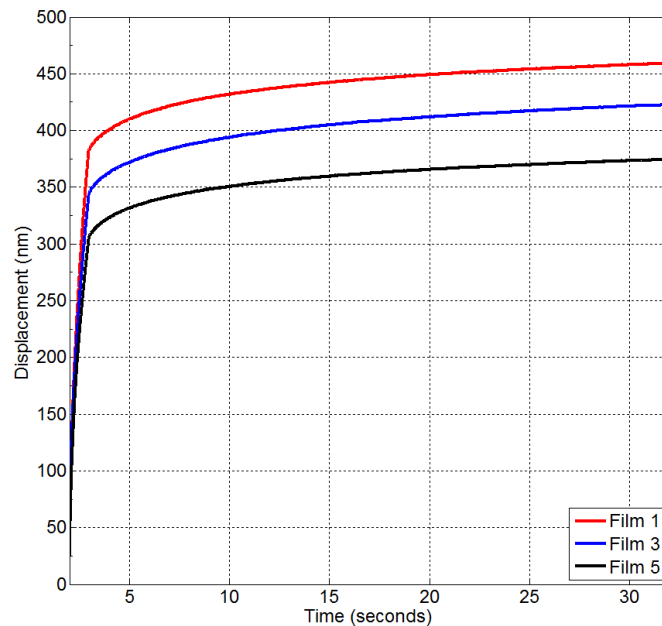
Figure 4.34 Representative curves of creep effects in gold-chitosan nanocomposites (Film 1, Film 3 and Film 5)

By fitting experimental indentation depth over a period of time (t) with the expression of **Equation 3.18** in Chapter 3, stiffness and damping coefficients parameters in **Figure 3.17** are obtained. **Figure 4.35** shows curve fitting of creep segment in **Figure 4.34** with the use of **Equation 3.18**. Through curve fitting, the constants such as J_0, J_1, τ_1, J_2, and τ_2 are obtained. The obtained constants are summarized in **Table 4.5**.
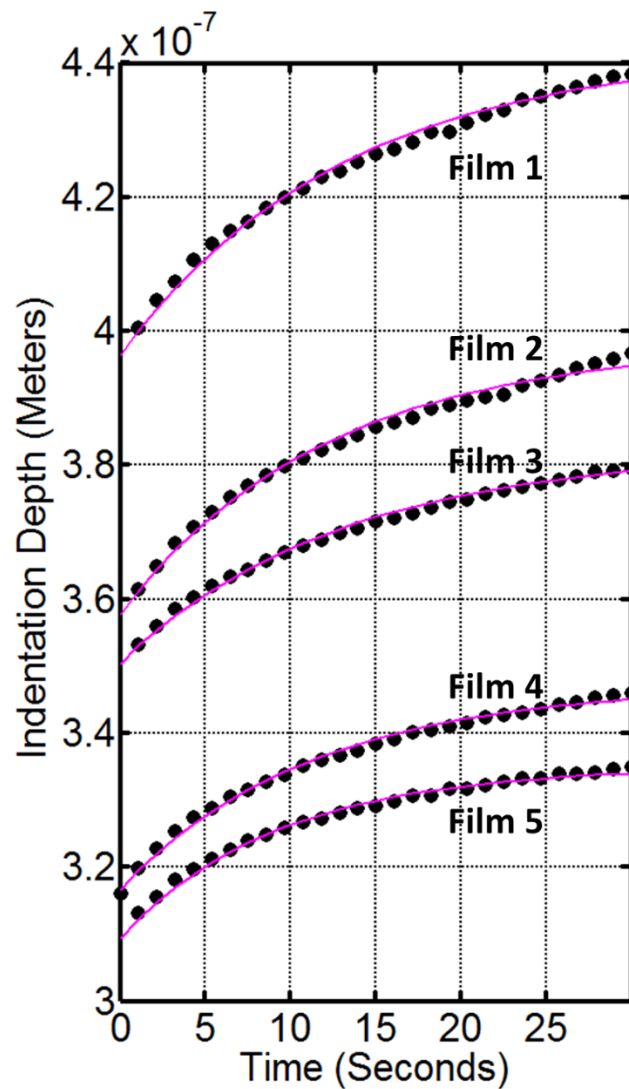
Figure 4.35 Fittings of experimental creep data (dots) with the creep function's expression (line) in Equation 3.18

Table 4.5 Shear moduli, creep compliance and retardation time constants obtained from curve fitting

		G (Pa)	C_0 (m/N)	C_1 (m/N)	τ_1 (sec)	C_2 (m/N)	τ_2 (sec)
Film 1	Average	8.64E+08	7.12E-10	2.33E-11	0.240674	1.1E-10	12.60622
	± SD	10213262	8.23E-12	3.86E-11	0.007448	3.76E-11	0.396344
Film 2	Average	1.04E+09	5.99E-10	2.8E-11	0.277132	9.23E-11	11.76729
	± SD	18630719	8.53E-12	3.52E-11	0.012532	3.4E-11	0.513012
Film 3	Average	1.08E+09	5.51E-10	9.7E-12	0.298432	7.59E-11	11.79891
	± SD	17192684	1.05E-11	2.29E-12	0.045026	1.93E-12	0.754708
Film 4	Average	1.24E+09	4.88E-10	2.78E-11	2.982356	6.5E-11	11.23709
	± SD	20673351	5.86E-12	3.25E-11	4.736979	2.51E-11	0.279298
Film 5	Average	1.3E+09	4.57E-10	7.65E-12	0.28252	6.43E-11	10.70223
	± SD	29226570	8.59E-12	2.45E-12	0.073279	3.61E-12	0.90058

Using **Equation 4.1** [80], shear modulus 'G' of the materials can also be determined.

$$G = \frac{1}{2(C0 - \sum Ci)} \quad \dots\dots\dots\dots\dots\dots\dots\dots\dots\dots\dots\dots\dots\dots 4.1$$

In **Table 4.5**, the shear modulus values are increasing as the gold concentration is increased in the chitosan matrix.

4.2.2.4 Nanoindentation stress relaxation analysis

Figure 4.36 shows relaxation behaviour of the gold chitoan nanocomposite films. The plots show load vs. indentation time as a results of deformation of the specimen at constant depth (here, 300 nanometers). As it is seen in the figure, after the loading ramp to the maximum load required to panetrate 300 namometers, the load seem to lower at higher rate in the initial part (up to 10 seconds). After that, the rate of load drop is lower

as time increases. It can also be observed that for reaching and maintaining the same indentation depth, Film 5 needs higher load (i.e. offers greater resistance) compared to Film 3 and Film 1.
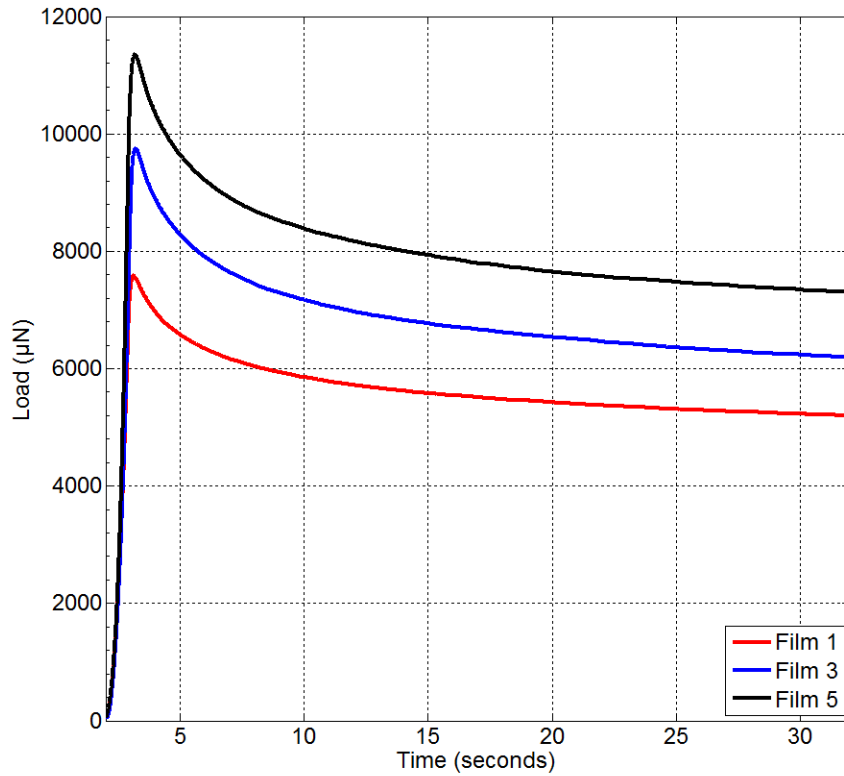
Figure 4. 36 Representative curves of relaxation effects in gold-chitosan nanocomposites (Film 1, Film 3 and Film 5)

In creep tests, load is kept constant and indentation depth increases while in relaxation tests, depth is kept constant and the required load to keep the depth constant lowers. Studying relaxation behaviour also proves useful in understanding time dependent properties of viscoelastic materials.

For relaxation analysis, the generalized maxwell model was used. **Equation 3.21** was used to fit relaxation modulus data to determine relaxation constants of the mateials.

Figure 4.37 shows the fits of relaxation modulus vs. time and the obtained relaxation

modulus constants are summerized in **Table 4.6**.
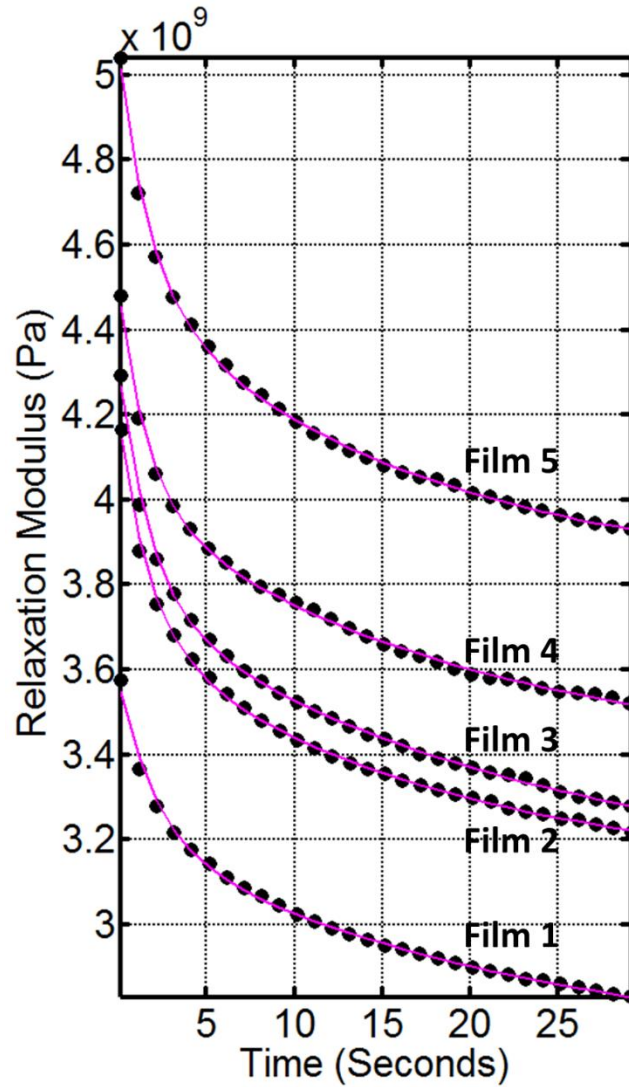
Figure 4.37 Fittings of experimental (dots) relaxation effects with the relaxation modulis' expression (line) in Equation 3.21

Table 4.6 Relaxation moduli and retardation time constants obtained through curve fitting

		E_0 (Pa)	E_∞ (Pa)	E_1 (Pa)	τ_1 (s)	E_2 (Pa)	τ_2 (s)
Film 1	Average	3.59E+09	2.76E+09	2.92E+08	1.46E+00	5.32E+08	1.77E+01
	SD	5.79E+07	5.36E+07	1.75E+07	1.25E-01	1.23E+07	1.58E+00
Film 2	Average	4.23E+09	3.18E+09	4.11E+08	1.32E+00	6.42E+08	1.55E+01
	SD	7.66E+07	9.05E+07	3.26E+07	2.80E-01	2.10E+07	3.98E+00
Film 3	Average	4.31E+09	3.24E+09	4.15E+08	1.30E+00	6.51E+08	1.59E+01
	SD	1.14E+08	1.20E+08	2.22E+07	1.59E-01	1.62E+07	2.40E+00
Film 4	Average	4.33E+09	3.26E+09	4.14E+08	1.28E+00	6.49E+08	1.57E+01
	SD	1.22E+08	1.33E+08	2.08E+07	1.60E-01	1.66E+07	2.31E+00
Film 5	Average	5.25E+09	4.00E+09	4.80E+08	1.19E+00	7.69E+08	1.32E+01
	SD	2.86E+08	1.85E+08	3.20E+07	4.14E-02	6.91E+07	1.01E+00

Where, E_0 is $E_{(t)}$ at t = 0 in **Equation 3.21.** E_0 can also be considered as instantaneous relaxation modulus of the material.

4.2.2.5 Plasticity index analysis

Figure 4.38 shows a representation of nanoindentation *area under curve* analysis with a curve obtained from a pure chitosan film. Here A_1 represents area under the loading curve and A_2 represents the area under the unloading curve. Hold segment (creep effects) is not taken into account while calculating the areas. [84, 89] It is important to note that the area A_1 considered here (**Figure 4.38**) is different than the one shown for the explanation of plasticity index calculations in Chapter 3 in **Figure 3.19c**. In **Figure 4.38**, area A_1 is a whole area occupied under the loading curve regardless of interference of the unloading curve. Because of that, there are slight modifications in the equation

(**Equation 4.2**) for calculating the plasticity indices of the gold-chitosan bionanocomposite films.
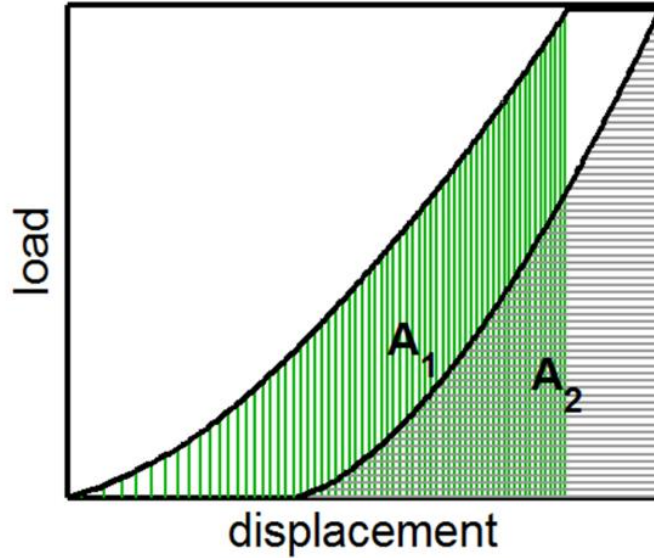
Figure 4.38 Nanoindentation load displacement curve from pure chitosan and representation of area A_1 and A_2 mentioned in Equation 4.2

$$. \; \phi \; = \; \frac{A_1 - A_2}{A_1} \quad \text{……………………...........…………..4.2}$$

As presented in **Figure 4.39**, there is significant increase in plasticity index of chitosan as gold nanoparticle concentration is increased. This could be the reason of losses due to friction between two phases; metallic and polymeric, present in the material. **Table 4.7** summarizes the calculated plasticity indices (mean and standard deviations) of the bionanocomposite films.
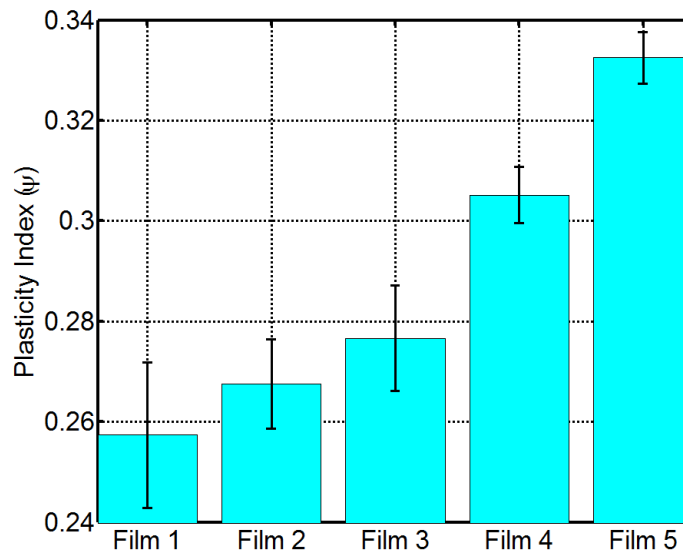
Figure 4.39 Bar plot for plasticity index of the gold-chitosan nanocomposites determined through nanoindentation

Table 4.7 Summary of plasticity index of gold-chitosan nanocomposites

	Film 1	Film 2	Film 3	Film 4	Film 5
Mean	0.257378	0.267555	0.276653	0.305183	0.332508
Std.D	0.014497	0.008846	0.010485	0.0056	0.00509

4.3 Biocompatibility testing

In biomedical applications, chitosan based materials are mainly used as scaffolds in tissue engineering, wound healing and implants. As such, it is important that the scaffold materials are nontoxic, non-reactive and compatible with the living cells. Such properties are important to attach and grow living cells and improve the recovery of damaged tissues.

Figure 4.40 shows optical micrographs of the gold-chitosan nanocomposite films seeded with human epithelial cells and the cell proliferation over a period of time. It is observed that cells adhered well on all the composite films. As we see vertically down, it is also clear that the cells proliferate at day 3 and day 5. It is evident that all the nanocomposite films are nontoxic and biocompatible to the human epithelial cells.
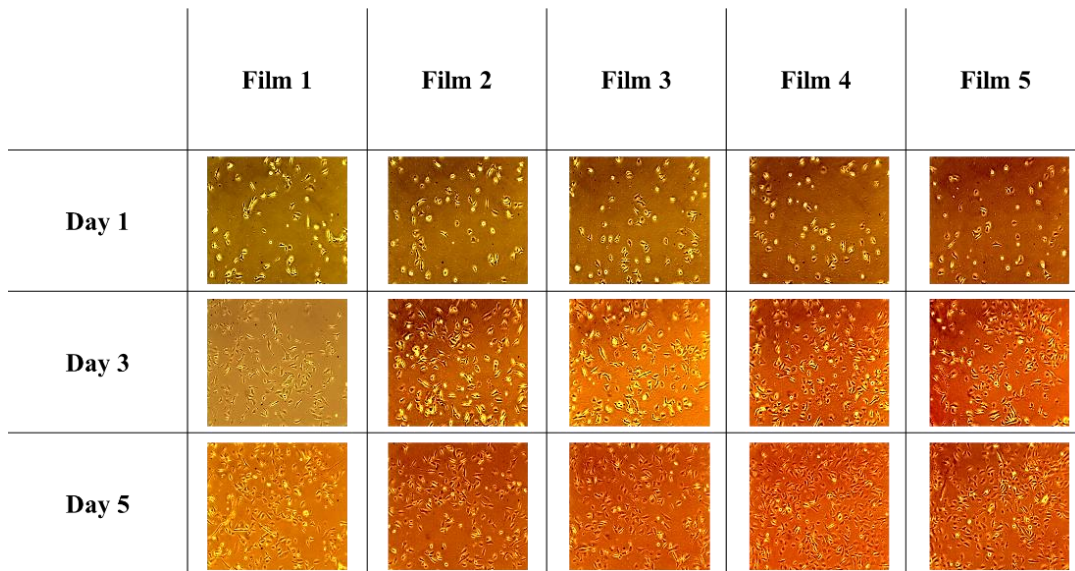
Figure 4.40 Optical micrographs of the cells attached of the gold-chitosan nanocomposites at day 1, day 3 and day 5

Table 4.8 Cell count on day 1, day 3 and day 5 attached on the gold-chitosan nanocomposite films

	Film 1	Film 2	Film 3	Film 4	Film 5
Day 1	58.60	60.60	61.60	65.20	62.60
	± 5.13	± 12.95	± 8.73	± 9.42	± 10.74
Day 3	139.40	136.40	139.60	179.60	149.20
	± 20.35	± 20.53	± 29.76	± 38.28	± 13.33
Day 5	236.60	220.20	263.20	416.00	361.00
	± 20.08	± 9.68	± 61.73	± 24.18	± 26.16
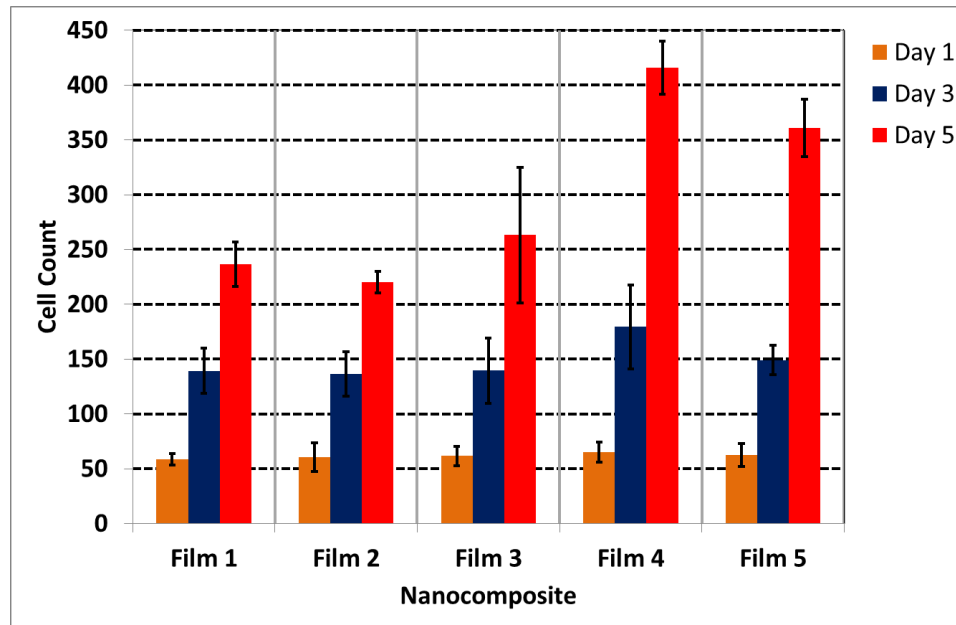
Figure 4.41 Bar plots of the numbers of cells attached on gold-chitosan nanocomposite films (bar height is the average of five readings and error bar is standard deviation)

Also, from the bar plots in **Figure 4.41**, adding certain amount of gold nanoparticles on to chitosan stimulates the cell proliferation. Possible reason for this improvement is an increase in the chitosan film surface area available for cells to adhere and proliferate. However, as the concentration increased above the threshold of 0.20 mg/ml, cell proliferation decreases. These results are consistent with previously published work [19, 90] that have also reported a decreasing proliferation effect with higher amount of gold concentration in a polymer nanocomposites. Cell count numbers for each film and at Day 1, Day 3 and Day 5 are summarized in **Table 4.9**.

4.4 Statistical analysis

When working with mathematical evaluation of the experimental outcomes, it is important to know if any difference in the result is a true response of the factors or it is just by chance that the difference is visible. Careful and systematic analysis of the results for evaluating statistical significance of the factors such as gold reinforcement, temperature, and cell incubation time is necessary. This section shows statistical analysis results (two-way ANOVA) from which sound conclusions can be made for the performance of the gold chitosan bionanocomposites.

The primary assumptions for performing ANOVA are …

1. There are no outliers in any group (or overall).
2. Each group's data (or residuals) is normally distributed.
3. Each group's data (or residuals) has equal variance (also called homogeneity of variances).

Figures 4.42 and **4.43**, shows histograms of residuals of reduced modulus and cell counts, respectively. From the shape of the histogram, it is clear that both the data sets are normally distributed. Also, in the tables next to the plots, the P-values obtained from the Anderson-Darling normality tests are greater than 0.05. That means, it rejects the null hypothesis that the data are from the population that is not normally distributed. Hence it is a quantitative indication that the data are normally distributed.
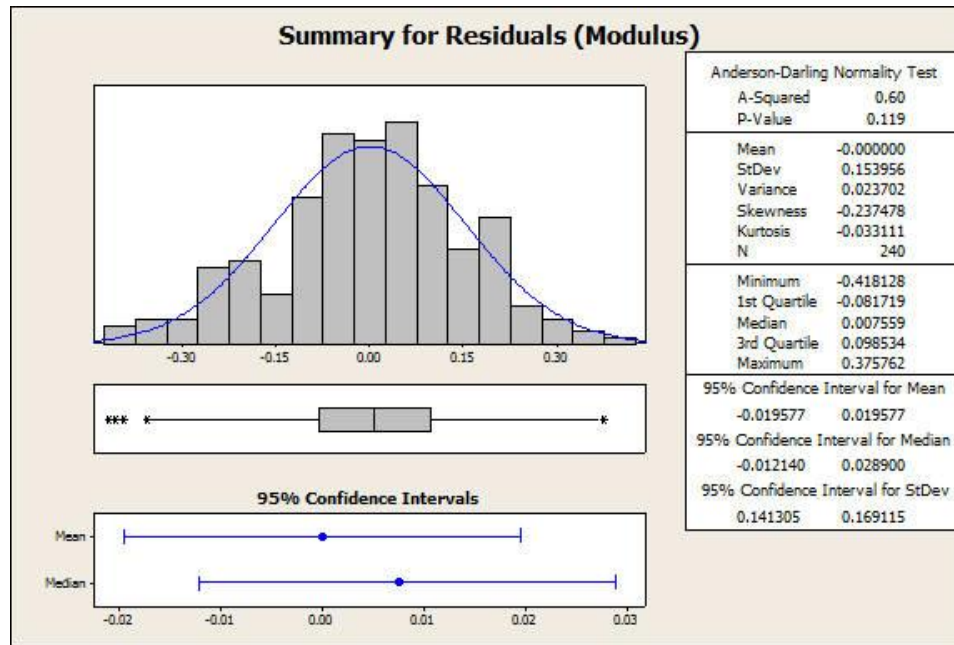
Figure 4.42 Histogram of residuals of reduced modulus
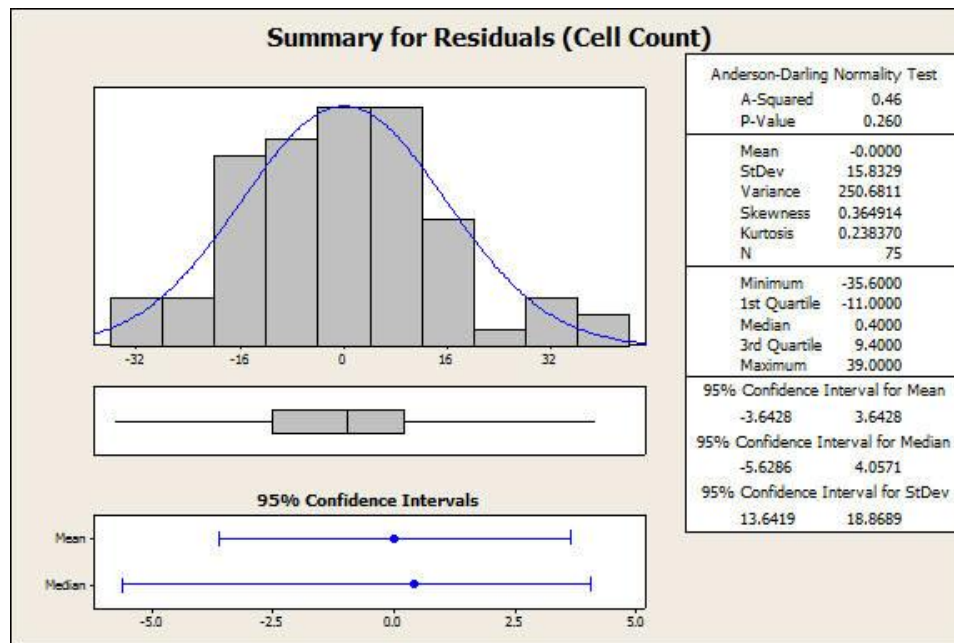
Figure 4.43 Histogram of residuals of cell count

Figures 4.44 and **4.45** show normal probability plots of residuals of reduced modulus and cell count respectively. Since most of the residual points fall on the line, the data is normally distributed. Also, there are no significant outliers observed on the plots.

However, through Levene's homogeneity test for equal variances, it is found that both of the datasets obtained from mechanical characterization and biocompatibility tests fail the assumption of homogeneity of variances ($p < 0.05$ in **Tables 4.10** and **4.11**). However, one could still go with the two-way ANOVA tests by being more conservative with the acceptable alpha level. Instead of the alpha level to be 0.05, in this work it is taken as 0.01 to consider any difference as a significant difference between two effects. This is to avoid type 1 error in the statistical analysis of the two-way ANOVA outcomes while the assumption of "homogeneity of variances" is voided.
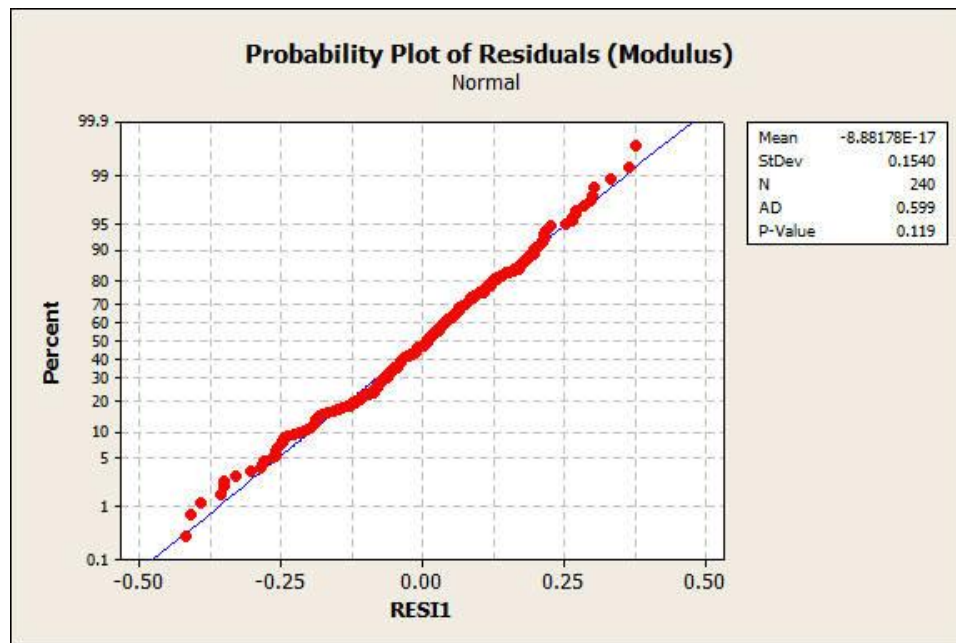
Figure 4.44 Normal probability plots of residuals (reduced modulus)
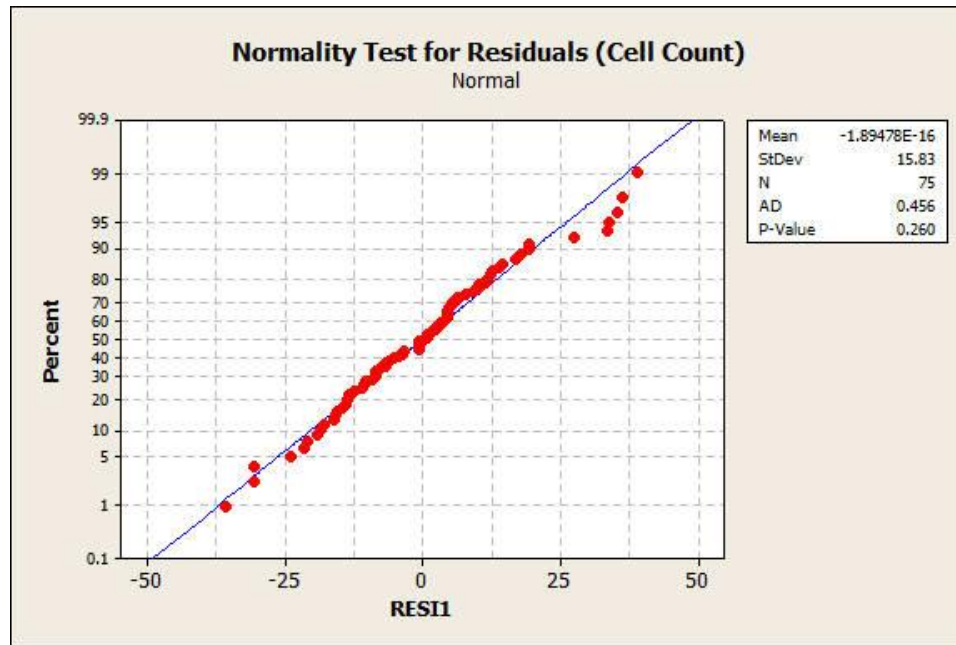
Figure 4.45 Normal probability plots of residuals (cell count)

Table 4.9 Levene's test for homogeneity of variances (reduced modulus)

Dependent Variable: Reduced modulus			
F	df1	df2	Sig. (*p*)
6.661	19	220	.000

Table 4.10 Levene's test for homogeneity of variances (cell count)

Dependent Variable: Cell Count			
F	df1	df2	Sig. (*p*)
2.756	14	60	.003

p values in **Table 4.12** are less than 0.01. It shows that at least one film from the set of five films has significantly different reduced modulus than one from the rest of the films. Similarly, for the effect of temperature, it seems that at least one temperature from

the selected four temperatures has significant impact on the reduced modulus values. In **Table 4.12**, p value for the interaction between the gold concentration and temperature is also less than 0.01. That means, there is an interaction between the two effects namely gold concentration and temperature. In other words, reduce modulus of the film with certain concentration of gold nanoparticles does depend on the test temperature.

Table 4.11 two-way ANOVA table for reduced modulus

Source	df	Sum of Squares	Mean Square	F	p value
Au Concentration	4	52.168	13.042	564.684	.000000000
Temperature	3	59.417	19.806	857.521	.000000000
AuConcentration * Temperature	12	14.577	1.215	52.596	.000000000
Error	220	5.081	.023		
Total	240	2909.929			

To perform more accurate analysis in order to build confidence in the effects of gold concentration and temperature on reduced modulus, a pairwise comparison with post-hoc tests was also performed. **Table A2.1** (see appendix) shows Film-by-Film comparison at each temperature level. Except the cases with their p value boxes highlighted, all films have significantly different reduced modulus than that of the remaining ones in the set.

Table **4.13** is the ANOVA table for the cell count analysis from the biocompatibility studies. p values in **Table 4.13** are less than 0.01. It shows that cell count on at least one film from the set of the film is different than the cell count on remaining films. Similarly, for the time in days, is can be concluded that cell count on at least one day is significantly different than the remaining two days. In **Table 4.13**, the p

value for the interaction between the gold concentration and days is also less than 0.01. Hence, there is an interaction between the two effects such as gold concentration and time in days. In other words, cell count on the film with certain concentration of gold nanoparticles does depend on the test temperature.

Table 4.12 two-way ANOVA table for cell count

Source	df	Sum of Squares	Mean Square	F	P Value
Au_Concentration	4	71768.053	17942.013	28.584	.0000000
Days	2	722916.587	361458.293	575.846	.0000000
Au_Concentration * Days	8	79314.347	9914.293	15.795	.0000000
Error	60	37662.000	627.700		
Total	75	3078821.000			

To perform more accurate analysis of the gold concentration and time in days on the cell count, a pairwise comparison with post-hoc tests was also performed. **Table A2.2** (see appendix) shows Day-by-Day comparison for each gold concentration level. By checking *p* values, it is obvious that there is a considerable difference between the numbers of cells on each day with the remaining days for each case of the films.

Chapter 5 Summary and Conclusions

Considering increasing need of advancement in the field of biomedical engineering, this work was focused on development of advanced materials for their potential use in biomedical applications.

In this work, thin solid films of bio-nanocomposite were prepared with the use of gold nanoparticles as reinforcement and chitosan (a biopolymer; polysaccharide) as a polymer matrix considering their excellent biological properties and film-forming capabilities. First, mono-dispersed gold nanoparticles (~ 32 nm diameter) were synthesized with slight modifications in the classical Turkevich method while chitosan solution was processed with a mild acidic solution. Gold nanoparticles were successfully entrapped into the polymer matrix via a straightforward separate synthesis of the nanoparticles and the polymer, then mixing them to form a homogeneous mixture through mechanical agitations.

TEM, SEM and particle size analysis studies confirmed size and mono-dispersity of the nanoparticles. For purity and crystallinity of the gold nanoparticles; EDX and SAED showed positive results and confirmed that there were no inclusions of other elements and that gold was in its purest form. Being very important factor to be considered in polymer nanocomposites, interfacial wetting and adhesion between the gold nanoparticles and the chitosan matrix was found to be efficient through the zeta potential measurements, TEM and UV-Vis spectroscopy. UV-Vis spectroscopy also confirmed size and dispersion stability of gold nanoparticles in the chitosan matrix for all concentrations. SEM observations showed no significant agglomerations of the gold

nanoparticles throughout the thin films cross-sections. FT-IR spectroscopy showed influence of gold nanoparticles on the molecular structure of the chitosan matrix qualitatively. Through XRD analysis, crystallinity of the bionanocomposite films was found to be increasing proportionally with addition of gold nanoparticles in the chitosan matrix.

Quasi-static and dynamic nanomechanical characterizations were performed *via* instrumented indentation (nanoindentation). Reinforcing amorphous chitosan polymer matrix with crystalline gold nanoparticles was found to be greatly rewarding in improving nanomechanical properties of the resulting nanocomposites. Reduced moduli of the nanocomposites films are significantly ($p < 0.01$) increased with addition of gold nanoparticles. Improvement in dynamic nanomechanical properties such as indentation storage and loss moduli was also confirmed by using gold nanoparticles as a filler material in the chitosan matrix. Time dependent nanomechanical properties such as creep compliance and relaxation moduli were also improved with reinforcing chitosan matrix with the metal nanoparticles. Plasticity index (Ψ) of the gold-chitosan nanocomposite films was increased with increase in gold nanoparticle concentration.

The synthesized bionanocomposite films were found to be non-toxic and biocompatible with human cervix tissue cells. The living cells were found to be adhere and proliferate on the surfaces of the bionanocomposite films. Significant improvement ($p < 0.01$) in number of cells attached with increase in the amount of gold nanoparticles were observed.

Chapter 6 Future Opportunities and Challenges

In this work, gold nanoparticle reinforced chitosan thin films were fabricated and characterized to evaluate their performance attributes for biomedical applications. Important characteristics such as toxicity, biocompatibility and mechanical properties at room temperature, human body temperature and higher temperatures are characterized.

This work focuses on characterizing chitosan based materials considering their potential applications in biomedical fields such as tissue regeneration and wound healing. Such applications widely comprise external medical treatments and curing. However, chitosan based materials have high potential for their use in in-body applications such as coating and scaffold materials for bone tissue regeneration, heart valve materials, blood vessels repairs and more. For such applications, while designing the appropriate materials and devices, it is of utmost importance that their mechanical properties are similar to that of surrounding and target tissues inside the body. In other words, when the materials are subjected to the within-body environments with potential fluidic and temperature effects, it is desired to design and fabricate the materials to avoid any circumstances of failure in the system. When chitosan film is used as a coating material to prevent excessive wear of the surfaces, it is important to monitor the onsets of failures. This can be achieved by monitoring electrical signals transmitting arrangements in the materials.

To perform nanomechanical testing in the environment similar to that present in the human body, body mimicking fluids (BMF) such as carefully prepared saline buffer solution, Hank's balanced salt solution, Earle's balanced salt solution and other commercially available fluids mixed with amino acids, vitamins and glucose can be used

to submerge the chitosan thin films and perform indentations on high temperature stage maintained at 37 °C. The major challenge with such testing is to take buoyancy forces exerted by the fluid on the tip in to account for calibrations as well as for testing and analysis.

For the material to be capable of transmitting and/or transferring electrical signals, it has to be electrically conductive. Gold nanoparticle reinforcement in the polymer matrix is quasi-discontinuous and hence, it is difficult to take advantage of high conductivity of the crystalline gold. This challenge can be addressed by incorporating more continuous type of reinforcement along-with or without gold nanoparticles such as graphene sheets and carbon nanotubes. Electrical conductivity of the gold, graphene and/or carbon nanotube reinforced chitosan can then be characterized with the use of nanomechanical test instruments with Electric Contact Resistance (ECR) tests capabilities. Electrical properties could be characterized as a function of reinforcement content and as a function of depth into the material. With the use of nanoindenter, nano-scale abrasion resistance studies such as nano-wear and scratch tests can also be performed to yield useful information about material properties required for applications with friction and wear.

References

[1]   Khor, E., *Chitin : fulfilling a biomaterials promise*. 2001, Amsterdam; New York: Elsevier Science Ltd.

[2]   Feofilova, E., D. Nemtsev, V. Tereshina, and V. Kozlov, *Polyaminosaccharides of mycelial fungi: new biotechnological use and practical implications*. APPLIED BIOCHEMISTRY AND MICROBIOLOGY C/C OF PRIKLADNAIA BIOKHIMIIA I MIKROBIOLOGIIA, 1996. **32**: p. 437-445.

[3]   Khor, E. and L.Y. Lim, *Implantable applications of chitin and chitosan*. Biomaterials, 2003. **24**(13): p. 2339-2349.

[4]   Riva, R., H. Ragelle, A. des Rieux, N. Duhem, C. Jérôme, and V. Préat, *Chitosan and chitosan derivatives in drug delivery and tissue engineering*, in *Chitosan for Biomaterials II*. 2011, Springer. p. 19-44.

[5]   Wang, X., Y. Du, J. Luo, B. Lin, and J.F. Kennedy, *Chitosan/organic rectorite nanocomposite films: Structure, characteristic and drug delivery behaviour*. Carbohydrate Polymers, 2007. **69**(1): p. 41-49.

[6]   Díaz-Visurraga, J., M.F. Meléndrez, A. García, M. Paulraj, and G. Cárdenas, *Semitransparent chitosan-TiO2 nanotubes composite film for food package applications*. Journal of Applied Polymer Science, 2010. **116**(6): p. 3503-3515.

[7]   Yang, T. and R.R. Zall, *Chitosan Membranes for Reverse Osmosis Application*. Journal of Food Science, 1984. **49**(1): p. 91-93.

[8]   Ravi Kumar, M.N.V., *A review of chitin and chitosan applications*. Reactive and Functional Polymers, 2000. **46**(1): p. 1-27.

[9]   Kim, I.-Y., S.-J. Seo, H.-S. Moon, M.-K. Yoo, I.-Y. Park, B.-C. Kim, and C.-S. Cho, *Chitosan and its derivatives for tissue engineering applications*. Biotechnology Advances, 2008. **26**(1): p. 1-21.

[10]   Cárdenas, G., P. Anaya, C. von Plessing, C. Rojas, and J. Sepúlveda, *Chitosan composite films. Biomedical applications*. Journal of Materials Science: Materials in Medicine, 2008. **19**(6): p. 2397-2405.

[11]   Glos, D.L., F.E. Sauser, I. Papautsky, and D.I. Bylski-Austrow, *Implantable MEMS compressive stress sensors: Design, fabrication and calibration with application to the disc annulus*. Journal of Biomechanics, 2010. **43**(11): p. 2244-2248.

[12]   Bumgardner, J.D., R. Wiser, P.D. Gerard, P. Bergin, B. Chestnutt, M. Marini, V. Ramsey, S.H. Elder, and J.A. Gilbert, *Chitosan: potential use as a bioactive coating for orthopaedic and craniofacial/dental implants*. Journal of Biomaterials Science, Polymer Edition, 2003. **14**(5): p. 423-438.

[13]   Yang, X., Y. Tu, L. Li, S. Shang, and X.-m. Tao, *Well-Dispersed Chitosan/Graphene Oxide Nanocomposites*. ACS Applied Materials & Interfaces, 2010. **2**(6): p. 1707-1713.

[14]   Lavorgna, M., F. Piscitelli, P. Mangiacapra, and G.G. Buonocore, *Study of the combined effect of both clay and glycerol plasticizer on the properties of chitosan films*. Carbohydrate Polymers, 2010. **82**(2): p. 291-298.

[15]   Kithva, P., L. Grøndahl, D. Martin, and M. Trau, *Biomimetic synthesis and tensile properties of nanostructured high volume fraction hydroxyapatite and*

chitosan biocomposite films. Journal of Materials Chemistry, 2010. **20**(2): p. 381-389.

[16]   Tang, C., L. Xiang, J. Su, K. Wang, C. Yang, Q. Zhang, and Q. Fu, *Largely Improved Tensile Properties of Chitosan Film via Unique Synergistic Reinforcing Effect of Carbon Nanotube and Clay.* The Journal of Physical Chemistry B, 2008. **112**(13): p. 3876-3881.

[17]   Wang, S.-F., L. Shen, W.-D. Zhang, and Y.-J. Tong, *Preparation and Mechanical Properties of Chitosan/Carbon Nanotubes Composites.* Biomacromolecules, 2005. **6**(6): p. 3067-3072.

[18]   Fan, H., L. Wang, K. Zhao, N. Li, Z. Shi, Z. Ge, and Z. Jin, *Fabrication, mechanical properties, and biocompatibility of graphene-reinforced chitosan composites.* Biomacromolecules, 2010. **11**(9): p. 2345-2351.

[19]   Lin, Y.-L., J.-C. Jen, S.-h. Hsu, and I.-M. Chiu, *Sciatic nerve repair by microgrooved nerve conduits made of chitosan-gold nanocomposites.* Surgical Neurology, 2008. **70, Supplement 1**(0): p. S9-S18.

[20]   Pingarrón, J.M., P. Yáñez-Sedeño, and A. González-Cortés, *Gold nanoparticle-based electrochemical biosensors.* Electrochimica Acta, 2008. **53**(19): p. 5848-5866.

[21]   Curulli, A., G. Di Carlo, G.M. Ingo, C. Riccucci, D. Zane, and C. Bianchini, *Chitosan Stabilized Gold Nanoparticle-Modified Au Electrodes for the Determination of Polyphenol Index in Wines: a Preliminary Study.* Electroanalysis, 2012. **24**(4): p. 897-904.

[22]   Du, Y., X.-L. Luo, J.-J. Xu, and H.-Y. Chen, *A simple method to fabricate a chitosan-gold nanoparticles film and its application in glucose biosensor.* Bioelectrochemistry, 2007. **70**(2): p. 342-347.

[23]   Luo, X.-L., J.-J. Xu, Y. Du, and H.-Y. Chen, *A glucose biosensor based on chitosan–glucose oxidase–gold nanoparticles biocomposite formed by one-step electrodeposition.* Analytical Biochemistry, 2004. **334**(2): p. 284-289.

[24]   Matteini, P., F. Ratto, F. Rossi, S. Centi, L. Dei, and R. Pini, *Chitosan Films Doped with Gold Nanorods as Laser-Activatable Hybrid Bioadhesives.* Advanced Materials, 2010. **22**(38): p. 4313-4316.

[25]   Kofidis, T., P. Akhyari, J. Boublik, P. Theodorou, U. Martin, A. Ruhparwar, S. Fischer, T. Eschenhagen, H. Kubis, and T. Kraft, *In vitro engineering of heart muscle: artificial myocardial tissue.* The Journal of thoracic and cardiovascular surgery, 2002. **124**(1): p. 63-69.

[26]   ATALA, A., *Tissue engineering of artificial organs.* Journal of Endourology, 2000. **14**(1): p. 49-57.

[27]   Mertsching, H., T. Walles, M. Hofmann, J. Schanz, and W.H. Knapp, *Engineering of a vascularized scaffold for artificial tissue and organ generation.* Biomaterials, 2005. **26**(33): p. 6610-6617.

[28]   Langer R, V.J.P., *Tissue Engineering.* Science, 1993. **260**(5110): p. 920-926.

[29]   Kumbar, S., C. Laurencin, and M. Deng, *Natural and Synthetic Biomedical Polymers.* 2014: Elsevier Science.

[30]   Aslam, M., L. Fu, M. Su, K. Vijayamohanan, and V.P. Dravid, *Novel one-step synthesis of amine-stabilized aqueous colloidal gold nanoparticles.* Journal of Materials Chemistry, 2004. **14**(12): p. 1795-1797.

[31]   Bain, C.D., E.B. Troughton, Y.T. Tao, J. Evall, G.M. Whitesides, and R.G. Nuzzo, *Formation of monolayer films by the spontaneous assembly of organic thiols from solution onto gold.* Journal of the American Chemical Society, 1989. **111**(1): p. 321-335.

[32]   Kumar, S. and R. Jin, *Water-soluble Au 25 (Capt) 18 nanoclusters: synthesis, thermal stability, and optical properties.* Nanoscale, 2012. **4**(14): p. 4222-4227.

[33]   Peniche, C., W. Argüelles-Monal, and F. Goycoolea, *Chitin and chitosan: major sources, properties and applications.* Monomers, Polymers and Composites from Renewable Resources, 2008: p. 517.

[34]   Hanshou, Y., W. Hanzhang, and Y. Bing, *RECENT ADVANCES OF CHITOSAN IN SUPPRESSION OF PLANT DISEASES [J].* Natural Product Research and Development, 2000. **3**: p. 018.

[35]   Vanlerberghe, G. and H. Sebag, *Chitosan derivative, method of making the same and cosmetic composition containing the same.* 1975, US Patent 3,879,376.

[36]   Hirano, S., *Chitin biotechnology applications.* Biotechnology annual review, 1996. **2**: p. 237-258.

[37]   Aider, M., *Chitosan application for active bio-based films production and potential in the food industry: Review.* LWT-Food Science and Technology, 2010. **43**(6): p. 837-842.

[38]   Zeng, D., J. Wu, and J.F. Kennedy, *Application of a chitosan flocculant to water treatment.* Carbohydrate polymers, 2008. **71**(1): p. 135-139.

[39]   Ramachandran, S., *Chitosan-coated pulp, a paper using the pulp, and a process for making them.* 1998, Google Patents.

[40]   Cheng, Q. and D. Shuqin, *Chitosan Fiber Nonwovens and the Prospects for Medical Dressings [J].* Technical Textiles, 2004. **1**: p. 004.

[41]   Wang, N., X. Wang, Y. Jia, X. Li, J. Yu, and B. Ding, *Electrospun nanofibrous chitosan membranes modified with polyethyleneimine for formaldehyde detection.* Carbohydrate polymers, 2014. **108**: p. 192-199.

[42]   Elbarbary, A.M. and T.B. Mostafa, *Effect of γ-rays on carboxymethyl chitosan for use as antioxidant and preservative coating for peach fruit.* Carbohydrate Polymers, 2014.

[43]   Beppu, M., R. Vieira, C. Aimoli, and C. Santana, *Crosslinking of chitosan membranes using glutaraldehyde: Effect on ion permeability and water absorption.* Journal of Membrane Science, 2007. **301**(1): p. 126-130.

[44]   Muzzarelli, R.A. and O. Tubertini, *Chitin and chitosan as chromatographic supports and adsorbents for collection of metal ions from organic and aqueous solutions and sea-water.* Talanta, 1969. **16**(12): p. 1571-1577.

[45]   Zeng, X. and E. Ruckenstein, *Cross-linked macroporous chitosan anion-exchange membranes for protein separations.* Journal of Membrane Science, 1998. **148**(2): p. 195-205.

[46]   Guo, T.-Y., Y.-Q. Xia, J. Wang, M.-D. Song, and B.-H. Zhang, *Chitosan beads as molecularly imprinted polymer matrix for selective separation of proteins.* Biomaterials, 2005. **26**(28): p. 5737-5745.

[47]   Feng, Z., Z. Shao, J. Yao, Y. Huang, and X. Chen, *Protein adsorption and separation with chitosan-based amphoteric membranes.* Polymer, 2009. **50**(5): p. 1257-1263.

[48]   Krajewska, B., *Application of chitin-and chitosan-based materials for enzyme immobilizations: a review.* Enzyme and microbial technology, 2004. **35**(2): p. 126-139.

[49]   Ding, L., C. Hao, Y. Xue, and H. Ju, *A bio-inspired support of gold nanoparticles-chitosan nanocomposites gel for immobilization and electrochemical study of K562 leukemia cells.* Biomacromolecules, 2007. **8**(4): p. 1341-1346.

[50]   Kang, X., J. Wang, H. Wu, I.A. Aksay, J. Liu, and Y. Lin, *Glucose oxidase–graphene–chitosan modified electrode for direct electrochemistry and glucose sensing.* Biosensors and Bioelectronics, 2009. **25**(4): p. 901-905.

[51]   *Tissue engineering.* Nat Biotech, 2000. **18**.

[52]   Du, J. and Y.-L. Hsieh, *PEGylation of chitosan for improved solubility and fiber formation via electrospinning.* Cellulose, 2007. **14**(6): p. 543-552.

[53]   Mao, S., X. Shuai, F. Unger, M. Simon, D. Bi, and T. Kissel, *The depolymerization of chitosan: effects on physicochemical and biological properties.* International journal of Pharmaceutics, 2004. **281**(1): p. 45-54.

[54]   Yalpani, M. and L.D. Hall, *Some chemical and analytical aspects of polysaccharide modifications. III. Formation of branched-chain, soluble chitosan derivatives.* Macromolecules, 1984. **17**(3): p. 272-281.

[55]   Harish Prashanth, K. and R. Tharanathan, *Chitin/chitosan: modifications and their unlimited application potential—an overview.* Trends in food science & technology, 2007. **18**(3): p. 117-131.

[56]   Sashiwa, H. and S.-i. Aiba, *Chemically modified chitin and chitosan as biomaterials.* Progress in Polymer Science, 2004. **29**(9): p. 887-908.

[57]   Mourya, V. and N.N. Inamdar, *Chitosan-modifications and applications: opportunities galore.* Reactive and Functional polymers, 2008. **68**(6): p. 1013-1051.

[58]   Ding, Z., J. Chen, S. Gao, J. Chang, J. Zhang, and E. Kang, *Immobilization of chitosan onto poly-L-lactic acid film surface by plasma graft polymerization to control the morphology of fibroblast and liver cells.* Biomaterials, 2004. **25**(6): p. 1059-1067.

[59]   Pon-On, W., N. Charoenphandhu, J. Teerapornpuntakit, J. Thongbunchoo, N. Krishnamra, and I.M. Tang, *Mechanical properties, biological activity and protein controlled release by Poly(vinyl alcohol)-Bioglass/Chitosan-Collagen composite scaffolds: A Bone tissue engineering applications.* Materials Science and Engineering: C, 2014(0).

[60]   Maganti, N., V. Surya, K. Pavan, W.W. Thein-Han, T.C. Pesacreta, and R.D.K. Misra, *Structure–Process–Property Relationship of Biomimetic Chitosan-Based Nanocomposite Scaffolds for Tissue Engineering: Biological, Physico-Chemical, and Mechanical Functions.* Advanced Engineering Materials, 2011. **13**(3): p. B108-B122.

[61]   Harkins, A.L., S. Duri, L.C. Kloth, and C.D. Tran, *Chitosan–cellulose composite for wound dressing material. Part 2. Antimicrobial activity, blood absorption ability, and biocompatibility.* Journal of Biomedical Materials Research Part B: Applied Biomaterials, 2014: p. n/a-n/a.

[62]   Khan, T.A., K.K. Peh, and H.S. Ch'ng, *Mechanical, bioadhesive strength and biological evaluations of chitosan films for wound dressing.* J. Pharm. Pharmaceut. Sci, 2000. **3**(3): p. 303.

[63]   Burkatovskaya, M., G.P. Tegos, E. Swietlik, T.N. Demidova, A. P Castano, and M.R. Hamblin, *Use of chitosan bandage to prevent fatal infections developing from highly contaminated wounds in mice.* Biomaterials, 2006. **27**(22): p. 4157-4164.

[64]   Available   from: http://www.hemcon.com/Products/HemConBandageOverview/HemConBandage15x15.aspx.

[65]   Albanna, M.Z., T.H. Bou-Akl, H.L. Walters III, and H.W. Matthew, *Improving the mechanical properties of chitosan-based heart valve scaffolds using chitosan fibers.* Journal of the mechanical behavior of biomedical materials, 2012. **5**(1): p. 171-180.

[66]   Turkevich, J., P.C. Stevenson, and J. Hillier, *A study of the nucleation and growth processes in the synthesis of colloidal gold.* Discussions of the Faraday Society, 1951. **11**(0): p. 55-75.

[67]   Avadhani, G.S. *Techniques for Characterization of Nano Materials*. in *Proc. The Sixth International Conference on Mathematical Modeling and Computer Simulation of Material Technologies,(MMT-2010).* 2010. Ariel, Israel.

[68]   Wissing, S. and R. Müller, *Solid lipid nanoparticles as carrier for sunscreens: in vitro release and in vivo skin penetration.* Journal of Controlled Release, 2002. **81**(3): p. 225-233.

[69]   Değim, Z., N. Çelebi, H. Sayan, A. Babül, D. Erdoğan, and G. Take, *An investigation on skin wound healing in mice with a taurine-chitosan gel formulation.* Amino Acids, 2002. **22**(2): p. 187-198.

[70]   Fischer-Cripps, A.C., *Nanoindentation*. 2011: Springer.

[71]   Oliver, W.C. and G.M. Pharr, *An improved technique for determining hardness and elastic modulus using load and displacement sensing indentation experiments.* Journal of Materials Research, 1992. **7**(06): p. 1564-1583.

[72]   Syed Asif, S.A., K.J. Wahl, R.J. Colton, and O.L. Warren, *Quantitative imaging of nanoscale mechanical properties using hybrid nanoindentation and force modulation.* Journal of Applied Physics, 2001. **90**(3): p. 1192-1200.

[73]   Herbert, E., W. Oliver, and G. Pharr, *Nanoindentation and the dynamic characterization of viscoelastic solids.* Journal of Physics D: Applied Physics, 2008. **41**(7): p. 074021.

[74]   Yuya, P.A. and N.G. Patel, *Analytical model for nanoscale viscoelastic properties characterization using dynamic nanoindentation.* Philosophical Magazine, 2014(ahead-of-print): p. 1-15.

[75]   Johnson, K.L. and K.L. Johnson, *Contact Mechanics*. 1987: Cambridge University Press.

[76]   Yang, S., Y.-W. Zhang, and K. Zeng, *Analysis of nanoindentation creep for polymeric materials.* Journal of applied physics, 2004. **95**(7): p. 3655-3666.

[77]   Oyen, M.L., *Sensitivity of polymer nanoindentation creep measurements to experimental variables.* Acta Materialia, 2007. **55**(11): p. 3633-3639.

[78]   Perez, C., V. Alvarez, and A. Vazquez, *Creep behaviour of layered silicate/starch–polycaprolactone blends nanocomposites.* Materials Science and Engineering: A, 2008. **480**(1): p. 259-265.

[79]   Tweedie, C.A. and K.J. Van Vliet, *Contact creep compliance of viscoelastic materials via nanoindentation.* Journal of materials research, 2006. **21**(06): p. 1576-1589.

[80]   Oyen, M.L., *Spherical indentation creep following ramp loading.* Journal of Materials Research, 2005. **20**(08): p. 2094-2100.

[81]   Maxwell, A.S., M.A. Monclus, N.M. Jennett, and G. Dean, *Accelerated testing of creep in polymeric materials using nanoindentation.* Polymer Testing, 2011. **30**(4): p. 366-371.

[82]   Lu, H., B. Wang, J. Ma, G. Huang, and H. Viswanathan, *Measurement of creep compliance of solid polymers by nanoindentation.* Mechanics of time-dependent materials, 2003. **7**(3-4): p. 189-207.

[83]   Yuya, P., E. Amborn, M. Beatty, and J. Turner, *Evaluating anisotropic properties in the porcine temporomandibular joint disc using nanoindentation.* Annals of biomedical engineering, 2010. **38**(7): p. 2428-2437.

[84]   Briscoe, B., L. Fiori, and E. Pelillo, *Nano-indentation of polymeric surfaces.* Journal of Physics D: Applied Physics, 1998. **31**(19): p. 2395.

[85]   Jayasuriya, A.C., A. Aryaei, and A.H. Jayatissa, *ZnO nanoparticles induced effects on nanomechanical behavior and cell viability of chitosan films.* Materials Science and Engineering: C, 2013. **33**(7): p. 3688-3696.

[86]   Escamilla-García, M., G. Calderón-Domínguez, J.J. Chanona-Pérez, R.R. Farrera-Rebollo, J.A. Andraca-Adame, I. Arzate-Vázquez, J.V. Mendez-Mendez, and L.A. Moreno-Ruiz, *Physical and structural characterisation of zein and chitosan edible films using nanotechnology tools.* International Journal of Biological Macromolecules, 2013. **61**(0): p. 196-203.

[87]   Liu, M., Y. Zhang, C. Wu, S. Xiong, and C. Zhou, *Chitosan/halloysite nanotubes bionanocomposites: Structure, mechanical properties and biocompatibility.* International Journal of Biological Macromolecules, 2012. **51**(4): p. 566-575.

[88]   Li, J. and Q. Huang, *Rheological properties of chitosan–tripolyphosphate complexes: From suspensions to microgels.* Carbohydrate Polymers, 2012. **87**(2): p. 1670-1677.

[89]   Shokrieh, M.M., M.R. Hosseinkhani, M.R. Naimi-Jamal, and H. Tourani, *Nanoindentation and nanoscratch investigations on graphene-based nanocomposites.* Polymer Testing, 2013. **32**(1): p. 45-51.

[90]   Hsu, S.-h., C.-M. Tang, and H.-J. Tseng, *Biocompatibility of poly(ether)urethane-gold nanocomposites.* Journal of Biomedical Materials Research Part A, 2006. **79A**(4): p. 759-770.

APPENDICES

A1. Statistical methods

To check the significance of the effects of the factors such as gold concentration and temperature on mechanical propertis and gold concentration and incubation time period on cell grouth, two way analysis of variance (two-way ANOVA or factorial ANOVA) was performed using SPSS Statistic v22. With two-way ANOVA, the mean difference between the groups that are split based on two independent variables (e.g. gold concentration and temperature or gold concentration and incubation time) was evaluated. The main reason behind using two-way ANOVA to see if there is an interaction between two independent variables (factors) on the dependent variable (response). In other words, it is useful in understanding the dependency of one independent variable on the level of the other independent variable to make significant difference in the dependent variable of the response.

A1.1 Two-way ANOVA methods

First, the assumptions that need to be confirmed before performing two-way ANOVA are…

1. There are no outliars in any group or in the whole set of data

2. Each group's data (or residuals) are normally distributed.

3. Each group's data (or residuals) has equal variance (also known as homogeneity of variances).

A1.1.1 Hypothesis tests

Three main hypothesis tests are performed while conducting two-way ANOVA; hypotheses for (1) the main effect for the first factor, (2) the main effect for the second factor, and (3) the interaction effects between the factors.

For factor 'A':

The null hypothesis states

H_{0A}: all group means are equal (i.e. $\mu_{A1} = \mu_{A2} = \mu_{A3} = ... = \mu_{Am}$)

Where m=number of groups or levels of the factor

and the alternative hypothesis is…

H_{1A}: at least one group mean is different i.e. H_{0A} proves wrong

Similarly,

For factor 'B':

H_{0B}: all group means are equal (i.e. $\mu_{B1} = \mu_{B2} = \mu_{B3} = ... = \mu_{Bm}$)

and the alternative hypothesis is…

H_{1B}: at least one group mean is different i.e. H_{0B} proves wrong

And, for interection between 'A' and 'B'

H_{0AB}: there is no interection between two factors

and the alternative hypothesis is…

H_{1AB}: there is an interaction between the two factors

A1.1.1.1 two-way ANOVA

Below is the standard two way ANOVA table

Table A1 a standard two-way ANOVA table

Source	Degrees of Freedom dF	Sum of Squares SS	Mean Square MS = (SS/dF)	F-value F = (MS/MSE)	Probability P
Factor A	a-1	SS_A	$SS_A/(a-1)$	MS_A/MS_E	
Factor B	b-1	SS_B	$SS_A/(a-1)$	MS_B/MS_E	
Interaction A*B	(a-1)(b-1)	SS_{AB}	$SS_{AB}/(a-1)(b-1)$	MS_{AB}/MS_E	
error	ab(n-1)	SS_E	$SS_E/ab(n-1)$		
Total	nab-1	SS_T			

Tabel shows standard way of presenting different elements of two-way ANOVA parameters. 'a' represnets number of levels of factor A. Similarly, 'b' represents number of level of factor 'b'. 'n' represents replicates or repetaions of the tests.

Now, first the grand total which is a sum of all the observations in study is calculated as…

$$Y... = \sum_{i}^{a} \sum_{j}^{b} \sum_{k}^{n} Y_{ijk}$$

where, 'i' and 'j' represent the level of factors A and B, respectively. 'k' represents given case or trial for a particular treatment.

and, the overall mean is…

$$\bar{\bar{Y}} = \bar{Y}... = \frac{\sum_i^a \sum_j^b \sum_k^n Y_{ijk}}{nab}$$

Once the grand total and overall mean are calculated, sum of squares for the ANOVA table can be calculated as follows.

$$SS_A = nb \sum_{i=1}^{a} (\bar{Y}_{i..} - \bar{Y}_{...})^2$$

$$SS_B = na \sum_{j=1}^{b} (\bar{Y}_{.j.} - \bar{Y}_{...})^2$$

Where, $Y_{i..}$ and $Y_{.j.}$ are the total of all observations for the ith factor level of A, and j^{th} factor level of B, respectively.

$$SS_{AB} = n \sum_{j=1}^{b} \sum_{i=1}^{a} (\bar{Y}_{ij.} - \bar{Y}_{i..} - \bar{Y}_{.j.} + \bar{Y}_{...})^2$$

Where, $Y_{ij.}$ is the sum of observations of the treatment corresponding to the ith level of factor A and the jth level of factor B.

$$SS_E = \sum_{i=1}^{a} \sum_{j=1}^{b} \sum_{k=1}^{n} (Y_{ijk} - \bar{Y}_{ij.})^2$$

and,

$$SS_T = \sum_{i=1}^{a} \sum_{j=1}^{b} \sum_{k=1}^{n} (Y_{ijk} - \bar{Y}_{...})^2$$

Once sum of square values are calculated, mean squares (MS) and calculated F-values can be deteremined in the ANOVA table.

Now depending on the alpha level selected, F-critical values are taken from the F-table. If F-critical value is lower than F values calculated in the ANOVA table for the set alpha level, the null hypothesis was rejected and the factor was considered to have significant effect on the response. A typical F-distribution curve is shown in **Figure A1**.
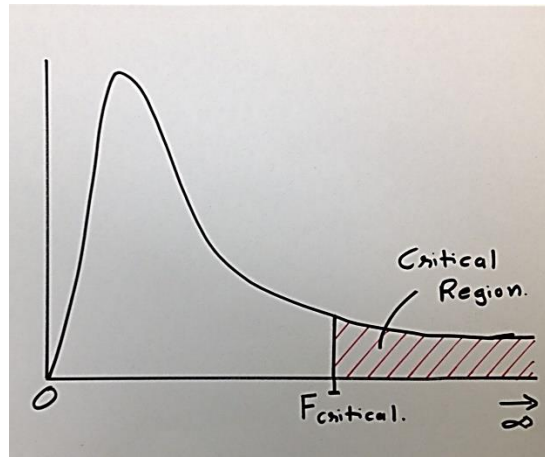
Figure A1 a representation of a typical F curve

A2. Pairwise comparison tables

Table A2.1 Pairwise comparison of reduced modulus

Temperature			Mean Difference (I-J)	Std. Error	P values	95% Confidence Interval for Difference	
						Lower Bound	Upper Bound
25	Film 1	Film 2	-.360*	0.06	.000000	-.482	-.238
		Film 3	-.955*	0.06	.000000	-1.077	-.833
		Film 4	-1.604*	0.06	.000000	-1.726	-1.482
		Film 5	-2.372*	0.06	.000000	-2.494	-2.249
	Film 2	Film 1	.360*	0.06	.000000	.238	.482
		Film 3	-.595*	0.06	.000000	-.717	-.473
		Film 4	-1.244*	0.06	.000000	-1.366	-1.122
		Film 5	-2.012*	0.06	.000000	-2.134	-1.889
	Film 3	Film 1	.955*	0.06	.000000	.833	1.077
		Film 2	.595*	0.06	.000000	.473	.717

		Film 4	-.649*	0.06	.000000	-.771	-.527
		Film 5	-1.417*	0.06	.000000	-1.539	-1.294
	Film 4	Film 1	1.604*	0.06	.000000	1.482	1.726
		Film 2	1.244*	0.06	.000000	1.122	1.366
		Film 3	.649*	0.06	.000000	.527	.771
		Film 5	-.767*	0.06	.000000	-.890	-.645
	Film 5	Film 1	2.372*	0.06	.000000	2.249	2.494
		Film 2	2.012*	0.06	.000000	1.889	2.134
		Film 3	1.417*	0.06	.000000	1.294	1.539
		Film 4	.767*	0.06	.000000	.645	.890
37	Film 1	Film 2	-.341*	0.06	.000000	-.463	-.219
		Film 3	-.621*	0.06	.000000	-.743	-.499
		Film 4	-1.232*	0.06	.000000	-1.354	-1.109
		Film 5	-1.037*	0.06	.000000	-1.159	-.914
	Film 2	Film 1	.341*	0.06	.000000	.219	.463
		Film 3	-.280*	0.06	.000010	-.402	-.158
		Film 4	-.891*	0.06	.000000	-1.013	-.769
		Film 5	-.696*	0.06	.000000	-.818	-.574
	Film 3	Film 1	.621*	0.06	.000000	.499	.743
		Film 2	.280*	0.06	.000010	.158	.402
		Film 4	-.611*	0.06	.000000	-.733	-.489
		Film 5	-.416*	0.06	.000000	-.538	-.294
	Film 4	Film 1	1.232*	0.06	.000000	1.109	1.354
		Film 2	.891*	0.06	.000000	.769	1.013
		Film 3	.611*	0.06	.000000	.489	.733
		Film 5	.195*	0.06	.001903	.073	.317
	Film 5	Film 1	1.037*	0.06	.000000	.914	1.159
		Film 2	.696*	0.06	.000000	.574	.818
		Film 3	.416*	0.06	.000000	.294	.538
		Film 4	-.195*	0.06	.001903	-.317	-.073
60	Film 1	Film 2	-.321*	0.06	.000001	-.443	-.199
		Film 3	-.466*	0.06	.000000	-.588	-.344
		Film 4	-.772*	0.06	.000000	-.894	-.649
		Film 5	-.984*	0.06	.000000	-1.106	-.862
	Film 2	Film 1	.321*	0.06	.000001	.199	.443
		Film 3	-.145*	0.06	.020334	-.267	-.023
		Film 4	-.451*	0.06	.000000	-.573	-.329
		Film 5	-.663*	0.06	.000000	-.786	-.541
	Film 3	Film 1	.466*	0.06	.000000	.344	.588
		Film 2	.145*	0.06	.020334	.023	.267
		Film 4	-.306*	0.06	.000002	-.428	-.184

		Film 5	-.518[*]	0.06	.000000	-.641	-.396
	Film 4	Film 1	.772[*]	0.06	.000000	.649	.894
		Film 2	.451[*]	0.06	.000000	.329	.573
		Film 3	.306[*]	0.06	.000002	.184	.428
		Film 5	-.212[*]	0.06	.000733	-.335	-.090
	Film 5	Film 1	.984[*]	0.06	.000000	.862	1.106
		Film 2	.663[*]	0.06	.000000	.541	.786
		Film 3	.518[*]	0.06	.000000	.396	.641
		Film 4	.212[*]	0.06	.000733	.090	.335
80	Film 1	Film 2	-.031	0.06	.619710	-.153	.091
		Film 3	-.270[*]	0.06	.000021	-.392	-.148
		Film 4	-.457[*]	0.06	.000000	-.579	-.334
		Film 5	-.669[*]	0.06	.000000	-.791	-.547
	Film 2	Film 1	.031	0.06	.619710	-.091	.153
		Film 3	-.239[*]	0.06	.000152	-.361	-.117
		Film 4	-.426[*]	0.06	.000000	-.548	-.304
		Film 5	-.638[*]	0.06	.000000	-.761	-.516
	Film 3	Film 1	.270[*]	0.06	.000021	.148	.392
		Film 2	.239[*]	0.06	.000152	.117	.361
		Film 4	-.187[*]	0.06	.002930	-.309	-.064
		Film 5	-.399[*]	0.06	.000000	-.521	-.277
	Film 4	Film 1	.457[*]	0.06	.000000	.334	.579
		Film 2	.426[*]	0.06	.000000	.304	.548
		Film 3	.187[*]	0.06	.002930	.064	.309
		Film 5	-.212[*]	0.06	.000733	-.335	-.090
	Film 5	Film 1	.669[*]	0.06	.000000	.547	.791
		Film 2	.638[*]	0.06	.000000	.516	.761
		Film 3	.399[*]	0.06	.000000	.277	.521
		Film 4	.212[*]	0.06	.000733	.090	.335

Table A2.2 Pairwise comparison for cell count

Au_Concentration			Mean Difference (I-J)	Std. Error	P Value	95% Confidence Interval for Difference[b]	
						Lower Bound	Upper Bound
Film 1	Day 1	Day 3	-80.800*	15.846	.0000037	-112.496	-49.104
		Day 5	-178.000*	15.846	.0000000	-209.696	-146.304
	Day 3	Day 1	80.800*	15.846	.0000037	49.104	112.496
		Day 5	-97.200*	15.846	.0000001	-128.896	-65.504
	Day 5	Day 1	178.000*	15.846	.0000000	146.304	209.696
		Day 3	97.200*	15.846	.0000001	65.504	128.896
Film 2	Day 1	Day 3	-75.800*	15.846	.0000116	-107.496	-44.104
		Day 5	-159.600*	15.846	.0000000	-191.296	-127.904
	Day 3	Day 1	75.800*	15.846	.0000116	44.104	107.496
		Day 5	-83.800*	15.846	.0000018	-115.496	-52.104
	Day 5	Day 1	159.600*	15.846	.0000000	127.904	191.296
		Day 3	83.800*	15.846	.0000018	52.104	115.496
Film 3	Day 1	Day 3	-78.000*	15.846	.0000070	-109.696	-46.304
		Day 5	-201.600*	15.846	.0000000	-233.296	-169.904
	Day 3	Day 1	78.000*	15.846	.0000070	46.304	109.696
		Day 5	-123.600*	15.846	.0000000	-155.296	-91.904
	Day 5	Day 1	201.600*	15.846	.0000000	169.904	233.296
		Day 3	123.600*	15.846	.0000000	91.904	155.296
Film 4	Day 1	Day 3	-114.400*	15.846	.0000000	-146.096	-82.704
		Day 5	-350.800*	15.846	.0000000	-382.496	-319.104
	Day 3	Day 1	114.400*	15.846	.0000000	82.704	146.096
		Day 5	-236.400*	15.846	.0000000	-268.096	-204.704
	Day 5	Day 1	350.800*	15.846	.0000000	319.104	382.496
		Day 3	236.400*	15.846	.0000000	204.704	268.096
Film 5	Day 1	Day 3	-86.600*	15.846	.0000009	-118.296	-54.904
		Day 5	-298.400*	15.846	.0000000	-330.096	-266.704
	Day 3	Day 1	86.600*	15.846	.0000009	54.904	118.296
		Day 5	-211.800*	15.846	.0000000	-243.496	-180.104
	Day 5	Day 1	298.400*	15.846	.0000000	266.704	330.096
		Day 3	211.800*	15.846	.0000000	180.104	243.496